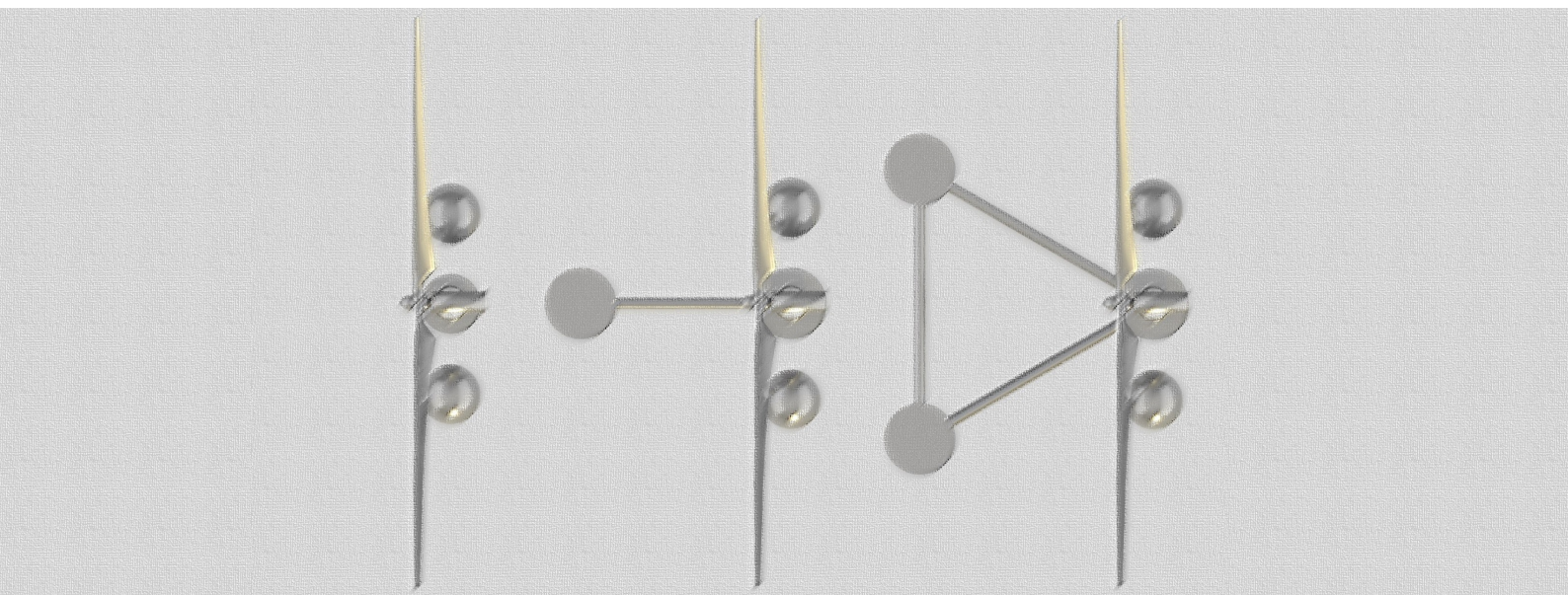


A HYDRODYNAMIC ANALYSIS OF THREE FLOATING OFFSHORE
WIND-WAVE ENERGY CONVERTERS DIFFERING IN THE FLOATING
STABILITY PRINCIPLE

MARTIN A. GONZALEZ JIMENEZ



Master of Science Thesis

March 2020

Martin A. Gonzalez Jimenez: *A hydrodynamic analysis of three floating offshore wind-wave energy converters differing in the floating stability principle*, Master of Science Thesis, © March 2020

“Success is not final, failure is not fatal: it is the courage to continue that counts.” - Sir Winston Churchill.

Dedicated to my family. It is an immense joy to share this sailing through life with you!

A HYDRODYNAMIC ANALYSIS OF THREE FLOATING
OFFSHORE WIND-WAVE ENERGY CONVERTERS
DIFFERING IN THE FLOATING STABILITY PRINCIPLE

by

MARTIN A. GONZALEZ JIMENEZ

in partial fulfilment of the requirements for the degree of

MASTER OF SCIENCE
in Marine Technology

at the Delft University of Technology,

to be defended publicly on Wednesday April 1st, 2020 at 2:00 PM.

CHAIRPERSON:	Dr. Ir. P.R.Wellens	TU Delft
FIRST SUPERVISOR:	Dr. Ir. A. Jarquin Laguna	TU Delft
SECOND SUPERVISOR:	J. Tan MSc	TU Delft

This thesis is confidential and cannot be made public until April 1, 2020.

An electronic version of this thesis is available at <http://repository.tudelft.nl/>.

ABSTRACT

A significant percentage of the offshore wind resource is located in waters deeper than 60m. Therefore, several floating offshore wind turbines (FOWT) have been conceived in recent years. In deep waters, it seems logical to also harvest wave energy. One of the options to harness both resources is to use a floating offshore hybrid wind-wave energy converter (FOHWWEC), which physically combines a FOWT with a wave energy converter (WEC).

Different studies have addressed the functionality, feasibility, optimization, control and survivability of FOHWWEC concepts. The majority considers a proven FOWT substructure to fit a certain type of WEC. Dynamic analyses in both, frequency and time domains, and laboratory experiments with models have been done. Nevertheless, the investigated studies have not considered the FOHWWEC concept as part of an extensive design space. In other words, they have not attempted to explore and compare the myriad design configurations that are possible in that space. Besides this, few studies have been able to deliver a comprehensive understanding on how certain parameters, intrinsic and extrinsic to the FOHWWEC system, influence its performance.

The present study is the start of that space exploration and understanding. Three FOHWWEC design configurations (DC), based on the substructure stability principle, are proposed. Vertical cylinders are used as substructure and two spherical point absorbers are connected through a PTO without mechanical spring to the cylinder supporting the WT. The objective is to compare their performances, based on two variables: the annual average absorption width and the maximum standard deviation of the horizontal nacelle acceleration. Besides this, three draft levels are considered and their impact in the performance is also analyzed. The hydrodynamic analysis of the FOHWWEC with parked WT is performed in the frequency domain. Hydrodynamic coefficients and wave-excitation forces are obtained from the BEM solver NEMOH. The software *FOHWWEC Analysis program*, developed by the author, solves the EoMs and calculates the performance variables. The North Sea is the selected region and a JONSWAP spectrum has been applied.

The results indicate that the design configuration 3 (DC₃) FOHWWECs have a wave power absorption mechanism based on the heave resonance of both, substructure and WECs. This mechanism is more efficient than DC₁ and DC₂'s mechanisms. This allows to maximize the absorption width. Besides this, DC₃ FOHWWECs can also minimize the nacelle accelerations (DC₃-D₂ case). The effect of the draft on both performance variables differs depending on the DC.

Wide-ranging deductions from the results can be summarized as follows. It is reasonable to design a FOHWWEC as a whole system, considering both, wind and wave power generation from the beginning. Using an existing substructure means to lose performance improvement opportunities. It is also reasonable to select a buoyancy-stabilized substructure for the design. This allows to reach the most efficient wave power absorption mechanism, while providing the required flexibility to thoroughly explore and find the balance between design parameters such as WPA, displacement, draft, size and position of the WECs, mooring, among others.

CONTENTS

1	INTRODUCTION	1
1.0.1	Background	1
1.0.2	General scope definition	2
1.0.3	Research objectives	4
1.0.4	Method outline	5
1.0.5	Structure of the thesis	8
2	STATE OF THE ART	9
2.1	Research on FOHWWECs	9
2.2	Research on FOWTs	11
3	DYNAMICS OF FLOATING STRUCTURES	15
3.1	Hydrodynamic classification	15
3.2	Floating stability principles	16
3.3	Rigid single body in regular waves	16
3.4	Rigid multi-bodies in regular waves	23
3.5	Two DOFs spring-damper model	24
3.6	Response in irregular waves	25
4	WAVE POWER	27
4.1	Description of waves	27
4.2	Available power in waves	31
4.3	Wave power absorption	33
4.4	Absorption width	38
4.5	Annual Energy Absorption	39
5	METHODOLOGY DESCRIPTION	41
5.1	Definition of the WEC Unit	41
5.1.1	Geometry	41
5.1.2	PTO system	42
5.2	Definition of the design configurations	42
5.2.1	Additional design requirements	42
5.2.2	Geometry	43
5.2.3	Naming conventions	44
5.3	Definition of the simulations	45
5.4	Hydrostatic stability calculation	45
5.5	Mesh modeling and conversion	48
5.6	Hydrodynamic coefficients calculation in NEMOH	49
5.7	Mooring details and loads	50
5.8	Wave data and JONSWAP Spectrum	51
5.9	Available power calculation	53
5.10	Motion and performance calculation	54
5.10.1	PTO damping optimization	55
5.10.2	Performance variables definition	56
6	VERIFICATION OF THE RESULTS	59
6.1	Verification and validation of the NEMOH results	59

6.1.1	Verification of the panel length	59
6.1.2	Validation of the hydrodynamic coefficients	63
6.2	Verification of the motion and performance module	64
6.2.1	Qualitative verification of the FOWT RAO calculation	64
6.2.2	Qualitative verification of the FOHWWECCAO calculation	67
6.2.3	Verification of the power absorption calculation	68
7	SIMULATION RESULTS	71
7.1	Isolated WEC simulation	71
7.1.1	Relevant intermediate results	72
7.1.2	Performance analysis	74
7.2	DC1 simulation	75
7.2.1	Relevant intermediate results	76
7.2.2	Performance analysis	81
7.3	DC2 simulation	85
7.3.1	Relevant intermediate results	85
7.3.2	Performance analysis	90
7.4	DC3 simulation	94
7.4.1	Relevant intermediate results	95
7.4.2	Performance analysis	101
7.5	Combined results	107
7.5.1	Relevant intermediate results	107
7.5.2	Performance analysis	108
8	CONCLUSIONS AND RECOMMENDATIONS	113
8.1	Objective related conclusions	113
8.2	Wide-ranging conclusions	114
8.3	Recommendations	116
A	APPENDIX A	119
A.1	Stability calculation results for DC2 and DC3	119
A.2	Standard deviation of the nacelle acceleration matrices of DC FOWTs	122
A.3	Absorbed energy matrices of DC FOHWWECCs	124
B	APPENDIX B	127
B.1	Wind turbine properties	127
C	APPENDIX C	129
C.1	FOHWWECC Analysis Program - User guide	129
	BIBLIOGRAPHY	145

LIST OF FIGURES

Figure 1	FOWT substructure designs [5]	1
Figure 2	FOHWWEC design space scope	3
Figure 3	Method flowchart	7
Figure 4	Sphere on 'WindFloat' [10]	9
Figure 5	OWCs on 'WindFloat' [11]	9
Figure 6	MARINA FP7 Project's selected hybrid concepts: 1- STC, 2-SFC [13]. 3-W2Power, 4-OWC array [12]	10
Figure 7	'MERMAID' platform [20]	11
Figure 8	'Poseidon 37' platform [21]	11
Figure 9	WaveStar [23]	11
Figure 10	Ballast-stabilized FOWT	12
Figure 11	Buoyancy-stabilized FOWT	12
Figure 12	Hall's basic substructure geometries	13
Figure 13	Relative importance of mass, viscous drag and diffrac- tion forces on marine structures [28]	15
Figure 14	Coordinate systems	17
Figure 15	Mass-spring-damper model	19
Figure 16	2 DOFs spring-damper model	25
Figure 17	Regular wave definitions [27]	27
Figure 18	Irregular wave definitions	27
Figure 19	Power absorption by a planar version of a heaving PA	33
Figure 20	Budal diagram	38
Figure 21	WEC unit: Spherical PA	41
Figure 22	WEC unit and WT cylinder	41
Figure 23	DC1 substructure and WECs	43
Figure 24	DC2 substructure and WECs	43
Figure 25	DC3 substructure and WECs	44
Figure 26	Righting moment curve for DC1-D1	47
Figure 27	Righting moment curve for DC1-D2	47
Figure 28	Righting moment curve for DC1-D3	47
Figure 29	DC1 mesh example	49
Figure 30	Mooring line catenary profile	50
Figure 31	JONSWAP spectra in operational subset for $H_s = 1.5\text{m}$	53
Figure 32	Absorbed power Vs frequency with optimum b_{PTO} for DC1-D1	55
Figure 33	Absorbed power Vs b_{PTO} containing the maximum power for DC1-D1	56
Figure 34	DCt with fine mesh	60
Figure 35	DCt with medium mesh	60
Figure 36	DCt with coarse mesh	60
Figure 37	Mesh influence on heave added mass of cylinder	61

Figure 38	Mesh influence on pitch added mass of cylinder	61
Figure 39	Mesh influence on heave added mass of sphere	61
Figure 40	Mesh influence on heave damping of cylinder	61
Figure 41	Mesh influence on pitch damping of cylinder	61
Figure 42	Mesh influence on heave damping of sphere	62
Figure 43	Mesh influence on heave wave excit. force of cyl.	62
Figure 44	Mesh influence on pitch wave excit. force of cyl.	62
Figure 45	Mesh influence on heave wave excit. force of sphere	62
Figure 46	Hulme and NEMOH results for the normalized coeff. \hat{a}_{33} of a heaving hemisphere	63
Figure 47	Hulme and NEMOH results for the normalized coeff. \hat{b}_{33} of a heaving hemisphere	64
Figure 48	Surge RAO of HyWind FOWT [44]	65
Figure 49	Surge RAO of DC ₁ FOWT	65
Figure 50	Heave RAO of HyWind FOWT [44]	65
Figure 51	Heave RAO of DC ₁ FOWT	65
Figure 52	Pitch RAO of HyWind FOWT [44]	65
Figure 53	Pitch RAO of DC ₁ FOWT	65
Figure 54	Surge RAO of DC ₁ FOHWEC and FOWT	67
Figure 55	Heave RAO of DC ₁ FOHWEC and FOWT	67
Figure 56	Pitch RAO of DC ₁ FOHWEC and FOWT	68
Figure 57	Budal diagram including results from the present study	69
Figure 58	Rel. heave spectrum of isolated WEC	72
Figure 59	Heave RAO of isolated WEC	73
Figure 60	Nacelle acc. spectrum of DC ₁ FOHWECs	76
Figure 61	Rel. heave spectrum of WEC on DC ₁ FOHWECs	76
Figure 62	Surge RAO of DC ₁ FOHWECs	77
Figure 63	Heave RAO of DC ₁ FOHWECs	77
Figure 64	Heave RAO of WEC on DC ₁ FOHWECs	77
Figure 65	Rel. heave RAO of WEC on DC ₁ FOHWECs	77
Figure 66	Pitch RAO of DC ₁ FOHWECs	77
Figure 67	Nacelle acc. RAO of DC ₁ FOHWECs	77
Figure 68	Pitch RAO of DC ₁ FOWTs	78
Figure 69	Nacelle acc. RAO of DC ₁ FOWTs	78
Figure 70	Pitch wave excitation force on DC ₁ subs. and FOWT	78
Figure 71	Pitch wave excitation force on DC ₁ -D ₃ WEC	78
Figure 72	DC ₁ performance plot	81
Figure 73	Nacelle acc. spectrum of DC ₂ FOHWECs	85
Figure 74	Rel. heave spect. of WEC on DC ₂ FOHWECs	85
Figure 75	Surge RAO of DC ₂ FOHWECs	86
Figure 76	Heave RAO of DC ₂ FOHWECs	86
Figure 77	Heave RAO of WEC on DC ₂ FOHWECs	86
Figure 78	Rel. heave RAO of WEC on DC ₂ FOHWECs	86
Figure 79	Pitch RAO of DC ₂ FOHWECs	86
Figure 80	Nacelle acc. RAO of DC ₂ FOHWECs	86
Figure 81	Pitch RAO of DC ₂ FOWTs	87

Figure 82	Nacelle acc. RAO of DC2 FOWTs	87
Figure 83	Pitch wave excitation force on DC2 subs. and FOWT	87
Figure 84	Pitch wave excitation force on DC2-D3 WEC	87
Figure 85	DC2 performance plot	91
Figure 86	Nacelle acc. spectrum of DC3 FOHWWECs. Sea state 1	95
Figure 87	Nacelle acc. spectrum of DC3 FOHWWECs. Sea state 1	95
Figure 88	Rel. heave spect. of WEC on DC3. Sea state 1	95
Figure 89	Rel. heave spect. of WEC on DC3. Sea state 2	95
Figure 90	Surge RAO of DC3 FOHWWECs. Sea state 1	96
Figure 91	Heave RAO of DC3 FOHWWECs. Sea state 1	96
Figure 92	Heave RAO of WEC on DC3 FOHWWECs. Sea state 1	96
Figure 93	Rel. heave RAO of WEC on DC3 FOHWWECs. Sea state 1	96
Figure 94	Pitch RAO of DC3 FOHWWECs. Sea state 1	96
Figure 95	Nacelle acc. RAO of DC3 FOHWWECs. Sea state 1	96
Figure 96	Surge RAO of DC3 FOHWWECs. Sea state 2	97
Figure 97	Heave RAO of DC3 FOHWWECs. Sea state 2	97
Figure 98	Heave RAO of WEC on DC3 FOHWWECs. Sea state 2	97
Figure 99	Rel. heave RAO of WEC on DC3 FOHWWECs. Sea state 2	97
Figure 100	Pitch RAO of DC3 FOHWWECs. Sea state 2	97
Figure 101	Nacelle acc. RAO of DC3 FOHWWECs. Sea state 2	97
Figure 102	Pitch RAO of DC3 FOWTs. Sea state 1	98
Figure 103	Nacelle acc. RAO of DC3 FOWTs. Sea state 1	98
Figure 104	Pitch wave excitation force on DC3 subs. and FOWT	98
Figure 105	Pitch wave excitation force on DC3-D3 WEC	98
Figure 106	DC3 performance plot	102
Figure 107	Heave RAO of DC3-D2 and DC3-D3 FOHWWECs and FOWTs	106
Figure 108	WEC wave-excitation force in heave. All DCs	107
Figure 109	Damping coeff. b_{33}^{CC} . Combined plot	108
Figure 110	Damping coeff. b_{33}^{AA} . Combined plot	108
Figure 111	Heave wave excitation force on WEC. Combined plot	108
Figure 112	Heave wave excit. force on substructure. Combined plot	108
Figure 113	Combined performance plot	109
Figure 114	Righting moment curve for DC2-D1	121
Figure 115	Righting moment curve for DC2-D2	121
Figure 116	Righting moment curve for DC2-D3	121
Figure 117	Righting moment curve for DC3-D1	122
Figure 118	Righting moment curve for DC3-D2	122
Figure 119	Righting moment curve for DC3-D3	122
Figure C.1.1	Group 1 python files	131
Figure C.1.2	Group 2 python files	132
Figure C.1.3	Group 3 python files	132
Figure C.1.4	Group 4 python files	132
Figure C.1.5	Group 5 python files	132

Figure C.1.6	Group 6 python files	132
Figure C.1.7	Group 7 python files	133
Figure C.1.8	Group 8 processing python files	134
Figure C.1.9	Group 8 post-processing python files	134
Figure C.1.10	Group 9 python files	134
Figure C.1.11	Group 10 python files	134
Figure C.1.12	SALOME installation directory	134
Figure C.1.13	SALOME folder for python scripts	135
Figure C.1.14	Shared folder example	135
Figure C.1.15	Main user interface	136
Figure C.1.16	Initial configuration paths	136
Figure C.1.17	Wave scatter diagram *.txt file example	136
Figure C.1.18	SALOME results folder	137
Figure C.1.19	NEMOH data	137
Figure C.1.20	Step-by-step of working with the program	138
Figure C.1.21	SALOME input example for DC1	138
Figure C.1.22	WT input	139
Figure C.1.23	Hydrostatic stability input	139
Figure C.1.24	NEMOH input	139
Figure C.1.25	HS Stability output folders	140
Figure C.1.26	Converted mesh files for DC1	140
Figure C.1.27	Message requesting input from user	140
Figure C.1.28	Example NEMOH initialization folder	141
Figure C.1.29	Example of NEMOH results folder	141
Figure C.1.30	Example of <i>RadiationCoefficients.tec</i> file for DC1-D1	141
Figure C.1.31	Example of <i>ExcitationForce.tec</i> file for DC1-D1	142
Figure C.1.32	Mooring input example	142
Figure C.1.33	Mooring data folder	142
Figure C.1.34	Dynamic model input example	143
Figure C.1.35	Program's result folders	143
Figure C.1.36	Example result plots	144

LIST OF TABLES

Table 1	WEC unit parameters	42
Table 2	DC ₁ FOHWWECs parameters	44
Table 3	DC ₂ FOHWWECs parameters	44
Table 4	DC ₃ FOHWWECs parameters	44
Table 5	FOHWWEC names	44
Table 6	DC ₁ common stability input	46
Table 7	FOWT DC ₁ -D ₁ stability I/O	46
Table 8	FOWT DC ₁ -D ₂ stability I/O	46
Table 9	FOWT DC ₁ -D ₃ stability I/O	46
Table 10	NEMOH input parameters	49
Table 11	Mooring system properties	50
Table 12	Scatter diagram of the North Sea region [42]	52
Table 13	Scatter diagram operational subset of the North Sea region	52
Table 14	Available power per meter wave front [kW/m]	54
Table 15	Mesh refinement levels	59
Table 16	Maximum error in NEMOH results	63
Table 17	Natural frequencies of HyWind and DC ₁ -D ₁ [Hz]	66
Table 18	Natural frequency of the isolated WEC	72
Table 19	Isolated WECs optimal PTO damping coefficient [ton-s/s]	73
Table 20	Isolated WECs absorbed power per sea state [kW]	74
Table 21	Isolated WECs absorbed energy per year [MWh/y]	74
Table 22	Isolated WECs absorption width [m]	74
Table 23	Natural frequencies of DC ₁ FOHWWECs	76
Table 24	DC ₁ -D ₁ optimal PTO damping coefficient [tons/s]	78
Table 25	DC ₁ -D ₂ and DC ₁ -D ₃ optimal PTO damping coefficient [tons/s]	79
Table 26	DC ₁ -D ₁ absorbed power per sea state [kW]	79
Table 27	DC ₁ -D ₂ absorbed power per sea state [kW]	79
Table 28	DC ₁ -D ₃ absorbed power per sea state [kW]	79
Table 29	DC ₁ -D ₁ absorption width [m]	80
Table 30	DC ₁ -D ₂ absorption width [m]	80
Table 31	DC ₁ -D ₃ absorption width [m]	80
Table 32	DC ₁ -D ₁ standard deviation of the nacelle acceleration [g]	80
Table 33	DC ₁ -D ₂ standard deviation of the nacelle acceleration [g]	81
Table 34	DC ₁ -D ₃ standard deviation of the nacelle acceleration [g]	81
Table 35	Performance variable values of DC ₁ FOHWWECs	82
Table 36	Natural frequencies of DC ₂ FOHWWECs	85

Table 37	DC2-D1 and DC2-D2 optimal PTO damping coefficient [tons/s]	87
Table 38	DC2-D3 optimal PTO damping coefficient [tons/s]	88
Table 39	DC2-D1 absorbed power per sea state [kW]	88
Table 40	DC2-D2 absorbed power per sea state [kW]	88
Table 41	DC2-D3 absorbed power per sea state [kW]	88
Table 42	DC2-D1 absorption width [m]	89
Table 43	DC2-D2 absorption width [m]	89
Table 44	DC2-D3 absorption width [m]	89
Table 45	DC2-D1 standard deviation of the nacelle acceleration [g]	89
Table 46	DC2-D2 standard deviation of the nacelle acceleration [g]	90
Table 47	DC2-D3 standard deviation of the nacelle acceleration [g]	90
Table 48	Performance variable values of DC2 FOHWWECS	91
Table 49	Natural frequencies of DC3 FOHWWECS	95
Table 50	DC3-D1 optimal PTO damping coefficient [tons/s]	98
Table 51	DC3-D2 optimal PTO damping coefficient [tons/s]	99
Table 52	DC3-D3 optimal PTO damping coefficient [tons/s]	99
Table 53	DC3-D1 absorbed power per sea state [kW]	99
Table 54	DC3-D2 absorbed power per year [kW]	99
Table 55	DC3-D3 absorbed power per year [kW]	100
Table 56	DC3-D1 absorption width [m]	100
Table 57	DC3-D2 absorption width [m]	100
Table 58	DC3-D3 absorption width [m]	100
Table 59	DC3-D1 standard deviation of the nacelle acceleration [g]	101
Table 60	DC3-D2 standard deviation of the nacelle acceleration [g]	101
Table 61	DC3-D3 standard deviation of the nacelle acceleration [g]	101
Table 62	Performance variable values of DC3 FOHWWECS	102
Table 63	Draft effect on $\lambda_{p(\text{avg})}$, as % of increase	109
Table 64	Draft effect on $\sigma_{aNa(\text{max})}$, as % of decrease	110
Table 65	DC2 common stability input	119
Table 66	FOWT DC2-D1 stability I/O	119
Table 67	FOWT DC2-D2 stability I/O	119
Table 68	FOWT DC2-D3 stability I/O	120
Table 69	DC3 common stability input	120
Table 70	FOWT DC3-D1 stability I/O	120
Table 71	FOWT DC3-D2 stability I/O	120
Table 72	FOWT DC3-D3 stability I/O	121
Table 73	DC1-D1 FOWT standard deviation of the nacelle acceleration [g]	122

Table 74	DC ₁ -D ₂ FOWT standard deviation of the nacelle acceleration [g]	123
Table 75	DC ₁ -D ₃ FOWT standard deviation of the nacelle acceleration [g]	123
Table 76	DC ₂ -D ₁ FOWT standard deviation of the nacelle acceleration [g]	123
Table 77	DC ₂ -D ₂ FOWT standard deviation of the nacelle acceleration [g]	123
Table 78	DC ₂ -D ₃ FOWT standard deviation of the nacelle acceleration [g]	123
Table 79	DC ₃ -D ₁ FOWT standard deviation of the nacelle acceleration [g]	124
Table 80	DC ₃ -D ₂ FOWT standard deviation of the nacelle acceleration [g]	124
Table 81	DC ₃ -D ₃ FOWT standard deviation of the nacelle acceleration [g]	124
Table 82	DC ₁ -D ₁ absorbed energy per year [MWh/y]	124
Table 83	DC ₁ -D ₂ absorbed energy per year [MWh/y]	125
Table 84	DC ₁ -D ₃ absorbed energy per year [MWh/y]	125
Table 85	DC ₂ -D ₁ absorbed energy per year [MWh/y]	125
Table 86	DC ₂ -D ₂ absorbed energy per year [MWh/y]	125
Table 87	DC ₂ -D ₃ absorbed energy per year [MWh/y]	126
Table 88	DC ₃ -D ₁ absorbed energy per year [MWh/y]	126
Table 89	DC ₃ -D ₂ absorbed energy per year [MWh/y]	126
Table 90	DC ₃ -D ₃ absorbed energy per year [MWh/y]	126
Table 91	NREL 5 MW wind turbine properties [35]	127

ACRONYMS

B	Ballast
BEM	Boundary Element Method
BFOWT	Bottom-Fixed Offshore Wind Turbine
CS	Coordinate System
CoG	Center of Gravity
CoB	Center of Buoyancy
D ₁	First draft level (shallowest)
D ₂	Second draft level
D ₃	Third draft level (deepest)
DC	Design Configuration
DOF	Degree of Freedom
EoM	Equation of Motion
EU	European Union
FOHWEC	Floating Offshore Hybrid Wind-Wave Energy Converter
FOWT	Floating Offshore Wind Turbine
GWS	Global Wave Statistics
JONSWAP	Joint North Sea Wind Project
MSL	Mean Sea Level
OTB	On the Base
OWC	Oscillating Water Column
PA	Point Absorber
PTO	Power Take Off
RAO	Response Amplitude Operator
RE	Renewable Energy
RNA	Rotor-Nacelle Assembly
SFC	Semi-submersible flap combination
SI	International system of units
STC	Spar Torus Combination
TLP	Tension Leg Platform
WEC	Wave Energy Converter
WPA	Water Plane Area
WT	Wind Turbine

SYMBOLS

Geometry and mass-related

D	Draft
CoB_z	Z coordinate of the center of buoyancy, from MSL
CoG_z	Z coordinate of the center of gravity, from MSL
d_{rat}	Hywind substructure diameter/OTB WT diameter ratio
f	Free-board
h_{arm}	Vertical distance from WEC's sphere to supporting arm
h_{na}	Vertical distance from CoG to nacelle
I_{yy}	Mass moment of inertia with respect to y axis
$l_{cyl-cyl}$	length between substructure cylinders
$l_{cyl-WEC}$	length between WT cylinder and WEC
m	Mass
m_b	Ballast mass
m_{bB}	Ballast mass in B cylinder(s)
m_{bWT}	Ballast mass in WT cylinder
∇	Displacement
∇_{wb}	Displacement with ballast
r_{cyl}	Radius of the substructure cylinder(s)
r_{WEC}	Radius of the WEC
$\rho_{s(eq)}$	Equivalent steel density
ρ	Density of sea water

Force-related

a	Hydrodynamic added mass coefficient
\underline{A}	Global added mass matrix for multiple floating bodies
A_{jk}^{ab}	Added mass matrix of body a due to the motion of body b
b	Hydrodynamic damping coefficient
b_{PTO}	PTO damping coefficient
\underline{B}	Global damping matrix for multiple floating bodies
B_{jk}^{ab}	Damping matrix of body a due to the motion of body b
c	Hydrostatic restoring coefficient
F_w	Wave excitation force
g	Gravity

Mooring-related

D_{moor}	Depth of fairlead
L_0	Unstretched line length
l_{moor}	Horizontal projection of the mooring line

Power, energy and performance-related

\bar{E}_{PTO}	Average energy absorbed for a given sea state in a year
J	Wave power level
λ_p	Absorption width
$\lambda_p^{(avg)}$	annual average absorption width
\bar{P}_{PTO}	Average power absorbed in one wave period
$\sigma_{aN\alpha}$	Standard deviation of nacelle acceleration
$\sigma_{aN\alpha}^{(avg)}$	annual average standard deviation of nacelle acceleration

$\sigma_{aNa(max)}$ Maximum standard deviation of nacelle acceleration

Stability-related

GM_t Transversal metacentric height
 GM_l Longitudinal metacentric height
 φ_{max} Maximum allowable heeling angle
 θ_{max} Maximum allowable trimming angle

Wave-related

c_g Group velocity
 c_w Wave velocity
 H Wave height
 H_s Significant wave height
 k Wave number
 λ Wave length
 m_n The n th-order moment of the spectrum
 μ Wave direction angle
 N_s Sea state yearly-occurrences
 N_{st} Sum of all sea state yearly-occurrences in the operational subset
 ω Angular wave frequency
 ϕ_w Wave velocity potential
 $S_\zeta(\omega)$ Wave spectrum
 $S_z(\omega)$ Heave motion spectrum
 T Wave period
 T_e Energy wave period
 T_p Peak period of the wave spectrum
 T_z Mean zero-crossing wave period
 ζ_a Wave amplitude

Subscripts

1 Surge motion
3 Heave motion
3r Relative heave motion
5 Pitch motion
aNa Horizontal acceleration of the nacelle
j Vector of j elements
k Vector of k elements
jk Matrix of j x k elements

Superscripts

a Referring to the WEC located on the positive y axis
b Referring to the WEC located on the negative y axis
c Referring to the FOHWWEC's substructure

INTRODUCTION

1.0.1 Background

Meeting the energy requirements of a steadily increasing global population is a major challenge. At the same time, the consequences of human induced climate change are compelling several countries to phase out fossil fuel as energy source. A total of 196 countries have pledged to the Paris Agreement, aiming at limiting warming to 1.5 to 2°C above pre-industrial levels [1].

Under this scenario, renewable energy (RE) sources have become one of the main pillars of the energy transition [2]. Offshore wind and ocean waves are two huge and predictable resources of RE. The industry related to the former is well established. As an example, Europe's cumulative offshore wind capacity reached 18499MW in 2018 [3]. In contrast, ocean wave energy is relatively untapped since its industry is in technological progression [4].

The offshore wind industry is moving fast towards floating technology (FOWT). The reason is the resource potential in deep waters. In Europe, 80% of the offshore wind resource is located in 60m or deeper waters, where bottom-fixed offshore wind turbines (BFOWT) are not an alternative [3].

Several FOWT substructure designs has been developed so far. Among them, four have reached a high level of technology readiness: Barge, Spar buoy, Semi-submersible and Tension Leg Platform (TLP) [3]. Examples of each of them are included in Figure 1.

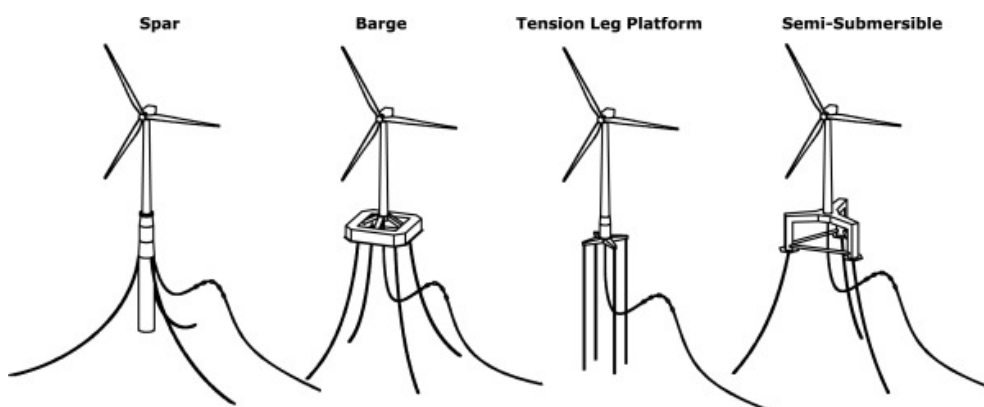


Figure 1: FOWT substructure designs [5]

The installation of FOWTs in farms requires extensive ocean areas. In the same area, ocean waves are transporting energy. Hence, it is logical to har-

vest wave energy, and share the structure and electric systems of the FOWT to reduce costs. Authors as Beerens [6] has named the combined system as floating offshore hybrid wind-wave energy converter (FOHWWEC).

Throughout the last decades, research effort has focused in studying how these systems can combine a Wave Energy Converter (WEC) with FOWTs. The relevant previous work on FOHWWECs is presented in section 2.1.

These studies have addressed the functionality, feasibility, optimization, control and survivability of FOHWWEC concepts. The majority considers a proven FOWT substructure to fit a certain type of WEC. Dynamic analyses in both, frequency and time domains, and laboratory experiments with models have been done. It has been proven that certain FOHWWECs besides adding wave power to the total power production, they also enhance the wind power absorption by increasing the substructure stability. Based on this summarized background, the following opportunities have been identified:

1. The studies investigated by the author have not considered the FOHWWEC concept as part of an extensive design space. In other words, an attempt to explore and compare the myriad design configurations that are possible in that space has not been found by the author.
2. Few studies have been able to deliver a comprehensive understanding on how certain parameters, intrinsic and extrinsic to the FOHWWEC system, influence its performance.

Both opportunities are extensive. There are several ways to explore the design space and, similarly, the FOHWWEC system has a large number of input parameters and performance variables. A scope definition is necessary and presented in the following section.

1.0.2 *General scope definition*

Based on the opportunities derived from the background review, a general definition of the scope can be performed. This general definition focuses only on the elements mentioned in the opportunities. Defining the scope of each of those elements is sufficient to establish the objectives. All the other detailed definitions of the scope are found in chapter 5.

1. **DESIGN SPACE SCOPE:** It consists of all FOHWWEC design configurations that can be created with two substructure floating stability principles: ballast-stabilization and buoyancy-stabilization. Stabilization can also be obtained with the mooring (e.g. TLP platforms), but it maximizes the resistance to motion, making it less attractive for the installation of heaving WECs. Therefore, it is not considered in this study.

These stability principles are used in other studies. For example, in the FOWT design space explorations of Hall et al. [7] and Tracy [8]. Since they used the principles on the FOWTs, it is decided to use them as well for the FOHWWECS. An extended definition of each stability principle is included in section 3.2.

Figure 2 has been included as a schematic representation of the FOHWWEC design space scope.

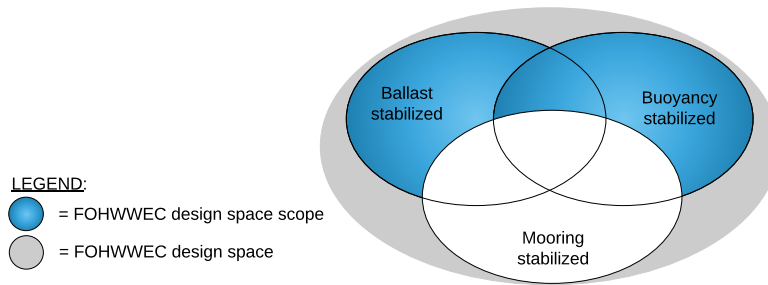


Figure 2: FOHWWEC design space scope

2. DESIGN CONFIGURATIONS (DC) SCOPE: From the myriad possibilities, three FOHWWEC DCs are selected; a ballast-stabilized (DC₁), a buoyancy stabilized (DC₃) and a mixed ballast-buoyancy-stabilized (DC₂). All of them with two spherical point absorber (PA) type WECs. The reason for the selection of a mixed DC is to obtain information on how the performance variables evolve from DC₁ to DC₃. The reason for the selection of spherical PAs is simplicity and the availability of experimental data/analytical formulations for them.

The design configurations and the WEC are described in detail in sections 5.1 and 5.2.

3. PERFORMANCE VARIABLES SCOPE: The performance variables refer to outputs from the FOHWWEC system that can be used to judge its performance. Since a FOHWWEC is a wind-wave hybrid, a FOHWWEC with outstanding performance scores well on both, wind and wave-related performance. Therefore, at least two performance variables are needed.

Since the FOHWWEC main objective is to produce power and this thesis must address hydrodynamics, the WEC's absorption width is selected as the wave-related performance variable. The absorption width is a measure of efficiency and it facilitates the comparisons between the DCs.

The wind-related performance variable is selected based on other research efforts. In references [8] and [7] it is explained that the horizontal nacelle acceleration could cause degradation of the turbine performance and damage to the equipment, specially at the blade roots. The blades in their flapwise direction are easily excited by nacelle accelerations and this leads to high bending moments. As it is applied by Hall in reference [7], the concept of *significant* amplitude of the nacelle acceleration is used. This is the same as the standard deviation of the nacelle acceleration. Therefore, this is selected as the second performance variable used in the present research.

Both performance variables are defined in detail in section 5.10.2.

From now onwards and for the present study, the performance of a FOHWWEC is just the combination of the two performance variables selected above. Then, performance improvement means higher absorption widths and lower standard deviations of the nacelle acceleration.

4. **INPUT PARAMETERS SCOPE:** The input parameters refer to inputs into the FOHWWEC system. They can be intrinsic or extrinsic to the system. For example, a geometrical parameter of the FOHWWEC is intrinsic, but a certain wind-wave direction is extrinsic. The input parameters have an impact on the performance variables and that impact is assessed.

Initially, the author thought about three input parameters: draft, WEC position on the substructure and wave direction. Nevertheless, to simplify the study, only the draft is included in the present work.

5. **SEA REGION SCOPE:** It is necessary to select a site for the simulations. The North Sea region is selected due to the availability of wave data and its well known and widely used wave spectra. Precisely, the JON-SWAP spectral formulation is the one selected for the present research. More details are found on section 5.8.

1.0.3 *Research objectives*

The opportunities derived from the background review and the definition of the scope allow to establish the main and secondary objectives of the present research.

- *Main objective:* To demonstrate which of the three considered FOHWWEC design configurations, based on the floating stability principle, provides the maximum efficiency in wave power absorption and the minimum variability of the horizontal nacelle acceleration.

- *Secondary objective:* To study the effect of the draft on the absorption width and the standard deviation of the nacelle acceleration of each FOHWWEC design configuration.

1.0.4 Method outline

To achieve each of the objectives described in subsection 1.0.3 a methodology is required. In this section the method is outlined. General aspects as well as specific steps are presented. A flowchart of the method is included as supporting material in Figure 3.

1.0.4.1 General aspects

The method is based on theory. That means no experimental tests. There are two reasons for this. First, the present work deals with design space exploration. That action is associated with the conceptual design stage, where it is not normally necessary to perform tests. Second, there is limited time to develop both, theoretical and experimental studies. The fundamental theory is Potential Flow, solved numerically with a Boundary Element Method (BEM) in the open source program NEMOH.

The model selected for the analysis is a linear frequency domain model. As explained by Beerens [6], this domain is faster in the evaluation of different sea states when compared with the time domain. It also portrays the influence of the natural frequencies in the dynamic response. This selection implies, as explained by Merigaud and Ringwood [9], that if non-linearities, such as non-linear Froude-Krylov and viscous forces, non-linear characteristics in the mooring, the PTO system or in the control strategy play a significant role in the WEC's dynamics, those effects are not captured by the linear model.

The analysis presented in this study is hydrodynamic with the WT rotor in parked condition. That means no aerodynamic loads are included. The recommendation is made for future research to include these loads and assess their impact on the performance variables.

A computer program, developed by the author, automates the calculation of the motion and performance variables for the three design configurations. The program is named *FOHWWEC Analysis Program* and it consists of three components, that are described in the following paragraphs.

- *The Salome-Nemoh interface:* It communicates and operates the open source programs Salome and Nemoh. Salome is used to model the underwater surfaces and to mesh them. NEMOH is employed to solve the flow on those surfaces, providing the hydrodynamic coefficients (added mass and damping) and the wave excitation forces (Froude-Krylov and diffraction components).

- *The motion and performance calculation module*: It is the main module. It receives input from the secondary modules to resolve the linearized Equations of Motion (EoM) and to calculate the performance variables.
- *Secondary modules*: They support and provide input to the main module. For example, the module calculating the hydrostatic stability of the FOHWWEC.

Specific details of the *FOHWWEC Analysis Program* are included in the Appendix C.

1.0.4.2 *Specific steps*

There is a minimum number of steps necessary to achieve the research objectives. Those steps are presented in the method flowchart in Figure 3.

Chapter 5 is dedicated to the description of each methodology step, including decisions and assumptions with their supporting arguments.

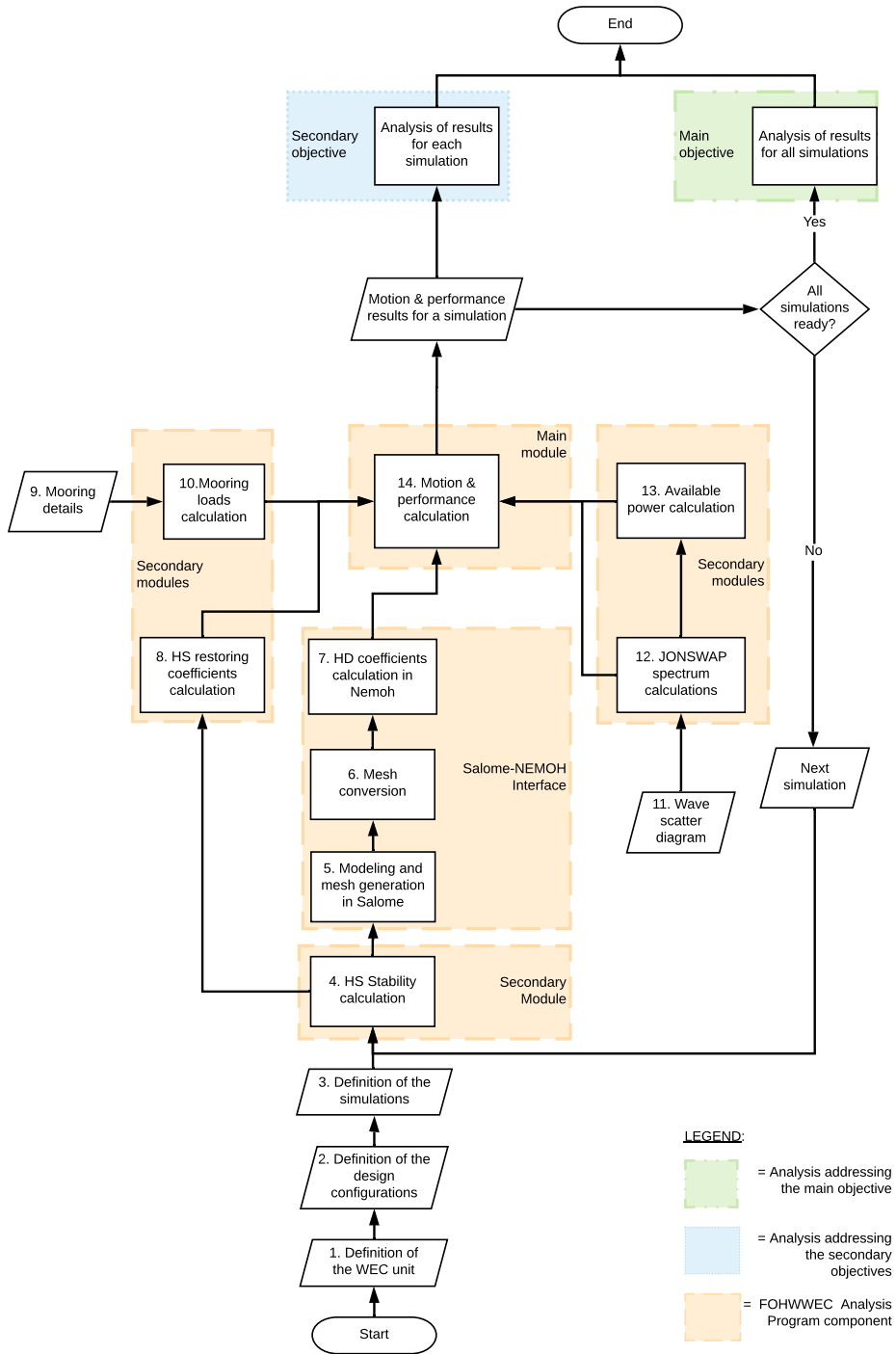


Figure 3: Method flowchart

1.0.5 *Structure of the thesis*

The present thesis report is divided in eight chapters and three appendices. The most relevant information is included in the sections. The information that is considered supplementary is written in the appendices.

The second chapter presents the state of the art of FOHWWECC and FOWT research and FOWT commercial devices, that inspired the present study. The third and fourth chapters describe, in a condensed manner, the terminology definitions, concepts, principles and physical laws supporting the research work. The fifth chapter describes how the methodology is actually applied, including relevant decisions and assumptions with its supporting arguments. The sixth chapter includes verification and validation actions on the calculations. The seventh chapter is the analysis of the results for each simulation and for all simulations combined. The eight and last chapter corresponds to the conclusions and recommendations.

The first appendix encompasses all additional results that, although relevant for the study conclusions, would make the sections too extensive if included. The second appendix corresponds to the wind turbine properties. The last appendix serves as an user guide for the *FOHWWECC Analysis Program* developed by the author as a byproduct of the research.

STATE OF THE ART

2.1 RESEARCH ON FOHWWECS

The research on FOHWWECS has been more active in the last decade. In this section, the most relevant studies from that period are presented.

In 2010 Beerens [6] studied the behavior of the semi-sub FOWT 'Wind-Float', coupled with three WEC buoys moving over an inclined guide. Three important conclusions were obtained. First, the buoys cause a decrease of the FOWT's heave RAO. Second, for low wave periods, the absorbed power by heaving/surging buoys is three times larger than by heaving buoys. Third, wave diffraction affects the power absorbed by the buoys.

In 2011, Peiffer et al. combined the WindFloat platform with a sphere [10] and then Aubault et al. with two Oscillating Water Columns (OWC) [11]. See Figures 4 and 5. Both performed tests and had similar values for the obtained mechanical power in the form of normalized capture width. Also the WEC was found to have minimal influence on the platform motions.



Figure 4: Sphere on 'WindFloat' [10]



Figure 5: OWCs on 'WindFloat' [11]

The period from 2010 until 2014 was influenced by the European Union (EU) supported FP7 MARINA Project. It consisted in an effort to study combined offshore RE systems [12], among them the FOHWWEC. From ten pre-selected concepts, only four remained: The Spar-Torus combination (STC), the Semi-sub flap combination (SFC), the Semi-sub multiple point absorbers (PA) combination, based on the W2Power concept, and a floater with an array of OWCs [12]. Figure 6 shows the selected systems.

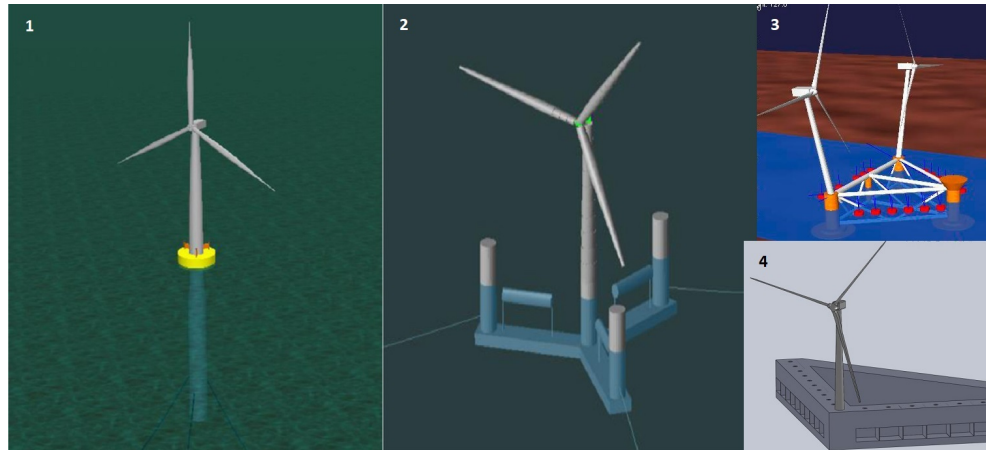


Figure 6: MARINA FP7 Project's selected hybrid concepts: 1-STC, 2-SFC [13].
3-W2Power, 4-OWC array [12]

The STC concept was analyzed by Muliawan et al. [14] in 2012. It was inspired by the HyWind FOWT and the WEC Wavebob. A more stable pitch motion was produced by adding the torus, allowing 10% higher power production compared to the WT alone. In 2017, research by Wan et al. [15] showed large forces on the torus connection due to slamming effects.

The SFC concept was analyzed by Michailides et al. [16] in 2014. It resulted in an increased power production without a significant effect on the motions of the platform. In 2016 [17] the research continued with experimental results validating these conclusions.

The W2Power combines a platform with the capacity to carry two 4MW WTs and an array of PAs with the Power Take-Off (PTO) in one of the columns. Extensive research has been done, as in reference [18].

In 2013 Soulard et al. [19] performed a preliminary design of a semi-sub platform combined with pitching WECs. For specific sea conditions, the WECs extracted an average annual power of 1.76MW. This is extracted in a year by a 5MW WT with 30% capacity factor. Nevertheless, loads transmitted to the structure were above allowable limits. That led to a recommendation to consider WECs and their loads earlier in the design process.

During 2015 two EU Projects defined the research context. First, the MERMAID Project supported the integration of a WT with three OWCs (See Figure 7 and reference [20]). Second, the POSEIDON Project, aiming to bring the proven concept Poseidon to commercial maturity. This hybrid demonstration platform is the first of its kind to deliver wind-wave power to the grid. It consists on two or three WTs over a floating platform, pivoting around a turret mooring, combined with pitching WECs (See Figure 8).



Figure 7: 'MERMAID' platform [20]



Figure 8: 'Poseidon 37' platform [21]

In 2016 the EU-supported UPWAVE Project started. The project's main objective is to demonstrate the feasibility of a 1MW wave energy converter integrated in an offshore wind turbine farm. That is not necessarily a hybrid unit, but at least WEC and WT in the same area.

One UPWAVE sub-project aims to prove the WaveStar C6-1000 device, developed by the danish company Wave Star AS, following a successful pilot installed in Hanstholm (See Figure 9). Although the platform is fixed to the sea bottom, the research effort in reference [22] adapts the WaveStar concept to the HyWind FOWT. This work shows that by choosing a proper PTO, it is possible to minimize the effect of the WEC on the WT performance, while adding wave power to the production.



Figure 9: WaveStar [23]

Additional research initiatives have focused on different FOWTs, WECs or purpose. Among them, Bachynsky and Moan [24] (2013) studied a TLP supporting a 5MW wind turbine and three point absorbers, also as part of the MARINA Project. In the same year, Borg et al. [25] investigated the WEC's optimization to reduce the FOWT's motions. In 2017 Fabregas et al. [26] worked on the interaction between multiple buoy PAs, inspired by the WaveStar.

2.2 RESEARCH ON FOWTS

In this section two relevant research efforts addressing the design space exploration for FOWTs are described. Since the present study is a start point for the same type of exploration for FOHWECs, it is useful to understand the method, results and conclusions of those two studies.

Parametric design of FOWTs by C. Tracy

This study [8] consists in a simple geometrical parametric definition of the FOWT design space. The author selects a concrete ballasted cylinder as design configuration and its draft and radius as geometrical parameters. Catenary and TLP mooring are analyzed and the WT NREL 5MW is used.

Tracy's method is to evolve the cylinder's shape from a short radius and deep draft (ballast-stabilized), as in Figure 10, towards a large radius and shallow draft (buoyancy-stabilized) as in Figure 11. The evaluated performance variables are the standard deviation of the horizontal nacelle acceleration and the mooring line tension.



Figure 10: Ballast-stabilized FOWT



Figure 11: Buoyancy-stabilized FOWT

The following findings are reported concerning the nacelle acceleration:

1. A trend is identified where increasing displacement decreases the nacelle acceleration. According to Tracy's explanation, a more massive structure has a lower natural frequency, that can be lower than the peak frequency of the sea state. Therefore, the nacelle accelerations are reduced.
2. The TLP designs produce lower values for the standard deviation of the nacelle acceleration than the catenary designs.

Hydrodynamics-based FOWT optimization by Hall

Hall's research effort [7] tries to overcome the limitation of adhering to certain physical design assumptions. For example, Tracy's study [8] is limited to a cylindrical shape for all design configurations.

In order to accomplish this, a linear combination of the hydrodynamic, hydrostatic and mass coefficients of six substructure geometries is proposed and the resulting combinations are optimized for minimum standard deviation of the horizontal nacelle acceleration. Two mooring systems are analyzed: catenary and TLP. The six geometries are presented in Figure 12.

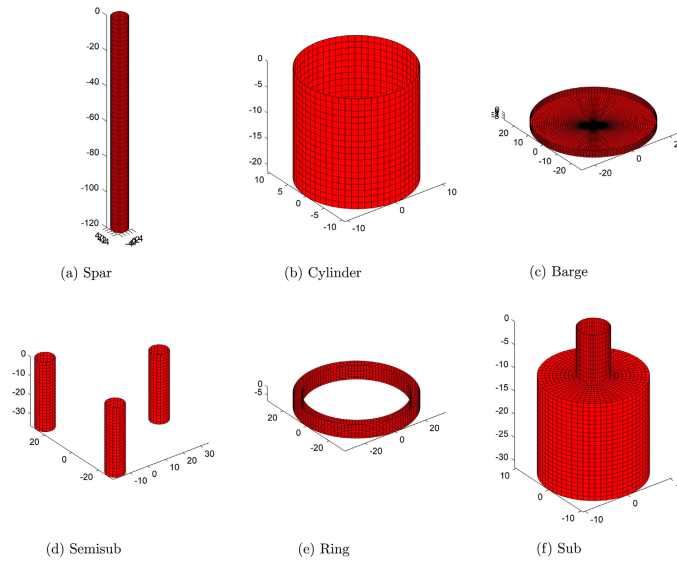


Figure 12: Hall's basic substructure geometries

The spar-type geometry establishes a displaced volume that is kept constant for all other designs. This is a way of maintaining approximate cost equivalence between platforms.

The findings obtained for catenary mooring are the following:

1. Submersed volume (Sub or spar) combined with widely distributed WPA (Semisub) provide the lowest nacelle accelerations. The Semisub provides hydrostatic stability, but also significant wave excitation. Adding submersed volume lowers the natural frequencies and keep them away from the active wave frequencies. It is possible that this combination could also take advantage of phase cancellation in the excitation forces.
2. It is difficult to obtain a physical interpretation of the optimal configuration. The results support an interpretation where both geometries are present, but scaled down. Nevertheless, this does not capture the inherent nonlinearities in how the hydrodynamic coefficients are determined from the geometry. Besides this, the hydrodynamic interactions between the geometries are not considered by the linear combination.

DYNAMICS OF FLOATING STRUCTURES

3.1 HYDRODYNAMIC CLASSIFICATION

A floating offshore structure is subjected to different force mechanisms (inertia, gravity and viscous) and it is often impossible to include all of them simultaneously in one mathematical model [27]. It is useful then to determine if viscous effects or potential flow effects are dominating. Here potential flow is understood as a flow that can be treated as inviscid and within potential flow effects, wave diffraction and radiation are included [28].

Faltisen presents in reference [28] a graph to determine if mass forces, viscous forces or wave diffraction forces are dominating. The graph, here in Figure 13, is based on results for horizontal wave forces on a vertical circular cylinder standing on the sea floor and penetrating the free surface. The cylinder with diameter D is subjected to regular waves with H and λ .

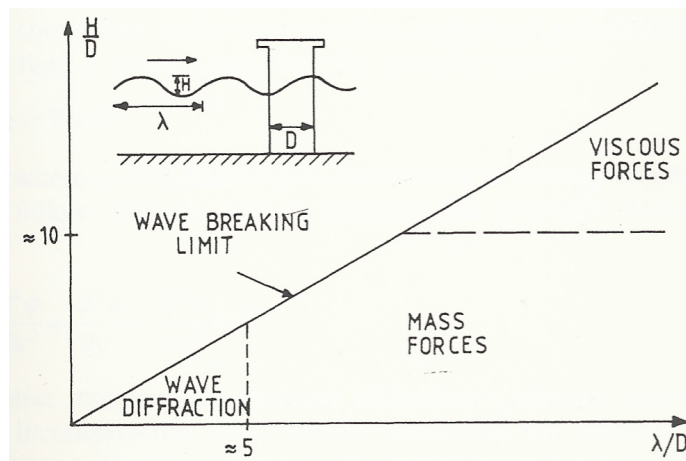


Figure 13: Relative importance of mass, viscous drag and diffraction forces on marine structures [28]

Now, using the graph for the present work, DC_1 , DC_2 and DC_3 have cylinder diameters of 10m and 12m. Considering an extreme wave of $H = 30\text{m}$ and $\lambda = 300\text{m}$, $H/D \approx 3$ and $\lambda/D \approx 30$. That means the hydrodynamic forces dominating are the mass forces; in other words, the forces in phase with the undisturbed local fluid acceleration [28]. Diffraction and viscous effects are less significant. Nevertheless, for high wave frequencies with λ values of 30m and H between 1.5m and 4.5m, which are actual waves within the operational range, $H/D \approx 0.3$ and $\lambda/D \approx 3$. That means wave diffraction effects are expected to be important for frequencies above $\omega = 1.23\text{rad/s}$.

In consequence, a BEM solver, like NEMOH that is based on potential theory is an appropriate selection for the analysis developed in this thesis.

3.2 FLOATING STABILITY PRINCIPLES

Floating structures supporting other devices, like wind turbines, are named from now onwards within the present work as floating substructures. There are three proven strategies for providing stability to floating substructures and they are described in reference [7] as follows:

- **Buoyancy-stabilized designs:** They rely on a large water plane area moment of inertia to raise the substructure's metacenter (MC) above its center of gravity (CoG). Also known as semisubmersibles, these substructures are often in the shape of a barge or an array of three or more vertical cylinders connected with a truss structure. Their shallow drafts allow simple installation and flexible siting. The lack of ballast reduces size and material requirements. The disadvantage is that the large water plane area (WPA) can make the substructure susceptible to severe wave-induced motions. Heave plates are often added to reduce wave-induced motions [7]. For graphical reference see Figure 1.
- **Ballast-stabilized designs:** In these substructures a deep draft and heavy ballast locate the CoG well below its center of buoyancy. A spar-buoy configuration (a long slender vertical cylinder) is normally used. With a minimal water plane area, resistance to wave-induced motions is increased, but the amount of ballast adds size and raises costs. Beside this, the large draft limits siting and installation options [7]. For graphical reference see Figure 1.
- **Mooring-stabilized designs:** These substructures are known as Tension Leg Platforms (TLPs). They make use of taut often-vertical mooring lines to hold it below its neutral buoyancy depth. The pretension on the lines effectively counters heaving and pitching motions. With a minimal water plane area and taut mooring lines, the TLP is extremely resistant to pitching motions. Its disadvantages are costs and siting limitations associated with the high tension mooring system. Moreover, additional buoyancy is needed to counter the mooring line tension [7]. For graphical reference see Figure 1.

3.3 RIGID SINGLE BODY IN REGULAR WAVES

The FOWT and the isolated WEC are examples of rigid bodies. Their rigidity is an assumption that works well for the analysis performed in this research.

In order to describe the EoM for a single floating body in regular waves, it is necessary to define the coordinate systems, the body motions involved and the concept of motion superposition.

The theory described here is mainly based on chapter 6 of reference [27].

Coordinate systems

Two right-handed orthogonal Coordinate Systems (CS) are used to define the single body motions. They are depicted in Figure 14.

1. An earth-bound CS, $O(x, y, z)$: The plane (x, y) lies at the equilibrium position of the CoG in calm sea. The positive x axis is in the wave direction $\mu = 0$. The wave direction is defined by the counter-clockwise angle μ .
2. A body-bound CS, $G(x_b, y_b, z_b)$: This CS is anchored to the body with its origin at the CoG.

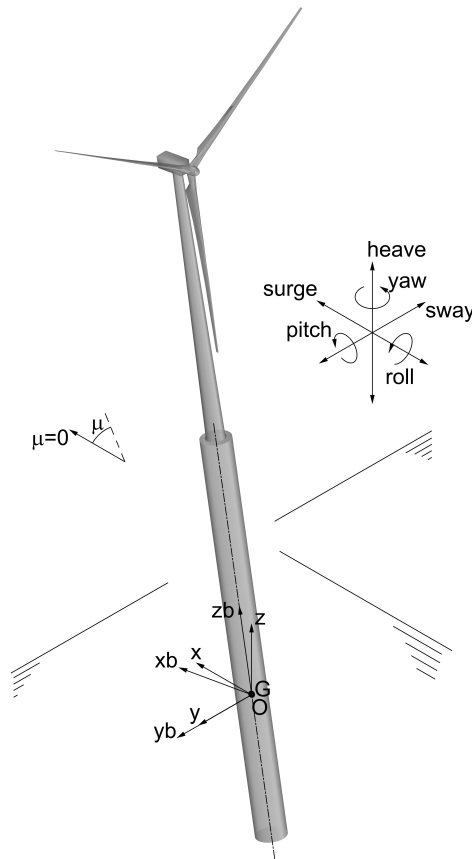


Figure 14: Coordinate systems

Wave-frequency motions

The oscillatory wave-frequency translations of a floating body CoG are surge, sway and heave. The oscillatory angular motions are roll, pitch and yaw (see Figure 14).

Since in the present research effort only 0 deg waves are considered, only hydrodynamic loads are estimated and all bodies are symmetric with respect to the x axis, the body motion can be described in terms of surge, heave and pitch, which are also known as symmetric motions, because the displacement of a point to starboard has the same motion as the mirrored point to port side [27].

The symmetric oscillatory wave-frequency motions are defined as harmonic functions in the earth-bound CS, as follows:

$$x = x_a \cos(\omega t + \epsilon_x \zeta) \quad (1)$$

$$z = z_a \cos(\omega t + \epsilon_z \zeta) \quad (2)$$

$$\theta = \theta_a \cos(\omega t + \epsilon_\theta \zeta) \quad (3)$$

where ϵ is the phase angle of the motion with respect to the undisturbed wave at the CoG.

Here the exponential form of a complex number can be used to express the displacements in a way that facilitates the calculations. It is known that a complex number z can be written as:

$$z = r e^{i\omega} = r (\cos(\omega) + i \sin(\omega)) \quad (4)$$

Therefore,

$$x = \Re\{x_a e^{i\omega t} e^{i\epsilon_x \zeta}\} \quad (5)$$

$$z = \Re\{z_a e^{i\omega t} e^{i\epsilon_z \zeta}\} \quad (6)$$

$$\theta = \Re\{\theta_a e^{i\omega t} e^{i\epsilon_\theta \zeta}\} \quad (7)$$

where \Re refers to the real part of the complex number.

The harmonic velocities and accelerations are found by taking the derivatives of equations 5, 6 and 7. For example, heave velocity and acceleration are given by:

$$\dot{z} = \Re\{i\omega z_a e^{i\omega t} e^{i\epsilon_z \zeta}\} = \Re\{i\omega z\} \quad (8)$$

$$\ddot{z} = \Re\{-\omega^2 z_a e^{i\omega t} e^{i\epsilon_z \zeta}\} = \Re\{-\omega^2 z\} \quad (9)$$

Motions superposition

The motions superposition is a linear transformation from the body-bound CS to the earth-bound CS. In consequence, the rotation angles, such as θ , are assumed to be small and the following can be written:

$$\cos(\theta) \approx 1 \quad (10)$$

$$\sin(\theta) \approx \theta \quad (11)$$

The specific motion superposition used in the present work to obtain the horizontal nacelle acceleration is based on the following transformation of the surge displacement:

$$x_p = x + z_b \dot{\theta} \quad (12)$$

where x_p is the surge motion of a point p on the body and z_b is the z coordinate of the point p in the body-bound CS.

Equation of motion (1 DOF)

The simplest case of a rigid body in regular waves is when only one DOF is allowed. For example, a heaving hemisphere. In this case, the problem can be modelled as a mass-spring-damper system as shown in Figure 15.

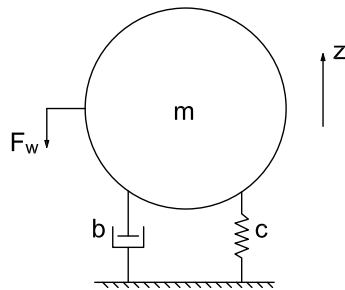


Figure 15: Mass-spring-damper model

A mass m , connected to a spring and a damper, experiences a wave excitation force, due to the incident waves and the diffracted waves. If Newton's second law is applied to this system, it results in equation 13 [6].

$$F_I = F_{res} + F_{rad} + F_w \quad (13)$$

where,

$$\begin{aligned}
F_I &= \text{Inertia forces} \\
F_{res} &= \text{Restoring forces} \\
F_{rad} &= \text{Hydrodynamic radiation forces} \\
F_w &= \text{Hydrodynamic wave excitation forces}
\end{aligned}$$

The restoring forces correspond to the hydrostatic restoring force in heave. It can be expressed as $F_{res} = -c \cdot z$. The hydrodynamic radiation forces consist of a damping part, in phase with the heave velocity, and an added mass part, in phase with the heave acceleration $F_{rad} = -(b \cdot \dot{z} + a \cdot \ddot{z})$. Finally, the equation of the heaving motion can be written as follows:

$$(-\omega^2(m + a) + i\omega b + c) \cdot z = F_w \quad (14)$$

where the definitions 8 and 9 has been used. The added mass coefficient (a), the wave radiation damping coefficient (b) and the wave excitation force (F_w) are frequency dependent.

Now, using equation 6, a similar complex formulation for F_w , and dividing both sides of the equation by the wave amplitude ζ_a , the following expression is obtained:

$$(-\omega^2(m + a) + i\omega b + c) \cdot \frac{z_a}{\zeta_a} e^{i\omega t} e^{i\epsilon_{z\zeta}} = \frac{F_{wa}}{\zeta_a} e^{i\omega t} e^{i\epsilon_{F\zeta}} \quad (15)$$

where it is understood that the real part of the complex number is taken on both sides of the equation.

The complex amplitudes are defined for the heave motion and for the wave force, as follows:

$$\widetilde{z}_a = \frac{z_a}{\zeta_a} e^{i\epsilon_{z\zeta}} \quad (16)$$

$$\widetilde{F}_a = \frac{F_{wa}}{\zeta_a} e^{i\epsilon_{F\zeta}} \quad (17)$$

Finally, solving equation 15 and defining the Response Amplitude Operator (RAO) as the ratio between the heave motion amplitude and the wave elevation, lead to the following expressions:

$$\widetilde{z}_a = \frac{\widetilde{F}_a}{(-\omega^2(m + a) + i\omega b + c)} \quad (18)$$

$$\frac{z_a}{\zeta_a} = \text{RAO} = \sqrt{\Re\{\widetilde{z}_a\}^2 + \Im\{\widetilde{z}_a\}^2} \quad (19)$$

$$\epsilon_{z\zeta} = \text{Phase angle} = \arctan\left(\frac{\Im\{\widetilde{z}_a\}}{\Re\{\widetilde{z}_a\}}\right) \quad (20)$$

The RAO is a characteristic of the system and it states that the heave amplitude is proportional to the wave amplitude. In other words, there is a linear relation between them. The phase angle is also a characteristic of the system and it does not depend on the wave amplitude. Both, RAO and phase angle, are also known as frequency characteristics and their dependence on frequency comes from the added mass and damping dependence on frequency.

Another important characteristic of the system, also dependant on the wave frequency, is the natural frequency. It is normally determined through a free-decay test. Making the connection with the floating hemisphere, obtaining its natural frequency means to induce a heave motion and analyze how it decays. From the free-decay EoM, the definition of the natural frequency (ω_n) arises with the following expression:

$$\omega_n = \sqrt{\frac{c}{m + a}} \quad (21)$$

Equation of motion (3 DOFs)

Moving on to consider further degrees of freedom and in particular 3 DOFs (surge, heave and pitch) for the dynamic analysis of the FOWT in 0 degree waves, a similar analogy with a mass-spring-damper system can be used and Newton's second law is also the basis. The difference is that there can be interaction effects between the DOFs. For example, a restoring pitch moment can be generated due to the heave motion of the body. Then, to consider those interactions, the EoM terms become matrices and vectors, producing the following expression:

$$(-\omega^2(M_{jk} + A_{jk}) + i\omega B_{jk} + C_{jk}) \cdot \eta_k = F_{w_j} \quad (22)$$

where, $j = 1,3,5$ and $k = 1,3,5$ representing surge (1), heave (3) and pitch (5) motions and directions.

The subscripts j and k indicate that the element is either a one-dimensional vector, as the vector of motions (η_k) or a two-dimensional matrix, as the mass matrix (M_{jk}).

The matrices and vectors involved are presented here making all their components visible:

$$M_{jk} = \begin{bmatrix} m_{11} & 0.0 & 0.0 \\ 0.0 & m_{33} & 0.0 \\ 0.0 & 0.0 & I_{55} \end{bmatrix} \quad (23)$$

$$A_{jk} = \begin{bmatrix} a_{11} & a_{13} & a_{15} \\ a_{31} & a_{33} & a_{35} \\ a_{51} & a_{53} & a_{55} \end{bmatrix} \quad (24)$$

$$B_{jk} = \begin{bmatrix} b_{11} & b_{13} & b_{15} \\ b_{31} & b_{33} & b_{35} \\ b_{51} & b_{53} & b_{55} \end{bmatrix} \quad (25)$$

$$C_{jk} = \begin{bmatrix} c_{11} & 0.0 & c_{15} \\ 0.0 & c_{33} & c_{35} \\ c_{51} & c_{53} & c_{55} \end{bmatrix} \quad (26)$$

Here it is important to mention that the C_{jk} matrix consists of the hydrostatic restoring matrix $C_{jk_{hyd}}$ and the mooring restoring matrix $C_{jk_{moor}}$. In equation form:

$$C_{jk} = C_{jk_{hyd}} + C_{jk_{moor}} \quad (27)$$

$$\eta_k = \begin{bmatrix} \eta_1 \\ \eta_3 \\ \eta_5 \end{bmatrix} \quad (28)$$

$$F_{w_j} = \begin{bmatrix} F_{w_1} \\ F_{w_3} \\ F_{w_5} \end{bmatrix} \quad (29)$$

Now, in a similar way as for the 1 DOF case, the motion and the wave-excitation force vectors can be written in a complex form:

$$\eta_k = \Re\{\tilde{\eta}_{\alpha_k} e^{i\omega t}\} \quad (30)$$

$$F_{w_j} = \Re\{\tilde{F}_{aw_j} e^{i\omega t}\} \quad (31)$$

Finally, the system of equations is solved for the complex amplitudes of the motions $\tilde{\eta}_{\alpha_k}$ and from there equations similar to 19 and 20 can be used for each of the motions.

Regarding the natural frequency, a difference appears in comparison with the 1 DOF case. A natural frequency expression that arises just from manipulating the terms of the free-decay EoM can not be obtained. Then, it is necessary to first state the free-decay problem as follows:

$$(-\omega^2(M_{jk} + A_{jk}) + C_{jk}) \cdot \eta_k = 0_j \quad (32)$$

where 0_j is just a vector with three components equal to zero.

Then, using the complex form of η_k and writing the system of equations 32 in an equivalent form, the following is obtained:

$$C_{jk}(M_{jk} + A_{jk})^{-1} \cdot \tilde{\eta}_{\alpha_k} = \omega^2 \cdot \tilde{\eta}_{\alpha_k} \quad (33)$$

The expression 33 is known as an eigenequation. It relates an eigenvector ($\tilde{\eta}_{\alpha_k}$) with its eigenvalues (ω^2). Just saying that ω^2 is ω_n^2 provides an equation to obtain the natural frequency for each DOF in the system.

3.4 RIGID MULTI-BODIES IN REGULAR WAVES

Based on the previous section the EoM is now adapted for multiple floating bodies. To accomplish this, a procedure similar to the one used by Vasilikis in reference [29], is followed.

First, it is considered that the bodies are not mechanically connected with each other. In that way, there is only hydrodynamic interaction between them. The number of floating bodies is also established to be three and they are labeled a, b, c . Three is precisely the amount needed for the analysis of the FOHWECs in the present work. The EoM is then the following:

$$(-\omega^2(\underline{\mathbf{M}} + \underline{\mathbf{A}}) + i\omega\underline{\mathbf{B}} + \underline{\mathbf{C}}) \cdot \underline{\eta} = \underline{\mathbf{F}}_w \quad (34)$$

This equation seems to be the same as equation 22, but the difference are the matrices of coefficients, which in this case are global matrices of coefficients, indicated by the under-bar. These matrices include diagonal matrices, such as A_{jk}^{aa} and off-diagonal matrices, such as A_{jk}^{ab} . The off-diagonal ones are also known as hydrodynamic interaction matrices.

A hydrodynamic interaction matrix example is presented here:

$$A_{jk}^{ab} = \begin{bmatrix} a_{11}^{ab} & a_{13}^{ab} & a_{15}^{ab} \\ a_{31}^{ab} & a_{33}^{ab} & a_{35}^{ab} \\ a_{51}^{ab} & a_{53}^{ab} & a_{55}^{ab} \end{bmatrix} \quad (35)$$

The meaning of the subscripts and superscripts in the matrix components are explained with two examples:

- a_{51}^{ab} = added mass on body a in the pitch direction due to the motion of body b in the surge direction.
- a_{13}^{ab} = added mass on body a in the surge direction due to the motion of body b in the heave direction.

Then, going a couple of levels upwards, an example of a global added mass matrix is presented:

$$\underline{A} = \begin{bmatrix} A_{jk}^{aa} & A_{jk}^{ab} & A_{jk}^{ac} \\ A_{jk}^{ba} & A_{jk}^{bb} & A_{jk}^{bc} \\ A_{jk}^{ca} & A_{jk}^{cb} & A_{jk}^{cc} \end{bmatrix} \quad (36)$$

Since for all FOHWWECS there is symmetry in the geometry and in the wave loading, some interaction matrices are equal to each other, as follows:

$$A_{jk}^{ab} = A_{jk}^{ba}, \quad A_{jk}^{ac} = A_{jk}^{bc}, \quad \text{and} \quad A_{jk}^{ca} = A_{jk}^{cb} \quad (37)$$

The relations established by equation 37 are also applicable for the radiation damping global matrix \underline{B} .

Now, the effect of the mechanical connections between the bodies needs to be included. The mechanical connections are divided in two types:

1. The connection that completely restricts the motion. The consequence is that the two connected bodies experience the same motion. This is the case for surge (η_1) and pitch (η_5), that are the same for substructure and WECs.
2. The flexible connection that allows for relative motion between the bodies. The consequence is that the two connected bodies experience a coupled motion. This is the case for the heave motion. The WECs can move relative to the substructure because they are attached to the substructure by the flexible PTO connection. In the following section it is explained how the dynamics of the system are transformed by this connection.

3.5 TWO DOFS SPRING-DAMPER MODEL

The floating substructure, the floating spherical PA type WEC and the PTO connection can be modeled by the system depicted in Figure 16.

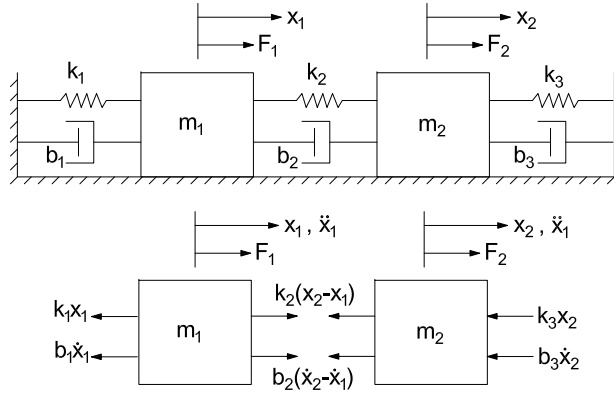


Figure 16: 2 DOFs spring-damper model

where the following analogy can be established:

- m_1 = WEC's mass
- m_2 = Substructure's mass
- k_1, b_1 = WEC's hydrostatic restoring and hydrodynamic damping coefficients
- k_3, b_3 = Substructure's hydrostatic restoring and hydrodynamic damping coefficients
- k_2, b_2 = PTO mechanical spring and damping coefficients

If it is assumed that both bodies are translating and accelerating in positive x direction, and that $x_2 > x_1$, $\dot{x}_2 > \dot{x}_1$, then the following two coupled EoMs are generated:

$$m_1 \ddot{x}_1 + (b_1 + b_2) \dot{x}_1 - b_2 \dot{x}_2 + (k_1 + k_2)x_1 - k_2 x_2 = F_1 \quad (38)$$

$$m_2 \ddot{x}_2 - b_2 \dot{x}_1 + (b_2 + b_3) \dot{x}_2 - k_2 x_1 + (k_2 + k_3)x_2 = F_2 \quad (39)$$

Based on these two equations, taking x_1 as the heave motion of the WEC ($\eta_{3\text{WEC}}$) and x_2 as the heave motion of the substructure (η_3), and remembering that no PTO mechanical spring is considered (See section 5.1.2), the matrices B_{jk}^{aa} , B_{jk}^{bb} and B_{jk}^{cc} can be modified to add the mechanical damping terms indicated by equations 38 and 39.

3.6 RESPONSE IN IRREGULAR WAVES

The previous sections have described different versions of the EoM in regular waves. Solving those equations means to obtain the RAO for each DOF. In this section it is explained how those RAOs are transformed to obtain the

response of the floating body in irregular waves. The description presented here is based on Chapter 6 of reference [27].

First, the heave motion spectrum is defined. It is done by analogy with the wave spectrum definition (equation 55), as follows:

$$S_z(\omega) \cdot d\omega = \frac{1}{2} z_a^2(\omega) \quad (40)$$

Second, this equation is multiplied and divided by ζ_a^2 , obtaining:

$$S_z(\omega) \cdot d\omega = \left| \frac{z_a}{\zeta_a}(\omega) \right|^2 \frac{1}{2} \zeta_a^2 \quad (41)$$

Finally, using the definition 55:

$$S_z(\omega) = \left| \frac{z_a}{\zeta_a}(\omega) \right|^2 S_\zeta(\omega) \quad (42)$$

where,

$$\left| \frac{z_a}{\zeta_a}(\omega) \right| = \text{RAO}_3 \quad (43)$$

These equations are valid for any RAO. That means, they are also used in the present thesis with the WEC relative heave RAO (RAO_{3r}) and with the horizontal nacelle acceleration RAO (RAO_{aN_a}).

WAVE POWER

4.1 DESCRIPTION OF WAVES

Regular and irregular waves

A wave can be defined as the profile of the surface elevation between two successive downward zero-crossings of the elevation, considering zero as the Mean Sea Level (MSL) [30]. A harmonic profile of the surface elevation corresponds to a regular wave. It is represented by equation 44 and depicted in Figure 17, considering fixed time and fixed x position. Regular waves are normally generated by a wavemaker under controlled laboratory conditions.

$$\zeta(x, t) = \zeta_a \cos(kx - \omega t) \quad (44)$$

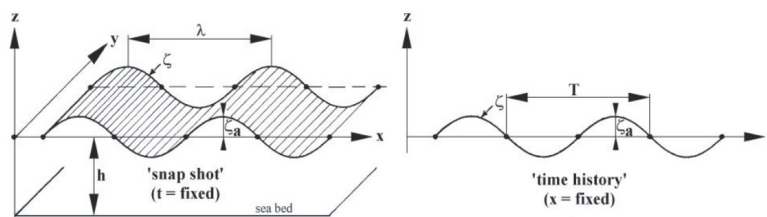


Figure 17: Regular wave definitions [27]

A random and therefore more realistic profile of the surface elevation corresponds to an irregular wave. This is portrayed in Figure 18.

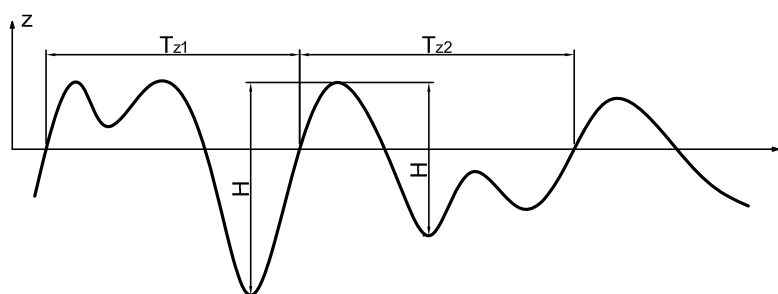


Figure 18: Irregular wave definitions

The symbols included in both figures are described in the Symbols list.

The ocean waves are measured to obtain a wave record. The wave heights and periods in the record are averaged to characterize the waves. An important average, commonly used because it bears resemblance to the visually

estimated wave height, is the significant wave height (H_s). It is defined as the mean of the highest one-third of waves in the wave record [30]:

$$H_s = \frac{1}{N/3} \sum_{j=1}^{N/3} H_j \quad (45)$$

where j is the rank number of the wave, based on the wave height. The significant wave height can also be estimated from the wave spectrum. In this case it is named H_{m0} and it is discussed later in this section.

Another important average quantity is the mean zero-crossing wave period (T_z). It is defined as follows:

$$T_z = \frac{1}{N} \sum_{i=1}^N T_{z_i} \quad (46)$$

Wave dispersion, phase velocity, group velocity and wave energy

These concepts are derived from the linear theory for surface gravity waves, in which the water is considered to be an ideal fluid (incompressible and inviscid) with only the gravity inducing the forces that control the motion of the water particles and the wave amplitudes are small relative to the wave length [30]. The continuity and momentum balances, together with several boundary conditions at the sea surface and sea bottom, establish the flow problem to be solved. Then, under the ideal conditions mentioned above, the flow can be defined by a scalar velocity potential function $\phi(x, y, z, t)$ because its spatial derivatives are equal to the flow velocities:

$$u_x = \frac{\partial \phi}{\partial x}, \quad u_y = \frac{\partial \phi}{\partial y}, \quad u_z = \frac{\partial \phi}{\partial z} \quad (47)$$

For deep water conditions, the velocity potential is given by the following expression:

$$\phi_w(x, y, z, t) = \frac{\zeta_a g}{\omega} e^{kz} \sin(kx - \omega t) \quad (48)$$

The deep water dispersion relation is obtained by combining equations 44, 48 and the dynamic surface boundary condition (further details on this boundary condition in references [27] or [30]):

$$\omega^2 = kg \quad (49)$$

From this equation, the phase velocity is readily derived, considering that the velocity of the propagating harmonic wave is given by:

$$c_w = \frac{\lambda}{T} = \frac{\omega}{k} \quad (50)$$

Then,

$$c_w = \frac{g}{\omega} \quad (51)$$

This expression shows that low frequency or long waves travel faster than high frequency or short waves. Due to this velocity dependence on the frequency, gravity waves are dispersive waves [30].

The group velocity (c_g) results from integrating the power per meter wave front along the total depth (h). This is also known as the wave power level. The derivation can be found in reference [27]. Here the result for deep water waves is presented:

$$c_g = \frac{1}{2}c_w = \frac{gT}{4\pi} \quad (52)$$

where, the definition for phase velocity 51 and $T = 2\pi/\omega$ have been used.

Wave spectrum

The most important form in which waves are described is the wave spectrum. To define the wave spectrum it is necessary to first consider a wave record. That is, the surface elevation $\zeta(t)$ at one location as a function of time, with a certain duration t_d , obtained for example by a buoy at sea. [30].

It is possible to exactly reproduce that record as the sum of a large number of harmonic waves components, as it is shown by equation 53.

$$\zeta(t) = \sum_{i=1}^N \zeta_{\alpha_i} \cos(2\pi f_i t + \alpha_i) \quad (53)$$

where,

ζ_{α_i} = Amplitude of the i -th component

α_i = Phase of the i -th component

f_i = i/t_d . Frequency of the i -th component. The frequency interval is then $\Delta f = 1/t_d$

Determining the amplitudes and phase for each frequency means to obtain the amplitude and phase spectrum for the record. Since the phases have any value between 0 and 2π without any preference for any value, they are ignored. Then, only the amplitude of the spectrum remains to characterize the record. To remove the dependency of the spectrum on the the measure-

ment or experiment, the idea is to repeat the measurement many times (M) and find the average amplitude spectrum [30]:

$$\bar{\zeta}_{a_i} = \frac{1}{M} \sum_{m=1}^M \zeta_{a_i,m} \quad (54)$$

where,

$\zeta_{a_i,m}$ = Amplitude of the i -th component in the m experiment

Now, it is more meaningful to distribute the *variance* of each wave component $\frac{1}{2}\overline{\zeta_{a_i}^2}$, instead of the amplitude. Nevertheless, the variance spectrum only includes the frequencies $f_i = i/t_d$, while all frequencies are present at sea. To resolve this, the variance is distributed only over the frequency interval $\Delta f = 1/t_d$, obtaining a variance density $\frac{1}{2}\overline{\zeta_{a_i}^2}/\Delta f$. Finally, to smooth the discontinuity between frequencies, the interval Δf is let to be infinitesimally small. This originates the variance density spectrum, also known as the wave spectrum ($S_\zeta(\omega)$) [30]:

$$S_\zeta(\omega) \cdot d\omega = \frac{1}{2}\overline{\zeta_a^2}(\omega) \quad (55)$$

All the statistical characteristics of the random sea-surface elevation are determined by the wave spectrum. These characteristics are expressed in terms of the moments of that spectrum, defined as [30]:

$$m_n = \int_0^\infty \omega^n S_\zeta(\omega) d\omega \quad \text{for } n = \dots, -3, -2, -1, 0, 1, 2, 3, \dots \quad (56)$$

The moment m_n is called the n th-order moment of $S_\zeta(\omega)$. Based on this moments several statistical characteristics are defined here below [30]:

$$\text{Variance} = \sigma^2 = m_0 \quad (57)$$

$$\text{Std. deviation} = \sigma = \sqrt{m_0} \quad (58)$$

$$\text{Significant wave height} = H_{m_0} = 4\sqrt{m_0} \quad (59)$$

$$\text{Mean wave period} = \bar{T} = T_{m_01} = \frac{m_0}{m_1} \quad (60)$$

$$\text{Zero-crossing period} = \bar{T}_0 = T_z = T_{m_02} = \sqrt{\frac{m_0}{m_2}} \quad (61)$$

$$\text{Energy period} = T_e = 2\pi \frac{m_{-1}}{m_0} \quad (62)$$

This energy period definition is taken from reference [31] and it is used in section 5.9 to estimate the energy content of irregular waves.

JONSWAP spectrum

At the end of the 1960s an oceanic wave measurement program, known as the JOint North Sea WAve Project (JONSWAP) was developed along a line extending over 100 miles into the North Sea. Analysis of the obtained data produced the following spectral formulation for fetch-limited (or coastal) wind generated seas [27]:

$$S_{\zeta}(\omega) = \frac{320 \cdot H_s^2}{T_p^4} \cdot \omega^{-5} \cdot \exp\left(\frac{-1950}{T_p^4} \cdot \omega^{-4}\right) \cdot \gamma^A \quad (63)$$

where,

$$\gamma = \text{Peakedness factor} = 3.3$$

$$A = \exp\left[-\left(\frac{\frac{\omega}{\omega_p} - 1}{\sigma\sqrt{2}}\right)^2\right]$$

$$T_p = \text{Peak period of the spectrum}$$

$$\omega_p = 2\pi/T_p$$

$$\sigma = \text{a step function of } \omega:$$

$$\text{if } \omega < \omega_p \text{ then: } \sigma = 0.07$$

$$\text{if } \omega > \omega_p \text{ then: } \sigma = 0.09$$

For JONSWAP, the relations between the different period definitions are as follows [27]:

$$T_p = 1.199 \cdot T_{m_{01}} = 1.287 \cdot T_{m_{02}} \quad (64)$$

In JONSWAP observations, the fetch, or the distance to the upwind coast-lines, was limited. Therefore, no transition of the spectrum to the fully developed sea state was observed. However, the JONSWAP spectrum has been shown to be rather universal, applying not only for fetch-limited conditions, but also for arbitrary wind conditions in deep water, including storms and hurricanes [30].

4.2 AVAILABLE POWER IN WAVES

The total energy carried by the waves, per unit horizontal area and averaged over one period, is the sum of the potential energy density and kinetic energy density [30]:

$$\overline{E}_T = \overline{E}_p + \overline{E}_k = \frac{1}{2} \rho g \zeta_a^2 \quad (65)$$

For the derivation of the potential and kinetic energy densities the reader is referred to reference [30].

Then, the wave power level or energy transport, that is actually a net result because more energy is transported in the wave propagation direction than against the propagation, is defined by:

$$J = \overline{E_T} c_g \quad (66)$$

where, c_g is the group velocity or the transport velocity of the energy, and it is given by equation 52. Since $\overline{E_T}$ is an energy density, J has units of power per meter wave front.

Using equations 65 and 52 the expression for the wave power level of a harmonic wave is obtained:

$$J = \frac{\rho g^2}{32\pi} \cdot T \cdot H \quad (67)$$

If irregular waves are considered, the definition of the wave spectrum 55 can be combined with equation 65 to obtain:

$$\overline{E_T} = \rho g \int_0^\infty S_\zeta(\omega) d\omega = \frac{\rho g}{16} H_s^2 \quad (68)$$

where, the definitions 59 and 56 have been applied.

For irregular waves, the wave power level can be expressed as follows [31]:

$$J = \rho g \int_0^\infty S_\zeta(\omega) \cdot c_g(\omega) d\omega = \frac{\rho g^2}{2} \int_0^\infty \frac{S_\zeta(\omega)}{\omega} d\omega \quad (69)$$

where, the group velocity definition (52) has been used.

Now, realizing that in this equation, the integral is the -1 moment of the spectrum, the energy period definition (64) can be incorporated, as follows:

$$J = \frac{\rho g^2}{4\pi} \cdot T_e \cdot m_0 = \frac{\rho g^2}{64\pi} \cdot T_e \cdot H_s^2 \quad (70)$$

where, the equation 59 has been substituted as well.

This obtained wave power level in irregular waves is an estimation used in engineering calculations, specially for the evaluation of WEC concepts (Refer to [31]). The analytical derivation of the wave power level in irregular waves implies a summation over the harmonic waves components

4.3 WAVE POWER ABSORPTION

Absorption principle

Wave energy absorption should be understood as a wave interference phenomenon. In order to absorb energy from a wave, the WEC must generate a *counter-wave* to interfere with the incident wave. If the interference reduces at least a part of the incoming wave, wave energy is absorbed by the WEC [31]. This may sound counter-intuitive, but it is illustrated in Figure 19 considering a heaving WEC.

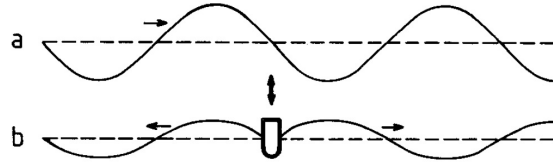


Figure 19: Power absorption by a planar version of a heaving PA

In this Figure the drawing *a* shows the undisturbed wave. The drawing *b* shows the heaving WEC generating waves in the upstream and downstream directions. The downstream waves only dissipate energy from the system. Therefore, this planar version of a heaving WEC can absorb maximum 50% of the incoming wave.

Power absorption by single DOF system

First, let us consider a 3D version of the planar case of Figure 19. Second, let us consider a spherical PA connected to a PTO system with a mechanical spring coefficient equal to zero and with a mechanical damping coefficient equal to b_{PTO} . These are actually the conditions considered in the present research effort.

Then, taking the equation of motion (EoM) for a PA that has been presented in section 3.3, the PTO damping can be added to the hydrodynamic damping coefficient and both sides to the equation can be multiplied by the heave velocity as defined by equation 8. This produces the following relation:

$$(-\omega^2(m + a) + i\omega(b + b_{PTO}) + c) \cdot z \cdot (i\omega z) = F_w \cdot (i\omega z) \quad (71)$$

The real part of the right hand side of equation 71 is the power applied to the mechanical system by the wave-excitation forces. The left hand side of the equation can be redefined as follows

$$(m + a) \frac{d}{dt} \left(\frac{1}{2} \dot{z}^2 \right) + (b + b_{PTO}) \dot{z}^2 + c \frac{d}{dt} \left(\frac{1}{2} z^2 \right) = P_w \quad (72)$$

The coefficients multiplying the derivatives can be included in the derivatives to obtain:

$$\frac{d}{dt} \left(\frac{1}{2} (m + a) \dot{z}^2 \right) + (b + b_{PTO}) \dot{z}^2 + \frac{d}{dt} \left(\frac{1}{2} c z^2 \right) = P_w \quad (73)$$

Now, it can be seen that the first term in the left hand side is the power stored and dissipated as kinetic energy in the mass, the third term is the power stored and dissipated as potential energy in the hydrostatic restoring. The second term is the power dissipated as radiated waves and the power absorbed by the PTO system. It is deduced then that the power of the first and third terms can not be effectively used and it is therefore known as *reactive power*, and the power of the second term that can be effectively used is known as *active power*. In an equation form:

$$\left(\frac{d}{dt} (E_k + E_p) \right)_{\text{reactive}} + ((b + b_{PTO}) \dot{z}^2)_{\text{active}} = P_w \quad (74)$$

The active power that is actually absorbed by the WEC can be expressed in the following way, using the real form of the heave velocity, obtained by taking the derivative of equation 2:

$$P_{PTO} = b_{PTO} z_a^2 \omega^2 \sin^2(\omega t + \epsilon_{z,\zeta}) \quad (75)$$

Now, the interest is on the average over one period of oscillation:

$$\bar{P}_{PTO} = \frac{1}{2} b_{PTO} z_a^2 \omega^2 \quad (76)$$

where, z_a has been defined in section 3.3, specifically with equation 19. Substituting equation 19 into equation 76 the absorbed power over one period in regular waves is obtained:

$$\bar{P}_{PTO} = \frac{1}{2} b_{PTO} \zeta_a^2 RAO^2 \omega^2 \quad (77)$$

The RAO^2 can be expanded using the relation 18, adding the b_{PTO} and considering that the squared module of a complex number can be calculated in the following way:

$$|\widetilde{z}_a|^2 = \widetilde{z}_a \cdot \widetilde{z}_a \quad (78)$$

where, \widetilde{z}_a is the complex conjugate of \widetilde{z}_a . Resolving this expression results in the following relation:

$$RAO^2 = \frac{F_{wa}^2}{(c - \omega^2(m + a))^2 + ((b + b_{PTO})\omega)^2} \quad (79)$$

Substituting this into equation 77 produces a relation for the average absorbed power that only depends on the regular wave characteristics, the hydrodynamic coefficients, the wave-excitation force, the restoring coefficient and the mechanical PTO damping:

$$\bar{P}_{\text{PTO}} = \frac{1}{2} b_{\text{PTO}} \zeta_a^2 \omega^2 \frac{F_{wa}^2}{(c - \omega^2(m + a))^2 + ((b + b_{\text{PTO}})\omega)^2} \quad (80)$$

Considering now irregular waves, the wave spectrum definition can be used to obtain the power absorbed in an infinitesimal frequency band in the spectrum:

$$\bar{P}_{\text{PTO}_{d\omega}} = b_{\text{PTO}} \text{RAO}^2 \omega^2 S_\zeta(\omega) d(\omega) \quad (81)$$

Then, integrating over the whole frequency range of the spectrum, the total absorbed power over one period in irregular waves is obtained:

$$\bar{P}_{\text{PTO}} = b_{\text{PTO}} \int_0^\infty \text{RAO}^2 \omega^2 S_\zeta(\omega) d(\omega) = b_{\text{PTO}} \int_0^\infty \omega^2 S_z(\omega) d(\omega) \quad (82)$$

where, the RAO is kept inside the integral because it depends on the wave frequency. In this expression the definition of the heave motion spectrum has been used and it is given by $S_z(\omega) d\omega = \frac{1}{2} z_a^2$.

Optimized power absorption by single DOF system

In reference ??, based on equation 80, it is mentioned that there are two conditions for maximum power extraction. The first condition is a WEC in resonance. The resonance condition occurs when the restoring forces equal the inertia forces; in an equation form:

$$c - \omega^2(m + a) = 0 \quad (83)$$

This is logical because the term $(c - \omega^2(m + a))^2$ is in the denominator of equation 80 and it is always positive. Therefore, let it approach to zero maximizes the absorbed power. A WEC in resonance also means that the wave frequency is equal to the WEC's natural frequency defined in equation 21. In practice, this is possible to achieve in regular waves, but more difficult in irregular waves, because it would mean to continuously tune the WEC natural frequency to the peak frequency of the spectrum that varies from one sea state to the other. In the present study that inconvenience is solved by tuning the WEC's natural frequency to the peak frequency of the most common sea state within the operational subset.

The second condition mentioned in reference ?? is a PTO damping equal to the hydrodynamic damping. The demonstration of this condition requires

more calculations than the previous condition and it is presented here below.

The demonstration starts with the average power absorption in resonance condition. That is:

$$\bar{P}_{PTO} = \frac{1}{2} b_{PTO} \zeta_a^2 \frac{F_{wa}^2}{(b + b_{PTO})^2} \quad (84)$$

Now, to determine the $b_{PTO,opt}$ the partial derivative of the absorbed power with respect to b_{PTO} is taken and it is made equal to zero:

$$\frac{\partial \bar{P}_{PTO}}{\partial b_{PTO}} = \frac{\zeta_a^2 F_{wa}^2 \left(\frac{1}{2}(b + b_{PTO}) - b_{PTO} \right)}{(b + b_{PTO})^3} = 0 \quad (85)$$

From this expression it is deduced that:

$$b_{PTO,opt} = b \quad (86)$$

Of course, this result is only valid in resonance. A more generalized expression for any frequency is obtained by taking the partial derivative of equation 80 with respect to b_{PTO} :

$$b_{PTO,opt} = \sqrt{\left(\frac{c}{\omega} - (m + a)\omega \right)^2 + b^2} \quad (87)$$

If the hydrodynamic and restoring coefficients are considered constant, it can be seen that any $\omega < \omega_n$ or $\omega > \omega_n$ generates a positive first term within the root, which is added to b^2 to always produce a $b_{PTO,opt} > b$. Therefore, the $b_{PTO,opt}$ at resonance is the minimum value, in comparison with the value obtained for other frequencies.

In irregular waves it is not possible to obtain a generalized expression for the optimum b_{PTO} because the power absorbed is a summation from 1 until n of the power absorbed from each wave harmonic component and the motion amplitudes themselves depend on the b_{PTO} .

In the present study this problem is solved with a constant b_{PTO} per sea state in the operational subset. That constant b_{PTO} results from an optimization process over a b_{PTO} range of values. Please refer to section 5.10.1 for the details.

Budal diagram

As explained by Falnes in reference [32] there exist two upper limits for the power that can be absorbed from a regular wave: the P_A and P_B limits. The former is just a consequence of an optimum PTO control or, in other words, optimum energy absorption. Optimum control implies the following two conditions:

1. The velocity of the PA is in phase with the dynamic pressure of the incoming wave [31].
2. The heave amplitude of the PA in resonance condition needs to be adjusted so that the amplitude of the incident wave is twice the amplitude of the radiated wave generated by the PA [31].

Considering there is axial symmetry for the heaving semi-submerged body, P_A is defined by equation 88 [32].

$$P_A = c_\infty T^3 H^2 \quad (88)$$

where,

$$c_\infty = \frac{\rho g^3}{128\pi^3} \quad (89)$$

The other limit, P_B , also known as Budal's upper bound, corresponds to an efficient exploitation of the PA's swept volume V , and not of the wave energy available in the sea, as it is the case with P_A . The swept volume is defined as the difference between maximum and minimum displacement of the heaving PA. Budal's original derivation leads to the following relation presented by Falnes [32].

$$P_B = c_0 \frac{VH}{T} \quad (90)$$

where,

$$c_0 = \frac{\rho g \pi}{4} \quad (91)$$

A P Vs T "Budal diagram" can be constructed (see Figure 20), including the two limits previously explained, and three power absorbed curves; all of them with optimum motion amplitude (optimum b_{PTO}). For the lowest curve there is no phase control and therefore it is called *passive loading control*, whereas for the other two curves phase control by the latching method and by the reactive method, respectively, has been assumed. An immersed axisymmetric PA of volume V (maximum swept volume) with the following conditions: $H = 2.26\text{m}$, $V = 524\text{m}^3$, $2r = 10\text{m}$, where r is the sphere radius. The heave amplitude of the sphere is load-constrained not to exceed 3m [32].

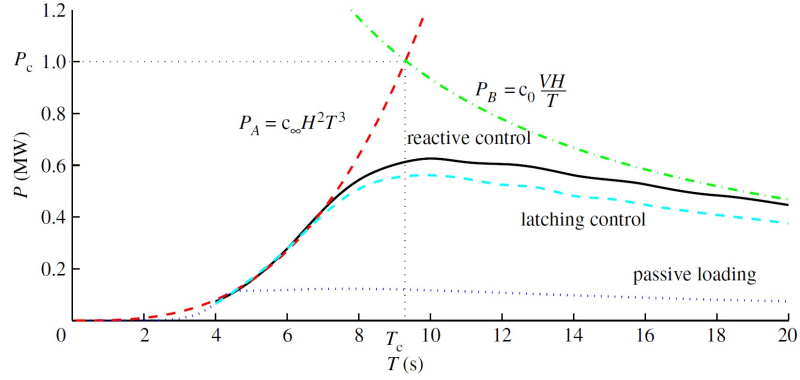


Figure 20: Budal diagram

This diagram is used to verify the power absorption results in section 6.2.3.

FOHWWEC power absorption

The motions of the WECs on the FOHWWEC are restricted with the exception of heave. That means there is relative heave motion between the substructure and the WECs.

In order to use all the power absorption relations presented in this section, the heave motion z has to be just substituted by the relative heave motion z_r .

From now onwards, when the relative condition of the motion needs to be highlighted, the subscript r is used.

4.4 ABSORPTION WIDTH

The absorption width (λ_p) is defined by De Backer in reference [33] as follows:

$$\lambda_p = \frac{P_{abs}}{P_{avail}} = \frac{\bar{P}_{PTO}}{J} \quad (92)$$

It is normally presented in meters and it is an indicator of the amount of wave front that it is actually absorbed by the WEC. When divided by the total active length of the WEC an efficiency is obtained. Since in the present study only one type of WEC is considered and it has a combined length of 20m (considering two spherical PAs) the actual efficiency is already represented by the absorption width.

Absorption width for point absorber

For a PA the absorption efficiency can be even larger than 100%. This phenomenon is called the *point-absorber effect* or *antenna effect*. It is explained by

the fact that the PA is able to absorb a larger fraction of the power than what is available over its diameter. In terms of the absorption width, in a regular wave with wave length λ , the maximum absorption width of a heaving point absorber is theoretically equal to the following:

$$\lambda_{p,max} = \frac{\lambda}{2\pi} \quad (93)$$

This result has been independently derived by some researchers; among them, Evans [34].

4.5 ANNUAL ENERGY ABSORPTION

The WECs are normally evaluated and compared to each other based on their Annual Electricity Production (AEP). This quantity is typically given in Megawatts-hour per year (MWh/y).

Although in the present research the comparison between the FOHWWECs is not based on this quantity, it is useful to report a variable that is similar to the AEP: the annual energy absorption. This variable does not consider the PTO energy losses, but it provides a reference on which evaluate and compare the FOHWWECs with other WECs. In order to obtain the annual energy absorption, the absorbed power (\bar{P}_{PTO}) in a given sea state is multiplied by the amount of hours per year of that sea state, obtaining the absorbed energy (\bar{E}_{PTO}) of the given sea state in a year, as stated in equation 94.

$$\bar{E}_{PTO} = \bar{P}_{PTO} \cdot 8760 \cdot \frac{N_s}{N_{s_t}} \quad (94)$$

where,

8760 = Amount of hours in a year

N_s = Sea state yearly-occurrences

N_{s_t} = Sum of all sea state yearly-occurrences in the operational subset

These values are included in the absorbed energy matrices for each simulation. The annual energy absorption is obtained by adding the values in the energy matrix.

METHODOLOGY DESCRIPTION

5.1 DEFINITION OF THE WEC UNIT

5.1.1 Geometry

As mentioned in the scope definition (Section 1.0.2), the WEC is a semi-submerged spherical point absorber. It has a radius of 5m and a draft of 5m, as it is shown in Figure 21.

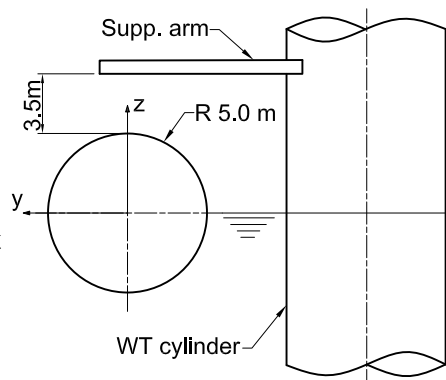
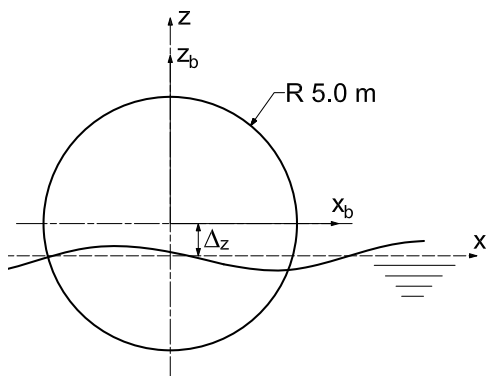


Figure 21: WEC unit: Spherical PA Figure 22: WEC unit and WT cylinder

The WEC sizing has been performed based on three requirements:

1. The internal space of the sphere is reserved for water ballast.
2. The wet natural frequency of the WEC must be as close as possible to the most common sea state peak frequency, which, for the selected wave data, corresponds to $\omega = 0.89\text{rad/s}$.
3. The added ballast should be enough to tune the WEC's natural frequency to the most common sea state peak frequency. In this way, the optimum resonance condition for power absorption, derived from equation 80, is at least obtained for the most common sea state.

This lead to an iterative process until a radius of 5m was reached. This size provides the following WEC parameters:

Parameter	Value
Unballasted displacement [tons]	268.34
Plate thickness [cm]	10.3
Ballast mass [tons]	500
Wet natural frequency [rad/s]	0.9

Table 1: WEC unit parameters

To maintain the WEC's draft at 5m even with ballast, a constant force spring could be added to the WEC-substructure connection. It should supply just the necessary force to carry the ballast weight.

5.1.2 PTO system

To simplify the calculations and the PTO setup, it is decided to use a zero PTO spring coefficient for all simulations. In consequence, the PTO system consists only on a linear damper with damping coefficient b_{PTO} . This damping value is optimized for each sea state, according to the procedure described in section 5.10.1. This control strategy, based only on the adjustment of the PTO damping coefficient is known as passive loading control [31]. As it can be seen in Budal diagram (Figure 20), passive control provides sub-optimal power absorption, in comparison with phase controlling strategies (latching and reactive control).

One side of the linear damper is attached to the top of the sphere, the other side to a supporting arm. This arm extends from the cylinder substructure. There is an initial distance $h_{arm} = 3.5\text{m}$ from the sphere's top until the bottom of the arm to allow for relative motion (see Figure 22). Nevertheless, since no displacement limitations (end-stops) to the WEC heave motion are considered, it is assumed that any relative heave motion amplitude is allowed.

5.2 DEFINITION OF THE DESIGN CONFIGURATIONS

As established in the scope definition (section 1.0.2) three DCs are considered, each with two spherical PAs, differing from each other in the substructure's floating stability principle. In this section, a couple of additional design requirements are established. The resulting geometries are also described.

5.2.1 Additional design requirements

1. The substructure must be as simple as possible. Additional material is added when it is strictly necessary.

2. Whenever possible, the substructure's volume should be the same for all DCs. This adds validity to the performance comparisons.
3. There is symmetry at least with respect to one of the horizontal plane substructure axes. The reason behind this requirement is only stability.
4. Cylinders are the substructure construction blocks. They are simple and common in offshore structures. Even proven FOWTs, such as Hy-Wind and WindFloat, use them.
5. There is one WT mounted on the so-called *WT cylinder*. The WECs are also attached to the WT cylinder. The rest of the cylinders are used for ballast and therefore called *B cylinders*.
6. To simplify the study, all cylinders have the same diameter as the WT cylinder.
7. Three draft levels (D_1 , D_2 and D_3) with 10m between each other are considered for each design configuration. This is done to be able to accomplish the secondary objective.

5.2.2 Geometry

The figures 23, 24 and 25 depicts the substructure and WECs of each DC. The tables 2, 3 and 4 present the most relevant parameters of each DC. Both, figures and tables, describe the geometry of the design configurations.

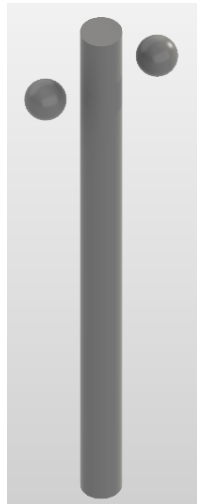


Figure 23: DC1 substructure and WECs

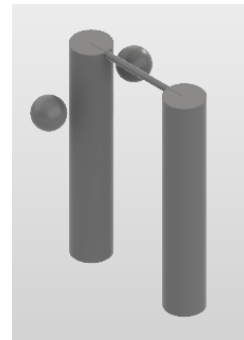


Figure 24: DC2 substructure and WECs

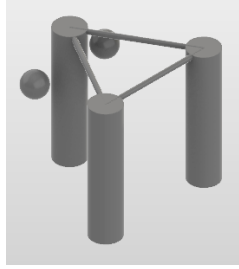


Figure 25: DC3 substructure and WECs

Parameter	Value
D levels [m]	118, 128, 138
r_{cyl} [m]	5
$l_{cyl-WEC}$ [m]	5

Table 2: DC1 FOHWWECs parameters

Parameter	Value
D levels [m]	53, 63, 73
r_{cyl} [m]	6
$l_{cyl-WEC}$ [m]	5
$l_{cyl-cyl}$ [m]	35

Table 3: DC2 FOHWWECs parameters

Parameter	Value
D levels [m]	22, 32, 42
r_{cyl} [m]	6
$l_{cyl-WEC}$ [m]	5
$l_{cyl-cyl}$ [m]	45

Table 4: DC3 FOHWWECs parameters

5.2.3 Naming conventions

In the present thesis the design configurations are named as DC₁, DC₂ and DC₃. Since each of them has three draft levels, the suffixes -D₁, -D₂ and -D₃ are added when required. That produces the following FOHWWEC names:

FOHWWEC DC ₁ -D ₁	FOHWWEC DC ₂ -D ₁	FOHWWEC DC ₃ -D ₁
FOHWWEC DC ₁ -D ₂	FOHWWEC DC ₂ -D ₂	FOHWWEC DC ₃ -D ₂
FOHWWEC DC ₁ -D ₃	FOHWWEC DC ₂ -D ₃	FOHWWEC DC ₃ -D ₃

Table 5: FOHWWEC names

The word "FOHWWEC" can be substituted by "FOWT" to refer to the device without WECs.

5.3 DEFINITION OF THE SIMULATIONS

The word “simulation” is used to represent a run of the *FOHWWEC Analysis Program*. In this run, the motions and performance variables are estimated for either one of the following four:

1. Isolated WECs
2. All three draft levels of DC₁
3. All three draft levels of DC₂
4. All three draft levels of DC₃

The expression isolated WECs means two WECs that are neither interacting with each other nor interacting with a substructure. For simplicity, the WECs are not moored and they are allowed only to heave.

Each simulation is done with a parked WT and in 0 degree waves. The parked WT is an operational condition that is required because no wind loads are included in the calculations. The 0 degree waves are translating in the direction of the x axis ($\mu = 0^\circ$) and they establish a symmetric wave loading condition.

5.4 HYDROSTATIC STABILITY CALCULATION

The first stability condition is that FOHWWECs and FOWTs must be neutrally buoyant. This is the vertical stability condition.

The second stability condition is that FOHWWECs and FOWTs must have intercept angles below the 10° . This is the transversal/longitudinal stability condition. The intercept angle refers to the angle at which the righting moment is equal to the heeling/pitching moment. The specific value of 10° has been obtained from reference [16], where a FOHWWEC concept is studied.

DC₁ FOHWWECs use a center of gravity (CoG) position below the center of buoyancy (CoB) in order to obtain transversal and longitudinal stability. DC₃ FOHWWECs use instead the expanded WPA. DC₂ FOHWWECs use both, the CoG position for transversal stability, and the expanded WPA for the longitudinal stability.

The stability calculation developed in the *FOHWWEC Analysis Program* employs a number of inputs that triggers an iterative process. This process considers two cases: the case of the FOWT and the case of the FOHWWEC with parked WECs. The result from the iteration is normally the substructure cylinder radius, but it can also be the draft, or both. It depends on the DC being analyzed. In tables 6, 7, 8 and 9, the inputs and outputs are presented. DC₂ and DC₃ FOWT data can be found in Appendix A.

Property	Value	I/O
f [m]	15	I
WT prop. [-]	In Appendix B	I
$\rho_{s(eq)}$ [Kg/m ³]	8500	I
d_{rat} [-]	1.33	I
r_{cyl}^{max} [m]	6	I
φ_{max} [°]	10	I
θ_{max} [°]	10	I

Table 6: DC1 common stability input

Property	Value	I/O
D [m]	118	I
r_{cyl} [m]	5	O
∇_b [tons]	9499.39	O
m_b [tons]	5879.98	O
CoB _z [m]	-59.0	O
CoG _z [m]	-78.43	O
GM _t [m]	19.48	O
GM _l [m]	19.48	O
I _{yy} [Kg.m ²]	3.23380e+10	O

Table 7: FOWT DC1-D1 stability I/O

Property	Value	I/O
D [m]	128	I
r_{cyl} [m]	5	O
∇_b [tons]	10304.42	O
m_b [tons]	6473.09	O
CoB _z [m]	-64.0	O
CoG _z [m]	-87.05	O
GM _t [m]	23.10	O
GM _l [m]	23.10	O
I _{yy} [Kg.m ²]	3.70831e+10	O

Table 8: FOWT DC1-D2 stability I/O

Property	Value	I/O
D [m]	138	I
r_{cyl} [m]	5	O
∇_b [tons]	11109.45	O
m_b [tons]	7066.20	O
CoB _z [m]	-69.0	O
CoG _z [m]	-95.60	O
GM _t [m]	26.64	O
GM _l [m]	26.64	O
I _{yy} [Kg.m ²]	4.23252e+10	O

Table 9: FOWT DC1-D3 stability I/O

Some additional notes on these tables: The WT properties are an important input for stability calculation. They are included in Appendix B. The equivalent steel density ($\rho_{s(eq)}$) is used to account for painting, bolting, welds and

flanges. This same approach has been used in reference [35]. From the ratio d_{rat} an initial cylinder radius of 4m is obtained. The z coordinates are given with respect to the MSL.

As a final result, the stability calculation module produces three plots. They present the righting moment Vs the heel/trim angle, including as well the corresponding heeling/trimming moment. These plots are in figures 26, 27 and 28.

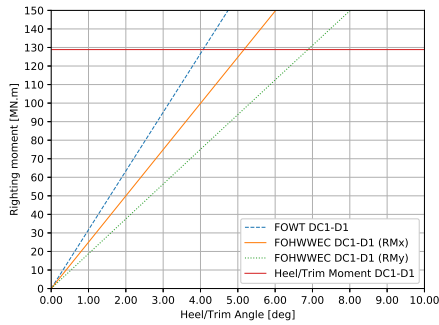


Figure 26: Righting moment curve for DC1-D1

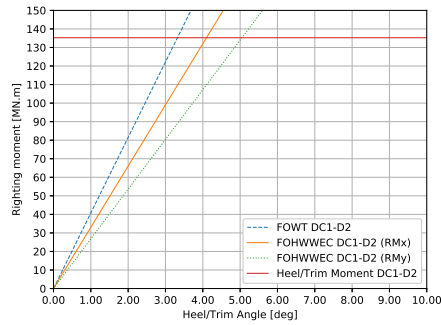


Figure 27: Righting moment curve for DC1-D2

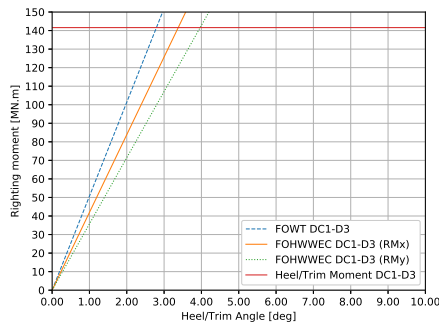


Figure 28: Righting moment curve for DC1-D3

As it can be seen in these plots, all cases are stable since all intercept angles are below 10° . Besides this, the FOHWWECs have a greater intercept angles in comparison with the FOWTs. It has to be remembered that the WECs on the FOHWWECs are in parked condition, that means the weight of partly ballasted WECs is taken by the substructure. That results in lower metacentric heights and it means that for DC1 the FOHWWEC with parked WECs case is more critical than the FOWT case.

The stability results for DC2 and DC3 are included in Appendix A.

5.5 MESH MODELING AND CONVERSION

As described in reference [36], Salome supplies a generic pre- and post-processing platform for numerical simulations. Specifically, it is used in the present research to model the underwater surfaces, to mesh them in quadrangular panels and to export the meshes to DAT files. The exported meshes are then converted to adapt them to NEMOH requirements.

All the actions described above are automatically done with Python-based instructions. The Python modules containing those instructions are part of the *Salome-NEMOH Interface* of the *FOHWWEC Analysis Program*. It is possible to perform at once the modeling, meshing, exporting and conversion of all FOHWWECs and FOWTs within a design configuration.

The length of the panels has been set by indicating the length of the segments in which the edges are split. That corresponds to the Salome meshing option "Local Length". For the spherical WEC, the length is set to 1m and for the substructure cylinders to 1.5m. The length is larger for the cylinder to reduce the time spent in the calculations.

A minimum required length of $\lambda/8$ is a common criterion in ship hydromechanics to obtain a proper convergence of the wave pattern when using panel methods. If the focus are only the forces and not the wave patterns, $\lambda/4$ should be enough (Refer to [37]). Considering that the highest wave frequency involved in the calculations is 2.255rad/s and that the dispersion relation in deep water can be expressed as follows:

$$\omega^2 = \frac{2\pi g}{\lambda} \quad (95)$$

Then,

$$\frac{\lambda}{8} = 1.51 \text{ m} \quad (96)$$

Therefore, both lengths used in the present study are below this minimum requirement, even though the interest of the present research is not the wave pattern, but the forces. Additionally, to verify the used criterion, a mesh sensitivity study is performed in chapter 6.

Figure 29 portrays the meshes of the two WECs and the substructure WT cylinder of DC1.

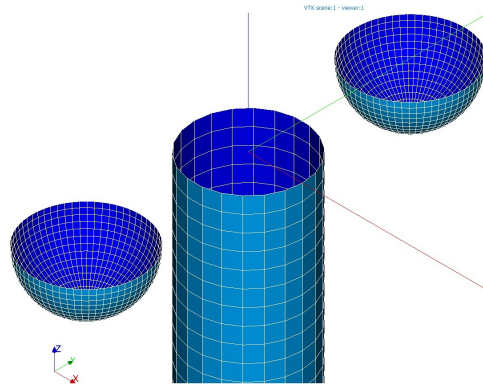


Figure 29: DC1 mesh example

5.6 HYDRODYNAMIC COEFFICIENTS CALCULATION IN NEMOH

As explained in reference [38], NEMOH is an open source Boundary Element Method (BEM) solver. The BEM method, also known as panel method employs Green's functions to transform a flow problem into a problem of source distribution on the body surface. Based on this, the scatter and radiated velocity potentials are solved to determine the wave excitation forces, the added mass and radiation damping terms.

According to reference [39], NEMOH's calculations have been verified for hydrodynamic interactions between two floating bodies. In the portrayed case, two cubes with 6 DOFs interact and the results were compared with the results obtained from BEM code *Aquaplanus*. At first glance, this verification seems enough for the three interacting bodies in the design configurations of the present work. Nevertheless, future research could address a similar verification with three interacting floating bodies.

Besides the geometrical information of the panels, NEMOH requires other inputs that are summarized in Table 10.

Property	Value
Water depth [m]	250
ω_{\min} [rad/s]	0.005
ω_{\max} [rad/s]	2.255
Num. of freq [-]	76
g [m/s^2]	9.81
ρ [Kg/m^3]	1025

Table 10: NEMOH input parameters

NEMOH produces two files that are relevant for the present work; First, the *ExcitationForce.tec* file, that contains the magnitude and phase of the total

wave excitation load (undisturbed wave and diffracted wave). Second, the *RadiationCoefficients.tec* file containing the added mass and damping coefficients for all body-DOF combinations. Example extracts from these files are included in Appendix C.

5.7 MOORING DETAILS AND LOADS

The mooring system applied to all DCs consists of three symmetrically distributed catenary lines. The properties are included in Table 11.

Property	Value
l_{moor} [m]	600
D_{moor} [m]	10
L_0 [m]	750
Chain type [-]	132 mm R4S chain

Table 11: Mooring system properties

The first three properties are defined in the Symbols list. The chain type has been selected from the DAMEN catalog [40].

The mooring calculation module of the *FOHWWEC Analysis Program* receives these properties and starts an iteration process in which the horizontal tension component in the line is varied until the fairlead vertical position is reached. Once this is done, a profile of the catenary line can be plotted (See Figure 30). The line tension and angle at the fairlead can be used to calculate the mooring restoring force matrix.

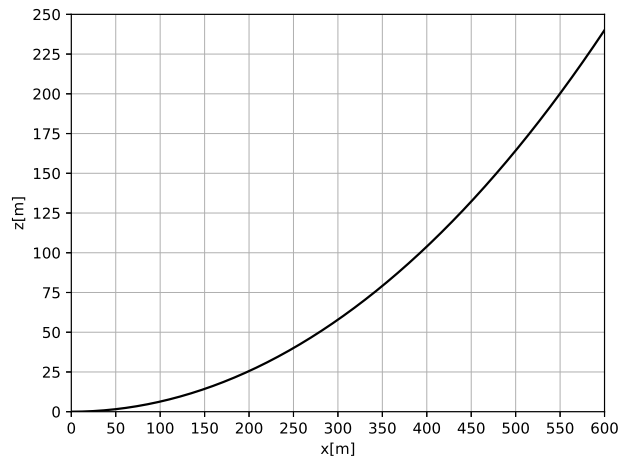


Figure 30: Mooring line catenary profile

The mooring restoring matrix $C_{j k_{\text{moor}}}$ is calculated with the equations constructed by Al-Solihat and Nahon in reference [41] around the FOHWWEC

position in calm waters with parked WT. The obtained full matrix (6 x 6) in SI units is presented here below.

$$C_{jk_{moor}} = \begin{bmatrix} 2.12 \times 10^5 & 0.0 & 0.0 & 0.0 & -1.94 \times 10^6 & 0.0 \\ 0.0 & 2.12 \times 10^5 & 0.0 & 1.94 \times 10^6 & 0.0 & 0.0 \\ 0.0 & 0.0 & 6.83 \times 10^4 & 0.0 & 0.0 & 0.0 \\ 0.0 & 1.94 \times 10^6 & 0.0 & 1.64 \times 10^8 & 0.0 & 0.0 \\ -1.94 \times 10^6 & 0.0 & 0.0 & 0.0 & 1.64 \times 10^8 & 0.0 \\ 0.0 & 0.0 & 0.0 & 0.0 & 0.0 & 6.36 \times 10^7 \end{bmatrix}$$

It is important to mention that although Al-Solihat and Nahon analysis is exact and nonlinear, the fact that the mooring restoring loads are taken around the FOHWWECS position in calm waters with parked WT and not around its equilibrium position during operation, disregards the nonlinear effects created by the displacement between those positions. Future research is to determine the impact of those nonlinear effects on the FOHWWECS performance.

5.8 WAVE DATA AND JONSWAP SPECTRUM

Since the FOHWWECS has been conceived in real scale, to be able to compare its performances, real wave data is necessary. In other words, a sea region has to be selected and its wave scatter diagram is then used to test the FOHWWECS performance in different sea states.

On one hand, the selected sea region should have deep water areas with depths of at least 250m, allowing for proper installation and operation of the FOHWWECS. On the other hand, obtaining wave climate data is not an easy task. In consequence, a compromise had to be found, and to test the FOHWWECS performance the North Sea region scatter diagram is used (See Table 12). Global Wave Statistics (GWS) [42] provides these scatter diagrams for several regions around the world.

H_s/T_z	3.5	4.5	5.5	6.5	7.5	8.5	9.5	10.5	11.5	12.5	13.5
0.5	19	86	94	41	10	2	0	0	0	0	0
1.5	3	49	121	99	40	10	2	0	0	0	0
2.5	1	17	63	73	40	13	3	1	0	0	0
3.5	0	6	27	39	26	10	3	1	0	0	0
4.5	0	2	11	19	14	6	2	1	0	0	0
5.5	0	1	4	9	7	4	1	0	0	0	0
6.5	0	0	2	4	4	2	1	0	0	0	0
7.5	0	0	1	2	2	1	1	0	0	0	0
8.5	0	0	0	1	1	1	0	0	0	0	0
9.5	0	0	0	1	1	0	0	0	0	0	0
10.5	0	0	0	0	0	0	0	0	0	0	0
11.5	0	0	0	0	0	0	0	0	0	0	0
12.5	0	0	0	0	0	0	0	0	0	0	0
13.5	0	0	0	0	0	0	0	0	0	0	0
14.5	0	0	0	0	0	0	0	0	0	0	0

Table 12: Scatter diagram of the North Sea region [42]

From this data an operating subset is selected based on the following logic: In the wave energy sector it is a common strategic choice to design the WEC to operate where the 80% of the sea states are concentrated. The rest are considered as critical sea states, for which storm protection and survivability strategies are important. To determine this subset a sum in rows and columns is done on Table 12. Then row and column with highest values are selected. From those, the sum is expanded until it reaches 80% of the total sea states. This produces the operational subset shown in Table 13.

H_s/T_z	3.5	4.5	5.5	6.5	7.5
0.5	19	86	94	41	10
1.5	3	49	121	99	40
2.5	1	17	63	73	40
3.5	0	6	27	39	26

Table 13: Scatter diagram operational subset of the North Sea region

Once the sea states are established, it is required to assign a wave frequency spectrum to each of them. The wave spectrum, as explained in section 4.1, is one of the building blocks of the FOHWWEC motion spectra and, in consequence, of the FOHWWEC performance.

The JONSWAP spectrum is selected as the standard form definition of the wave spectrum. It describes the North Sea and that matches the scatter

diagram selection. As mentioned in section 4.1, this formulation is for fetch-limited (or coastal) wind generated seas. Nevertheless, it has proven to be rather universal, applying also for arbitrary wind conditions in deep water, including storms and hurricanes [30]. This versatility has expanded its usage to different wave-related studies, including wave energy absorption, but the author did not find a demonstration on JONSWAP spectrum validity for WEC studies. It may be that its peakedness, in comparison with other spectra, produces non-conservative results for power absorption. This is still to be determined or the study addressing it has to be found.

Despite the previous analysis, the objective of the present work is to compare performances, not to optimize the performance to a certain region. Therefore, the impact of the spectral formulation is not a critical issue.

As an example, the JONSWAP wave spectra for sea states in the operational subset with $H_s = 1.5\text{m}$ are depicted in Figure 31.

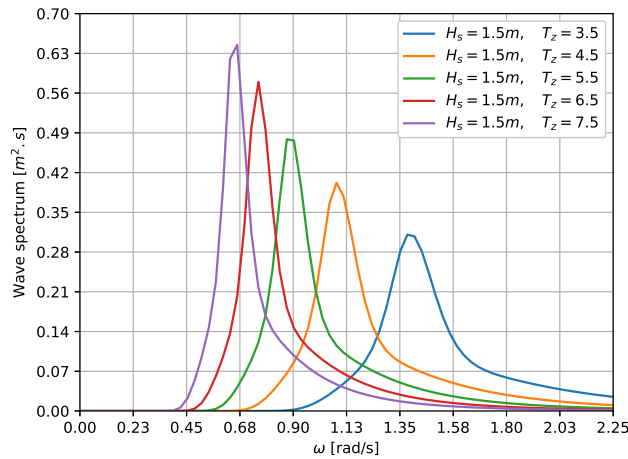


Figure 31: JONSWAP spectra in operational subset for $H_s = 1.5\text{m}$

5.9 AVAILABLE POWER CALCULATION

The available power per meter wave front in an irregular sea state is calculated with equation 70. The results per meter wave front for the operational subset, are depicted in Table 14. Notice that in this table the zero crossing periods has been substituted by the peak periods. This is to have uniformity between this matrix and the performance matrices included in chapter 7.

H_s/T_p	4.5	5.8	7.1	8.4	9.7
0.5	0.5	0.6	0.8	0.9	1.1
1.5	4.2	5.7	7.0	8.3	9.6
2.5	11.7	15.8	19.5	23.1	26.7
3.5	0.0	30.9	38.2	45.3	52.4

Table 14: Available power per meter wave front [kW/m]

There are some aspects to highlight in this table. First, the maximum power available per meter wave front is obtained for sea state $H_s = 3.5$, $T_p = 9.7$ s. This is logical because the power content increases with the increase of both, the period and the significant wave height.

5.10 MOTION AND PERFORMANCE CALCULATION

This is the last step of the methodology and it corresponds as well to the main module of the *FOHWWEC Analysis Program*. Four objectives are pursued in this step:

1. To calculate an optimum b_{PTO} for each sea state in the operational subset. This process is described in section 5.10.1.
2. To solve the motion equations for the three floating bodies loaded with 0 deg waves, using the optimum b_{PTO} just calculated. In this condition there is symmetry in the geometry and in the wave load. In consequence, the motion can be described with four DOFs: the surge, heave and pitch of the substructure and the heave of the WEC. The coupled multi-body equation 34 is solved to obtain the RAOs. It is important to highlight that in this equation all the matrices of hydrodynamic coefficients (diagonal and off-diagonal) are considered. Therefore, all the radiation/diffraction interaction between the bodies is included.
3. To calculate the natural frequencies associated to each DOF. In this case, the eigenvalue problem (similar to equation 33) is solved, obtaining the natural frequencies reported in sections 7.2.1.1, 7.3.1.1 and 7.4.1.1.
4. To calculate the performance variables. For a detailed explanation of the calculation, the reader is referred to section 5.10.2. Then, the values obtained for these variables are portrayed in a *performance plot*, with the annual average absorption width in the x axis and the standard deviation of the nacelle acceleration in the y axis. These plots are the most important source of information in the present work and they are presented in sections 7.2.2, 7.3.2, 7.4.2 and 7.5.2.

It is important to mention that the objectives and logic just explained is almost the same for the isolated WEC calculation. The differences are that there is just one body with a single DOF and there is no nacelle.

A similar note applies for the FOWT. The calculations are the same, but since there are no WECs, there is no need to calculate absorption widths.

5.10.1 PTO damping optimization

The b_{PTO} value is optimized for each sea state in the operational subset following the procedure described in this section.

1. A range, in which the PTO damping varies, is established. For all DCs the range $(0, 3000)$ [tons/s] is enough.
2. A hundred values are considered within the b_{PTO} range. For each of them the RAOs are calculated, the curve absorbed power Vs frequency is constructed and the maximum value is saved. An example of this curve for FOHWEC DC1-D1 is included in Figure 32. In this case, the curve corresponds to the optimum b_{PTO} .

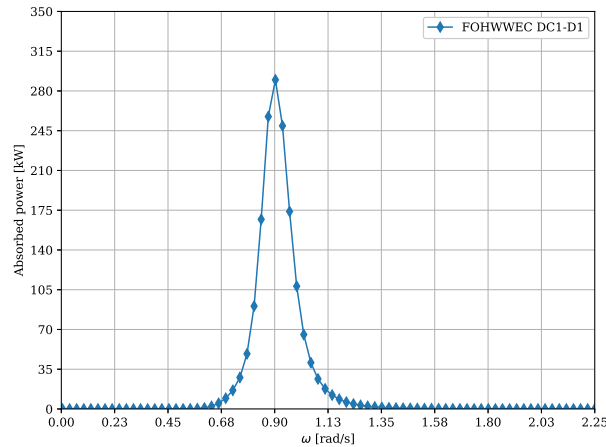


Figure 32: Absorbed power Vs frequency with optimum b_{PTO} for DC1-D1

3. The maximum absorbed power within the saved maxima in the previous step, is found. The b_{PTO} value corresponding to that maximum is the optimum one. Now, the curve absorbed power Vs PTO damping containing the maximum absorbed power can be constructed. An example of this curve for FOHWEC DC1-D1 is in Figure 33.

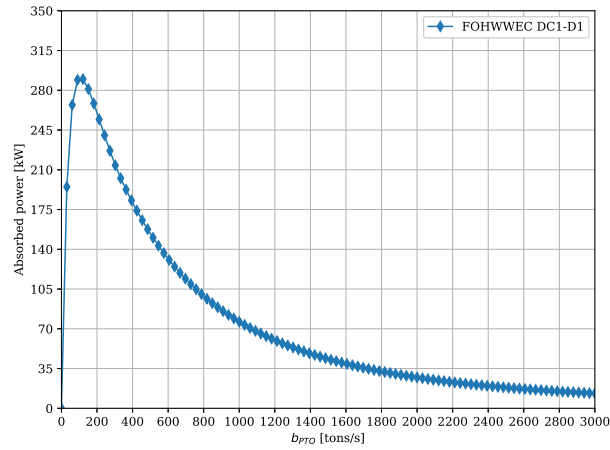


Figure 33: Absorbed power Vs b_{PTO} containing the maximum power for DC1-D1

It can be noticed how both curves coincide at the maximum absorbed power. They are indeed different 2D views of the 3D plot absorbed power Vs frequency Vs PTO damping. From Figure 33 the optimum b_{PTO} value can be estimated to be around 120tons/s. Indeed, it is reported in Table 24 as 121.2tons/s.

5.10.2 Performance variables definition

In this section the equations employed in the calculation of the performance variables are presented and explained.

- **Annual average absorption width:** In order to calculate this performance variable, the equation 92 is used to calculate the λ_p value for each sea state in the operational subset. Then, if there are n sea states in the operational subset, each of them occurs N_s times in a year and the sum of all sea state occurrences in the operational subset is N_{st} , the annual average absorption width ($\lambda_{p(avg)}$) is calculated by the following expression:

$$\lambda_{p(avg)} = \frac{1}{N_{st}} \sum_{i=1}^n N_{s_i} \cdot \lambda_{p_i} \quad (97)$$

- For the horizontal nacelle acceleration two versions of its standard deviation are used as performance variables:

1. Annual average standard deviation of the nacelle acceleration:

It is relevant to establish a comparison between the FOHWECs and the FOWTs. In order to calculate this performance variable, first the nacelle horizontal acceleration RAO (RAO_{aN_α}) is calculated. This calculation makes use of the following adapted version

of the motion superposition equation 12 and the harmonic acceleration definition 9:

$$\tilde{\eta}_{aN_a}(\omega) = -\omega^2 (\tilde{\eta}_1(\omega) + h_{n_a} \cdot \tilde{\eta}_5(\omega)) \quad (98)$$

$$RAO_{aN_a} = \sqrt{\Re\{\tilde{\eta}_{aN_a}\}^2 + \Im\{\tilde{\eta}_{aN_a}\}^2} \quad (99)$$

where,

$\tilde{\eta}_{aN_a}$ = Nacelle horizontal acceleration complex amplitude

$\tilde{\eta}_1$ = Surge motion complex amplitude

$\tilde{\eta}_5$ = Pitch motion complex amplitude

h_{n_a} = Vertical distance from CoG to nacelle

RAO_{aN_a} = Nacelle's horizontal acceleration RAO

Then, the nacelle acceleration motion spectrum ($S_{aN_a}(\omega)$) is calculated making use of an equation similar to 42 and the standard deviation of the spectrum (σ_{aN_a}) for each sea state in the operational subset is calculated as follows:

$$\sigma_{aN_a} = \sqrt{m_0} \quad (100)$$

where, m_0 is the zero moment of the spectrum.

Finally, the annual average standard deviation of the nacelle acceleration is obtained by using the following expression:

$$\sigma_{aN_a(\text{avg})} = \frac{1}{N_{st}} \sum_{i=1}^n N_{s_i} \cdot \sigma_{aN_{a_i}} \quad (101)$$

2. **Maximum standard deviation of the nacelle acceleration:** It is relevant to establish a comparison between the DCs and also to report it for each FOHWWEC. Maximum accelerations are critical for the FOHWWEC performance, since they cause maximum loads and moments. In order to calculate it, the same procedure as for the annual average is followed, with the exception of the last step; instead of calculating an average, the maximum value within the operational subset is taken.

VERIFICATION OF THE RESULTS

In this chapter the NEMOH generated hydrodynamic coefficients are verified and validated. It is important to perform this action because these coefficients are the main input for the motion and performance module.

Besides this, the verification of the RAO and wave power absorption results obtained from the motion and performance module is also performed in this chapter. This is also a necessary step to limit the uncertainty on the final results of the present research.

6.1 VERIFICATION AND VALIDATION OF THE NEMOH RESULTS

6.1.1 Verification of the panel length

As mentioned in section 5.5 a panel length of maximum $\lambda/8$ should be enough to obtain accurate hydrodynamic forces. Nevertheless, since the method is based on numerical simulations that are highly dependent on the length of the panel, it is worth to demonstrate that indeed the $\lambda/8$ limit guarantees accurate results.

In order to perform that demonstration, a mesh refinement test is proposed on a geometrical configuration similar to DC1's geometry. The test configuration is named as *DCt* and the only difference with respect to DC1 is the draft of the cylinder, which is set to 15m, much shorter than DC1's drafts, to limit the number of panels and accelerate the calculations. Three refinement levels of the mesh are evaluated: a fine mesh, a medium mesh and a coarse mesh. Each level corresponds to a panel length, as indicated in Table 15.

Mesh	Sphere panel length [m]	Cyl. panel length [m]
Fine	0.5	0.75
Medium	0.75	1.0
Coarse	1.0	1.5

Table 15: Mesh refinement levels

In this table, the cells highlighted in blue color correspond to the panel length values employed in the present work calculations. Notice that the panel length for the substructure is larger than that of the spheres. This is done to limit the amount of panels on the cylinder surface and therefore

reduce the time invested in the calculations.

A graphical representation of each refinement level is presented in figures 34, 35 and 36.

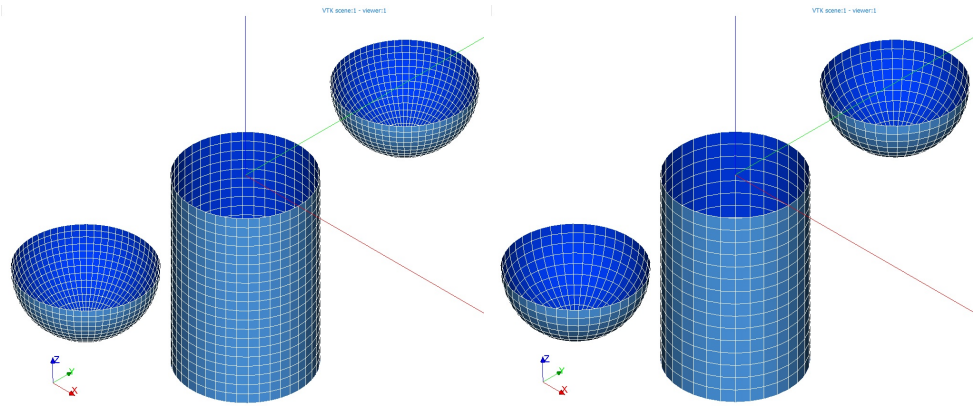


Figure 34: DCt with fine mesh

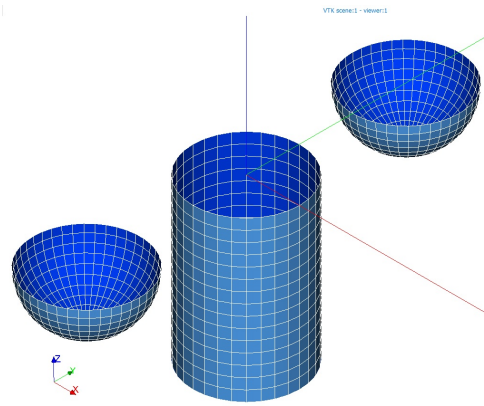


Figure 35: DCt with medium mesh

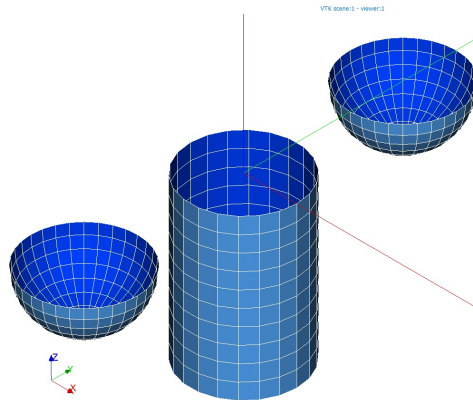


Figure 36: DCt with coarse mesh

The influence of the length of the panel on the NEMOH results is assessed on three added mass coefficients, three damping coefficients and three wave excitation forces. The plots portraying this influence can be found from Figure 37 until Figure 45. Notice that in these figures the superscript “AA” corresponds to the sphere on the positive y axis and “CC” corresponds to the cylinder. The meaning of these superscripts can be found in the Symbols list.

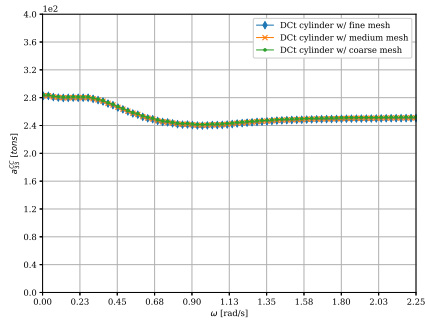


Figure 37: Mesh influence on heave added mass of cylinder

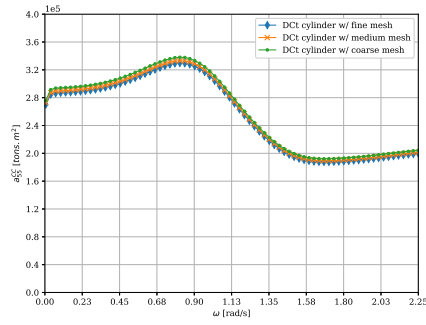


Figure 38: Mesh influence on pitch added mass of cylinder

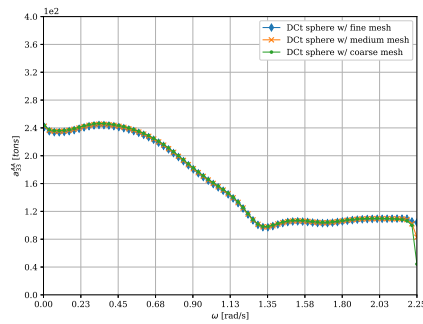


Figure 39: Mesh influence on heave added mass of sphere

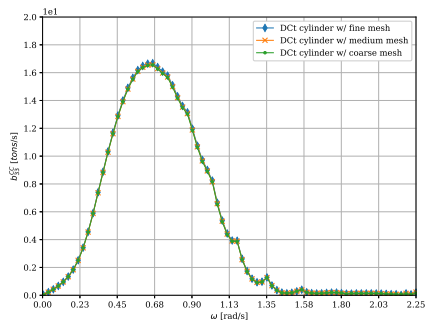


Figure 40: Mesh influence on heave damping of cylinder

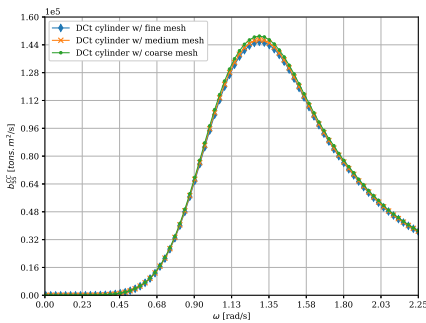


Figure 41: Mesh influence on pitch damping of cylinder

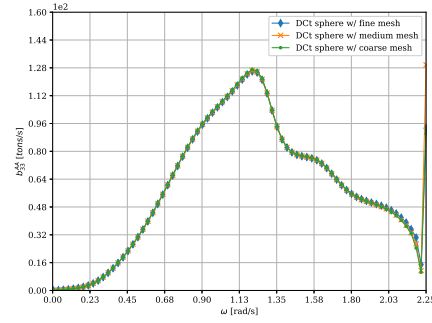


Figure 42: Mesh influence on heave damping of sphere

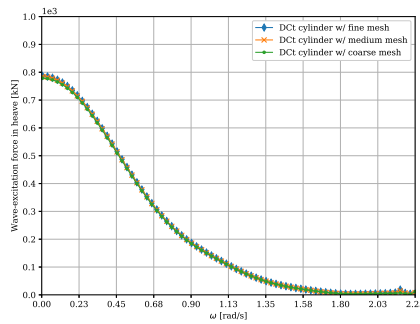


Figure 43: Mesh influence on heave wave excit. force of cyl.

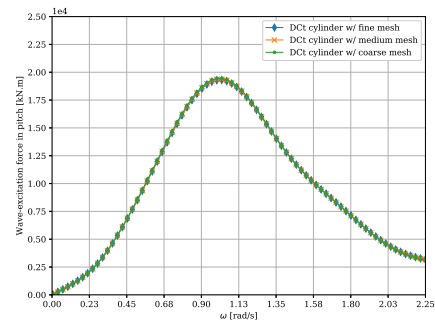


Figure 44: Mesh influence on pitch wave excit. force of cyl.

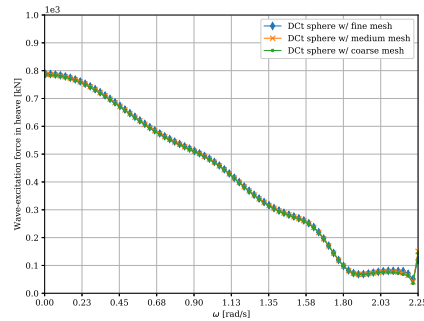


Figure 45: Mesh influence on heave wave excit. force of sphere

As it can be directly deduced from the plots, there are only minor differences between the NEMOH results obtained with the three different mesh refinements. If the fine mesh produces the most accurate results, then the differences produced by the medium and coarse meshes, with respect to the fine mesh, can be considered as errors. The maximum error values obtained from the analyzed NEMOH results are presented in Table 16.

Mesh	Max. error [%]
Medium	1.0
Coarse	2.5

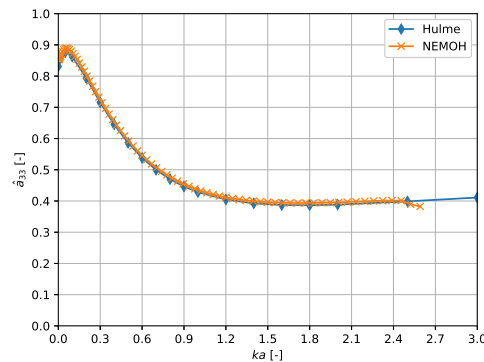
Table 16: Maximum error in NEMOH results

From these numbers it can be concluded that any combination of the sphere and cylinder mesh refinements considered in Table 15 leads to errors in the NEMOH results within 1% and 2.5%. These are considered limited error magnitudes that have a very limited influence on the performance variables. Therefore, the selected mesh refinement and its corresponding panel lengths are verified. They produce accurate enough hydrodynamic forces to be further employed in the calculation of the performance variables.

6.1.2 Validation of the hydrodynamic coefficients

Some of the hydrodynamic coefficients obtained from NEMOH can be validated against exact analytical solutions. For example, Hulme [43] derived in 1982 an exact solution for the added mass and damping of a floating heaving hemisphere. Since the added mass and damping of the heaving spherical PA are part of the EoM employed in all simulations, it makes sense to establish a direct comparison against Hulme's results to validate the values of a_{33} and b_{33} , further limiting the uncertainty of the final results.

The coefficients employed in the comparison are those of the isolated WEC simulation, because the conditions on which the hemisphere heaves are the same as in Hulme's problem. Since Hulme provided normalized values for a_{33} and b_{33} , the values obtained for the isolated WEC are normalized by $2\pi\rho r_{WEC}^3/3$ and $2\pi\omega\rho r_{WEC}^3/3$ respectively. The frequency is also normalized as $k r_{WEC}$, making use of the deep water dispersion relation (49). The result of the comparison is graphically portrayed in Figures 46 and 47.

Figure 46: Hulme and NEMOH results for the normalized coeff. \hat{a}_{33} of a heaving hemisphere

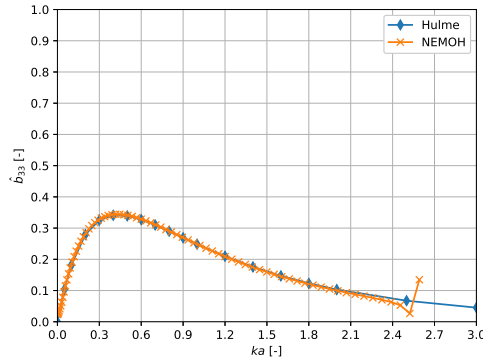


Figure 47: Hulme and NEMOH results for the normalized coeff. \hat{b}_{33} of a heaving hemisphere

As it can be seen, the agreement between values from NEMOH and values from Hulme's solution is very good. Since NEMOH has been validated for different types of floating bodies and under different conditions, it was expected to obtain this degree of agreement. Based on that, it is also expected the same degree of agreement is reached for the following cases:

1. A floating cylinder, representing the simplest substructure.
2. The combination of a floating cylinder and two floating spheres, representing the simplest case with hydrodynamic interaction between the substructure and two WECs.

It is assumed that the results are accurate for those cases and therefore the numerical results from NEMOH can be considered sufficiently close to the real values.

6.2 VERIFICATION OF THE MOTION AND PERFORMANCE MODULE

6.2.1 *Qualitative verification of the FOWT RAO calculation*

Once the panel length has been verified and the most important hydrodynamic coefficients, obtained from NEMOH, have been validated, it is necessary to determine if the equations of motion are solved in a correct manner.

In order to accomplish this, an investigation is performed to find RAO data of configurations similar to the ones analyzed in the present work. The simplest DC in the present research is DC₁ and the DC₁-D₁ FOWT is geometrically similar to the already proven HyWind FOWT. The National Renewable Energy Laboratory (NREL) has supported a paper developed by G.K.V. Ramachandran et al. [44] that investigates the HyWind's RAOs. Figures 48, 50 and 52 includes the HyWind RAO curves for surge, heave and pitch. Interspersed with these figures, three figures corresponding to the DC₁'s surge,

heave and pitch RAOs have been added (49, 51 and 53). It is important to notice that in all figures the frequency is presented in Hertz (Hz).

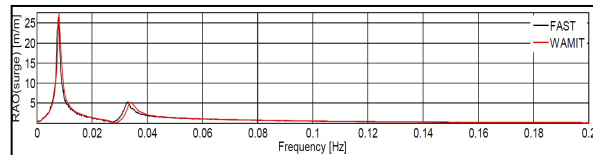


Figure 48: Surge RAO of HyWind FOWT [44]

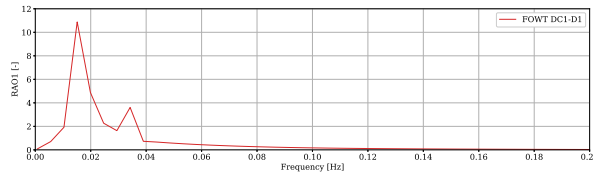


Figure 49: Surge RAO of DC1 FOWT

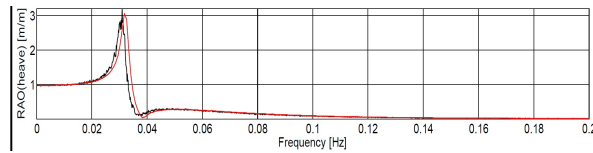


Figure 50: Heave RAO of HyWind FOWT [44]

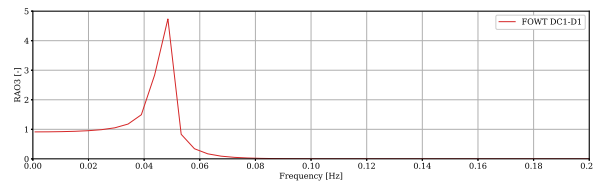


Figure 51: Heave RAO of DC1 FOWT

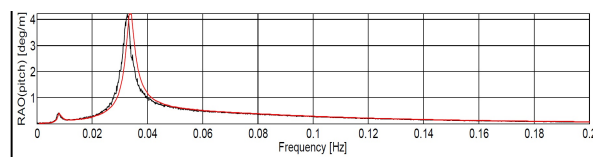


Figure 52: Pitch RAO of HyWind FOWT [44]

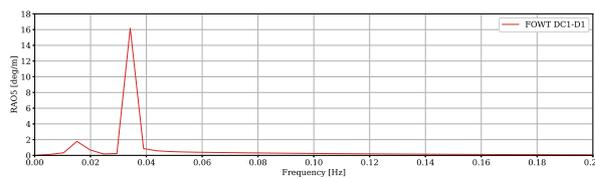


Figure 53: Pitch RAO of DC1 FOWT

Qualitatively, the HyWind curves are similar to the DC1's curves. In both cases the surge and pitch RAO curves have two peaks; one at surge resonance and the other at pitch resonance, demonstrating the coupling between the motions. The surge natural frequency has a value greater than zero in both cases, revealing the presence of a mooring system that adds surge restoring force. The heave RAO curve starts at 1, as expected in low frequencies, where the FOWT just follows the wave surface. All the natural frequencies are relatively low, as expected, since all FOWTs have a very large displacement.

Going more into detail, the natural frequencies are compared in Table 17. Although, HyWind and DC1's natural frequencies have the same order of magnitude, there are differences and the suspected reasons behind these differences are also included.

DOF/FOWT	HyWind	DC1-D1	Reason behind difference
1	0.008	0.017	①
3	0.032	0.047	②
5	0.034	0.033	③

Table 17: Natural frequencies of HyWind and DC1-D1 [Hz]

The reasons behind the differences are the following:

- ① = The mooring systems are different. HyWind fairleads are at 70m depth and the lines have 902m of unstretched length. DC1-D1's fairleads are at 10m depth and the lines have 750m of unstretched length. Those differences, among others, produce a higher surge restoring force for DC1-D1, in comparison with HyWind.
- ② = DC1-D1's displacement (9499.4tons) is relatively higher than HyWind's displacement (8229.7tons), but the hydrostatic heave restoring force of DC1-D1 is much higher than the HyWind one, because the substructure's diameter at the MSL of DC1-D1 is 10m and HyWind's diameter is 6.5m.

Additionally, the HyWind substructure's diameter is tapered, growing until 9.4m as the depth increases. This might be increasing the hydrodynamic damping in heave, in comparison with DC1-D1, explaining the higher heave peak amplitude for DC1-D1.

- ③ = Although the natural frequencies are almost the same for both, the pitch peak amplitude is higher for DC1-D1. This might be related to the tapered (conical) shape of HyWind's substructure that generates a higher hydrodynamic damping in pitch.

Based on the results of the comparison effort, it can be said that the EoMs for the FOWTs are solved in a correct manner.

6.2.2 Qualitative verification of the FOHWWEC RAO calculation

The EoMs of the FOHWWECs involve multi-body interaction and therefore it is more difficult to find appropriate data to be compared with the results of the present work. Nevertheless, the FOHWWEC's RAOs can be qualitative compared to the FOWT's RAOs using the figures 49, 51 and 53.

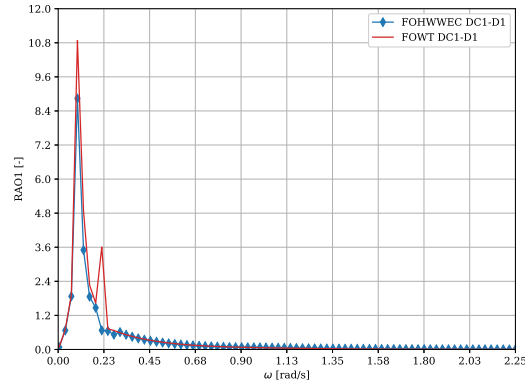


Figure 54: Surge RAO of DC1 FOHWWEC and FOWT

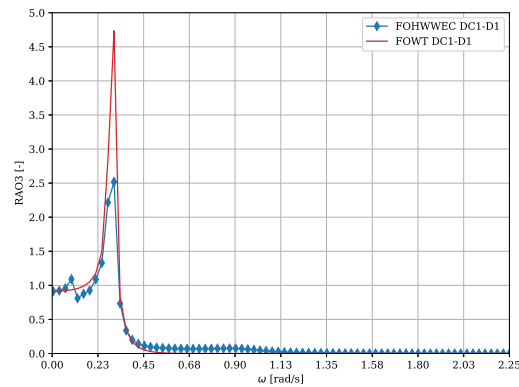


Figure 55: Heave RAO of DC1 FOHWWEC and FOWT

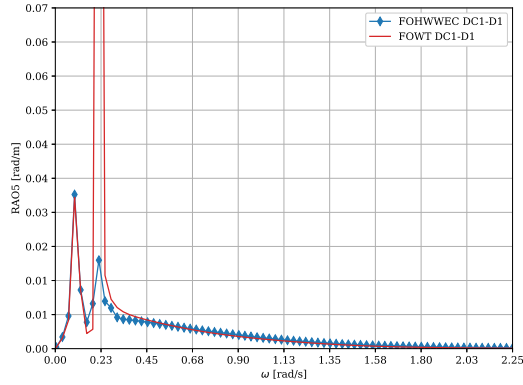


Figure 56: Pitch RAO of DC1 FOHWEC and FOWT

In Figure 54, although it is not clearly seen, the extra mass added by the WECs cause a decrease in the surge resonance frequency (from 0.109rad/s to 0.106rad/s). That is expected. There is also additional damping added by the WECs and therefore the resonance peak is shorter for the FOHWEC. The pitch resonance peak is almost not visible for the FOHWECs because the pitch damping added by the WECs limits the peak amplitude.

In Figure 55, it is clearly seen how the heave resonance frequency is almost equal for FOWT and FOHWEC. This is expected since the WECs are not adding mass to the FOWT because they are floating and they are neither adding hydrostatic restoring force, because there is no mechanical spring in the PTO system. Nevertheless, there is added damping and therefore the resonance peak amplitude of the FOHWEC is lower.

In Figure 56, although it is not clearly seen, the extra moment of inertia added by the WECs cause a decrease in the pitch resonance frequency (from 0.208rad/s to 0.185rad/s ; adding to this phenomena, the WEC's pitch restoring force is not effectively translated to the substructure because there is no mechanical spring in the PTO system. That is expected. There is additional damping added by the WECs and therefore the resonance peak amplitude is shorter for the FOHWEC.

Based on the previous analysis, it can be said that the DC1 FOHWEC RAOs are qualitatively verified against the DC1 FOWT RAOs. The verification is extrapolated to the other DCs because the calculation's logic is the same.

6.2.3 Verification of the power absorption calculation

The next step of the verification process is to demonstrate that the power absorption values, and therefore the absorption width values, are calculated in the correct manner. To accomplish that, the Budal diagram (Figure 20) ex-

plained in section 4.3 is employed. The idea is to see if the passive loading absorption curve for the isolated WEC falls in the appropriate position with respect to the theoretical upper bounds (P_A and P_B).

The same conditions used by Falnes [32] to construct Figure 20, are used to build-up the Budal diagram of the present research. It results in Figure 57.

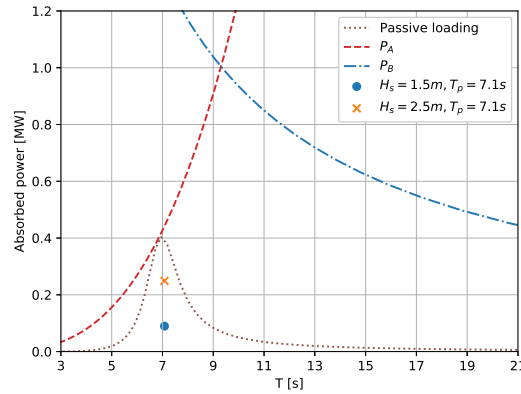


Figure 57: Budal diagram including results from the present study

As it can be seen, the passive loading curve falls just in the expected position, meaning that the calculation of the absorbed power by the isolated WEC is correct. The peak and the form of this curve is different than the one presented by Falnes. There are two reasons behind this difference. First, the WEC is ballasted with water in the present study. Second, Falnes considers a load-constrained heave motion, limited to 3m.

Besides this, the absorbed power obtained in irregular waves, specifically for sea state $H_s = 1.5\text{m}$, $T_p = 7.1\text{s}$ and sea state $H_s = 2.5\text{m}$, $T_p = 7.1\text{s}$ is included. Since the regular waves used to construct the diagram have a height of $H = 2.26\text{m}$, it is expected that the absorbed power for the mentioned sea states falls below the passive loading curve, because less power is absorbed in irregular waves than in regular waves. Indeed, that is the case, as shown in Figure 57. This demonstrates that the power absorption calculation in irregular waves is also correct.

From this verification an extrapolation is done for the absorbed power calculation of the FOHWECs, because the same power calculation's logic has been employed.

SIMULATION RESULTS

The four simulations planned in the methodology have produced results for each design configuration (DC). As mentioned in section 5.10, the most important results are presented in the performance plots for each DC (sections 7.2.2, 7.3.2 and 7.4.2) and for all DCs (section 7.5.2). The information in those plots is analyzed in the present chapter to address the objectives.

The analysis of the performance variables is based on intermediate results, such as the natural frequencies, RAOs, motion spectra, wave excitation forces, hydrodynamic coefficients and the operational subset matrices for PTO damping, absorption width and standard deviation of the nacelle acceleration. All the *intermediate results*, relevant to the performance analysis, are included in sections 7.1.1, 7.2.1, 7.3.1, 7.4.1 and 7.5.1. It is suggested that the reader proceeds first with reading the performance analyses. From there, proper references in the text point to the required intermediate result.

The analysis of the results is first focused on each DC (sections 7.2.2, 7.3.2 and 7.4.2). Then, the perspective is broadened to look at all DCs in the design space (section 7.5.2). This last section uses the word *combined* to indicate that data from the different DCs and the isolated WEC is used.

It is important to point out that the absorbed power/energy and the absorption width matrices, presented as intermediate results, are considering two WECs. This also applies for the isolated WEC simulation to facilitate the comparison with the FOHWECs.

7.1 ISOLATED WEC SIMULATION

The results for the isolated WEC are used as a power absorption reference. That means the results for the three design configurations are compared to the results of the isolated WEC, providing insight into the influence of the substructure on the absorbed power.

As mentioned at the beginning of this chapter, the reader can skip the section 7.1.1, where the intermediate results are presented, and continue with the analysis in section 7.1.2. In this analysis, proper references are made to the required intermediate result.

7.1.1 Relevant intermediate results

7.1.1.1 Natural frequency

In this section the natural frequency value of the heaving isolated WEC is presented. The value correspond to the wave frequency $\omega = 0.875\text{rad/s}$ which is the closest to the most common sea state peak period $T_p = 7.1\text{s}$.

ω_n [rad/s]
0.914

Table 18: Natural frequency of the isolated WEC

7.1.1.2 Motion spectrum

This section includes the relative heave motion spectrum plot for the isolated WEC. The data corresponds to the most common sea state in the operational range ($H_s = 1.5\text{m}$, $T_p = 7.1\text{s}$).

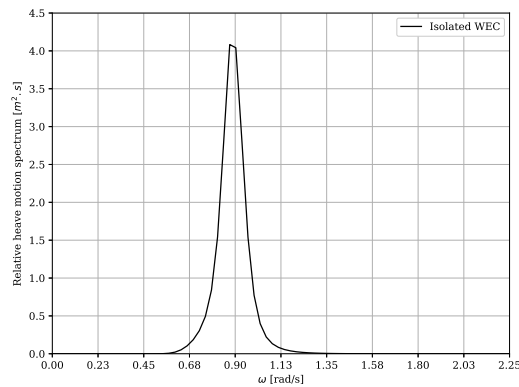


Figure 58: Rel. heave spectrum of isolated WEC

7.1.1.3 Response amplitude operator (RAO)

This section includes the heave RAO plot of the isolated WEC. As mentioned in section 5.3, there is no mooring system involved. The data is taken from the most common sea state ($H_s = 1.5\text{m}$, $T_p = 7.1\text{s}$).

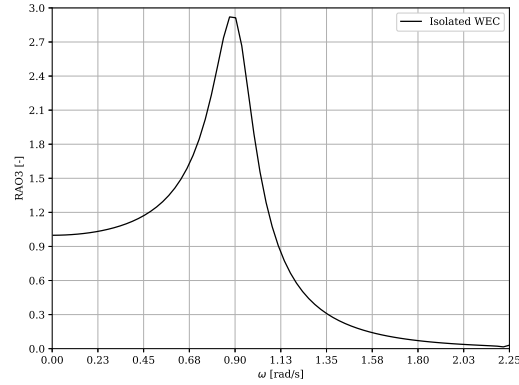


Figure 59: Heave RAO of isolated WEC

This RAO curve is also included in Figure 108, where it serves as a reference RAO to be compared with the relative heave RAO of each design configuration.

7.1.1.4 Optimized PTO damping matrix

The PTO damping coefficient (b_{PTO}) is optimized for each sea state in the operational range, following the procedure described in section 5.10.1. In the present section, the results are presented in matrix form.

H_s/T_p	4.5	5.8	7.1	8.4	9.6
0.5	636.4	242.4	90.9	333.3	545.5
1.5	636.4	242.4	90.9	333.3	545.5
2.5	636.4	242.4	90.9	333.3	545.5
3.5	636.4	242.4	90.9	333.3	545.5

Table 19: Isolated WECs optimal PTO damping coefficient [tons/s]

7.1.1.5 Absorbed power and energy matrices

Once the PTO damping is established and optimized, the absorbed power can be calculated for each sea state in the operational range, using equation 82. The results are presented in matrix form in Table 20.

Then, using equation 94 the absorbed energy in each sea state is calculated. The results are presented in matrix form in Table 21, including the row, column and total sums.

H_s/T_p	4.5	5.8	7.1	8.4	9.6
0.5	1.2	4.9	10.0	9.4	8.0
1.5	10.5	43.6	89.7	84.9	72.3
2.5	29.2	121.2	249.1	235.9	200.8
3.5	0.0	237.6	488.3	462.4	393.5

Table 20: Isolated WECs absorbed power per sea state [kW]

H_s/T_p	4.5	5.8	7.1	8.4	9.6	Sum
0.5	0.2	4.3	9.6	4.0	0.8	18.9
1.5	0.3	21.9	111.3	86.3	29.7	249.5
2.5	0.3	21.1	161.0	176.7	82.4	441.5
3.5	0.0	14.6	135.2	185.0	104.9	439.8
Sum	0.8	61.9	417.2	451.9	217.8	1149.7

Table 21: Isolated WECs absorbed energy per year [MWh/y]

7.1.1.6 Absorption width matrix

The absorption width (λ_p) is calculated through equation 92, using the absorbed power and the available power matrices. The values for each sea state in the operational range are presented here in meters.

It is important to notice that since both WECs are considered, a 100% efficiency is equal to an absorption width of 20m (two WECs of 10m diameter each).

H_s/T_p	4.5	5.8	7.1	8.4	9.6
0.5	2.5	7.7	12.8	10.2	7.5
1.5	2.5	7.7	12.8	10.2	7.5
2.5	2.5	7.7	12.8	10.2	7.5
3.5	2.5	7.7	12.8	10.2	7.5

Table 22: Isolated WECs absorption width [m]

7.1.2 Performance analysis

The only performance variable that can be calculated and analyzed for the isolated WECs is the annual average absorption width. Using the values in tables 20 and 13, together with equation 97, a value of $\lambda_{p(\text{avg})} = 10.1\text{m}$ is obtained. That means, in average each WEC is able to absorb approximately the power of a wave front equal to the half of its diameter. In other words, the average absorption efficiency is about 50%. Here it is important to men-

tion that the efficiency can be above 50% (see peak frequencies $T_p = 7.1s$ and $T_p = 8.4s$ in Table 22), because it is not a planar (2D) situation and the incoming wave diffracts in the sphere surface.

As indicated by equation 82, this absorption width depends on the WEC's heave spectra. One of these spectra is portrayed in Figure 58. This spectrum has a T_p of 7.1s, which is the closest to the WEC natural frequency of 0.914rad/s. Therefore, it is the motion spectrum of the WEC in resonance or, in other words, where the heave RAO is maximum as shown in Figure 59. Then, it is known, by the deduction from equation 87, that the minimum b_{PTO} and the maximum absorbed power and absorption width should be obtained at this resonance frequency. This is indeed demonstrated by the values under $T_p = 7.1s$ in tables 19, 20 and 22.

Further advantage is taken from these maximum absorbed power values, because the sea state $H_s = 1.5m$, $T_p = 7.1s$ is the one with more occurrences in the operational subset. More occurrences are translated in more hours per year of that sea state. Therefore, a value of 113.3MWh of absorbed energy is obtained at that sea state, and that value is maximum for sea states with $H_s = 1.5m$.

The previous paragraphs explain why in all simulations the WEC's natural frequency is tuned to the peak frequency $T_p = 7.1s$. They also explain why the motion spectra and RAOs used in the analysis of all simulations are the ones generated in the sea state $H_s = 1.5m$, $T_p = 7.1s$.

Another point to highlight in Table 22 is that the values in high peak periods are greater than the values in low peak periods. This is explained by a combination of two elements:

1. First, greater RAO values in low frequencies, where the sphere follows the wave elevation, than in high frequencies, where the sphere inertia dominates. These RAO values are a product of higher heave wave excitation forces in low frequencies, as it can be seen in Figure 111.
2. Second, the fact that high peak period spectra consist of low frequency wave components. Due to this, the low frequency RAO values are captured and multiplied by those spectrum values, producing greater absorbed power values.

7.2 DC1 SIMULATION

As mentioned at the beginning of this chapter, the reader can skip the section 7.2.1, where the intermediate results are presented, and continue with the analysis in section 7.2.2. In this analysis, proper references are made to the required intermediate result.

7.2.1 Relevant intermediate results

7.2.1.1 Natural frequencies

In this section the natural frequencies values for each DOF of DC₁ are presented. The values correspond to the wave frequency $\omega = 0.875 \text{ rad/s}$ which is the closest to the peak period $T_p = 7.1 \text{ s}$.

DOF/FOHWWEC	DC ₁ -D ₁	DC ₁ -D ₂	DC ₁ -D ₃
1	0.106	0.103	0.099
3	0.296	0.284	0.274
WEC ₃	0.931	0.931	0.931
5	0.185	0.191	0.195

Table 23: Natural frequencies of DC₁ FOHWWECs

7.2.1.2 Motion spectrum

This section includes the motion spectrum plots which are relevant for the analysis of the results of DC₁. The data corresponds to the most common sea state in the operational range ($H_s = 1.5 \text{ m}$, $T_p = 7.1 \text{ s}$).

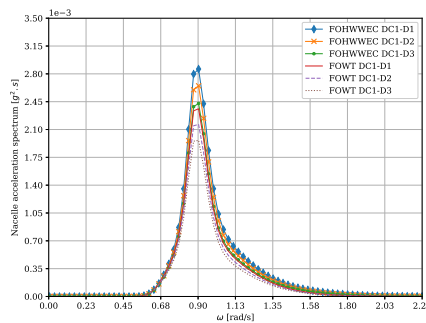


Figure 60: Nacelle acc. spectrum of DC₁ FOHWWECs

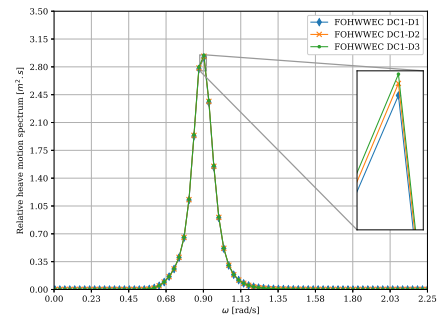


Figure 61: Rel. heave spectrum of WEC on DC₁ FOHWWECs

7.2.1.3 Response amplitude operators (RAOs)

This section includes the RAO plots which are relevant for the analysis of the results. Two groups of plots are identified. The first group portrays the effect of draft variation for FOHWWECs. The second group presents the same, but for the FOWTs (without WECs).

As it is done for the spectra in the previous section, the RAO data is taken as well from the most common sea state ($H_s = 1.5 \text{ m}$, $T_p = 7.1 \text{ s}$).

GROUP 1: FOHWWECC RAOs for each draft level

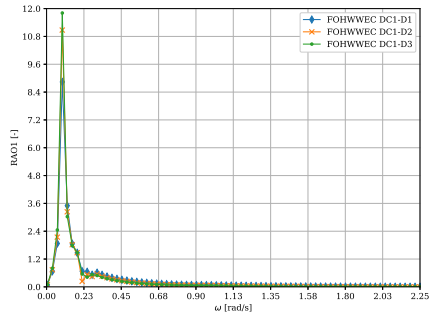


Figure 62: Surge RAO of DC1 FOHWWECCs

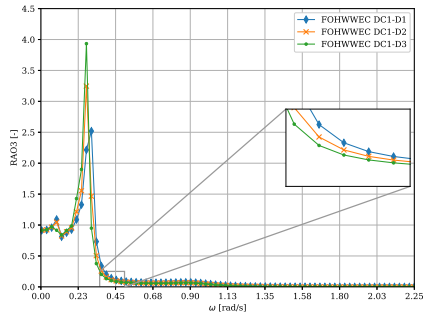


Figure 63: Heave RAO of DC1 FOHWWECCs

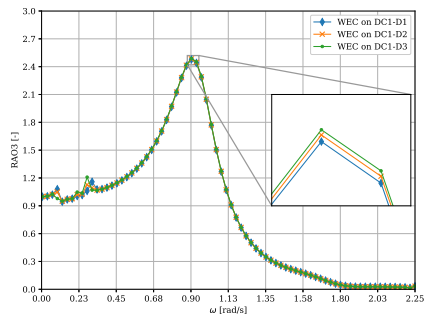


Figure 64: Heave RAO of WEC on DC1 FOHWWECCs

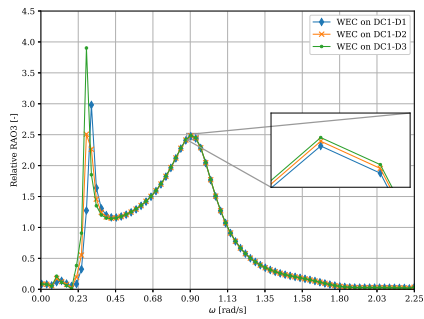


Figure 65: Rel. heave RAO of WEC on DC1 FOHWWECCs

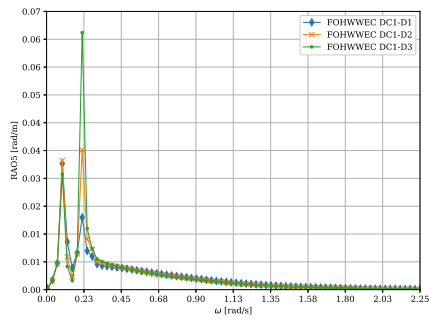


Figure 66: Pitch RAO of DC1 FOHWWECCs

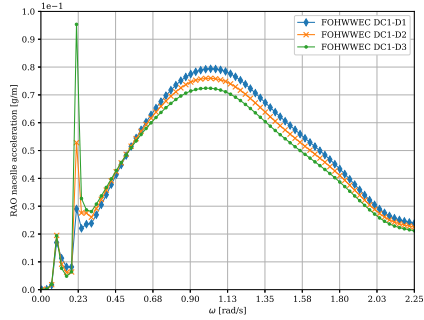


Figure 67: Nacelle acc. RAO of DC1 FOHWWECCs

GROUP 2: FOWT RAOs for each draft level

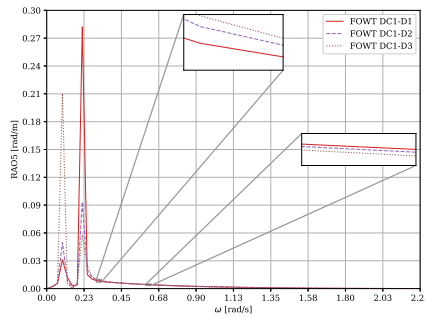


Figure 68: Pitch RAO of DC1 FOWTs

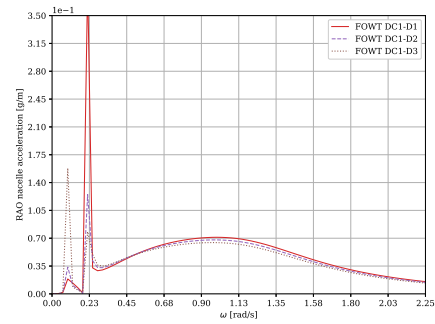


Figure 69: Nacelle acc. RAO of DC1 FOWTs

7.2.1.4 Wave excitation forces

This section includes the wave excitation force plots which are relevant for the analysis of the results of DC1.

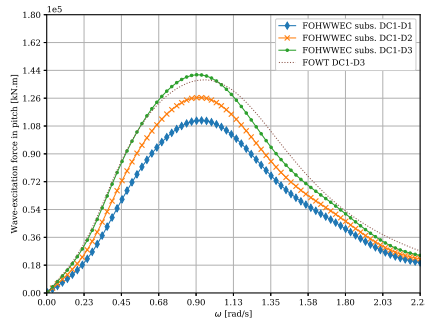


Figure 70: Pitch wave excitation force on DC1 subs. and FOWT

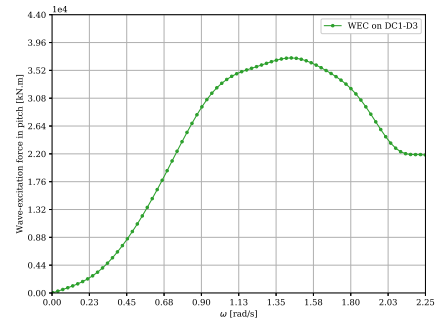


Figure 71: Pitch wave excitation force on DC1-D3 WEC

7.2.1.5 Optimized PTO damping matrix

The PTO damping coefficient (b_{PTO}) is optimized for each sea state in the operational range, following the procedure described in section 5.10.1. In the present section, the results are presented in matrix form.

H_s/T_p	4.5	5.8	7.1	8.4	9.6
0.5	515.2	181.8	121.2	333.3	515.2
1.5	515.2	181.8	121.2	333.3	515.2
2.5	515.2	181.8	121.2	333.3	515.2
3.5	515.2	181.8	121.2	333.3	515.2

Table 24: DC1-D1 optimal PTO damping coefficient [tons/s]

H_s/T_p	4.5	5.8	7.1	8.4	9.6
0.5	515.2	181.8	121.2	333.3	545.5
1.5	515.2	181.8	121.2	333.3	545.5
2.5	515.2	181.8	121.2	333.3	545.5
3.5	515.2	181.8	121.2	333.3	545.5

Table 25: DC1-D2 and DC1-D3 optimal PTO damping coefficient [tons/s]

7.2.1.6 Absorbed power and energy matrices

Once the PTO damping is established and optimized, the absorbed power can be calculated for each sea state in the operational range, using equation 82. The results are presented in matrix form in tables 26, 27 and 28.

Then, each of the values in the absorbed power matrices is multiplied by the amount of hours per year corresponding to the applicable sea state, to obtain the absorbed energy matrices. These matrices are included in Appendix A.

H_s/T_p	4.5	5.8	7.1	8.4	9.6
0.5	1.4	6.2	10.9	9.1	7.5
1.5	12.4	56.1	98.5	81.8	67.8
2.5	34.4	155.8	273.6	227.4	188.3
3.5	0.0	305.3	536.3	445.6	369.0

Table 26: DC1-D1 absorbed power per sea state [kW]

H_s/T_p	4.5	5.8	7.1	8.4	9.6
0.5	1.4	6.3	11.0	9.2	7.6
1.5	12.7	56.5	99.0	82.9	68.5
2.5	35.1	157.1	275.0	230.3	190.2
3.5	0.0	307.8	539.0	451.4	372.9

Table 27: DC1-D2 absorbed power per sea state [kW]

H_s/T_p	4.5	5.8	7.1	8.4	9.6
0.5	1.4	6.3	11.0	9.3	7.7
1.5	12.9	56.9	99.4	83.8	69.7
2.5	35.8	158.1	276.2	232.7	193.6
3.5	0.0	309.9	541.3	456.2	379.4

Table 28: DC1-D3 absorbed power per sea state [kW]

7.2.1.7 Absorption width matrix

The absorption width (λ_p) is calculated through equation 92, using the absorbed power and the available power matrices. The values for each sea state in the operational range are presented here in meters.

It is important to notice that since both WECs are considered, a 100% efficiency is equal to an absorption width of 20m (two WECs of 10m diameter each).

H_s/T_p	4.5	5.8	7.1	8.4	9.6	H_s/T_p	4.5	5.8	7.1	8.4	9.6
0.5	2.9	9.9	14.0	9.8	7.0	0.5	3.0	10.0	14.1	10.0	7.1
1.5	2.9	9.9	14.0	9.8	7.0	1.5	3.0	10.0	14.1	10.0	7.1
2.5	2.9	9.9	14.0	9.8	7.0	2.5	3.0	10.0	14.1	10.0	7.1
3.5	0.0	9.9	14.0	9.8	7.0	3.5	0.0	10.0	14.1	10.0	7.1

Table 29: DC1-D1 absorption width [m] Table 30: DC1-D2 absorption width [m]

H_s/T_p	4.5	5.8	7.1	8.4	9.6
0.5	3.0	10.0	14.2	10.1	7.2
1.5	3.0	10.0	14.2	10.1	7.2
2.5	3.0	10.0	14.2	10.1	7.2
3.5	0.0	10.0	14.2	10.1	7.2

Table 31: DC1-D3 absorption width [m]

7.2.1.8 Standard deviation of the nacelle acceleration matrix

The standard deviation of the nacelle acceleration is calculated through equation 100. The values for each sea state in the operational range are presented here in g units. In this section, only the values for the FOHWECs are included. The matrices for the FOWTs can be found in Appendix A.

H_s/T_p	4.5	5.8	7.1	8.4	9.6
0.5	0.007	0.009	0.009	0.009	0.008
1.5	0.021	0.026	0.027	0.026	0.024
2.5	0.036	0.044	0.046	0.044	0.041
3.5	0.0	0.062	0.064	0.061	0.057

Table 32: DC1-D1 standard deviation of the nacelle acceleration [g]

H_s/T_p	4.5	5.8	7.1	8.4	9.6
0.5	0.007	0.008	0.009	0.008	0.008
1.5	0.020	0.025	0.026	0.025	0.024
2.5	0.034	0.042	0.044	0.042	0.040
3.5	0.0	0.059	0.061	0.059	0.056

Table 33: DC1-D2 standard deviation of the nacelle acceleration [g]

H_s/T_p	4.5	5.8	7.1	8.4	9.6
0.5	0.006	0.008	0.008	0.008	0.008
1.5	0.019	0.024	0.025	0.024	0.023
2.5	0.032	0.040	0.042	0.041	0.039
3.5	0.0	0.056	0.059	0.057	0.054

Table 34: DC1-D3 standard deviation of the nacelle acceleration [g]

The highlighted cells are the minimum value (blue) and maximum value (red). Both are important to define the standard deviation fluctuation.

7.2.2 Performance analysis

The analysis performed for the isolated WEC is also applicable to DC1. The difference for DC1 is that not only one, but two performance variables can be analyzed. This analysis is based on the performance plot.

Figure 72 is DC1's performance plot. It has $\lambda_{p(\text{avg})}$ in the x axis and σ_{aNa} in the y axis. The diamond, cross and circle symbols indicate the performance variable value for each draft level. The vertical bars represent $\sigma_{aNa(\text{max})}$ and $\sigma_{aNa(\text{min})}$. The horizontal lines are the $\sigma_{aNa(\text{avg})}$ values of DC1 FOWTs.

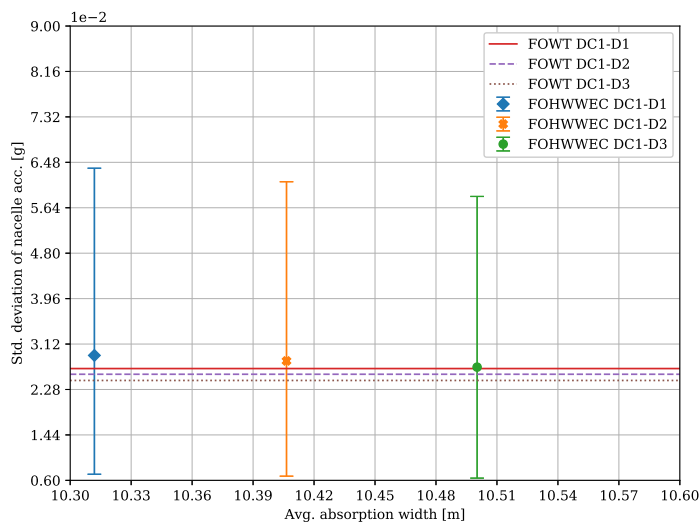


Figure 72: DC1 performance plot

These performance values are also included in Table 35.

Perf. variable	DC1-D1	DC1-D2	DC1-D3
$\lambda_{p(\text{avg})}$ [m]	10.31	10.41	10.50
$\sigma_{aN_a(\text{avg})}$ [g]	0.029	0.028	0.027

Table 35: Performance variable values of DC1 FOHWWECS

DC1-D3 has the higher $\lambda_{p(\text{avg})}$, just 1% higher than DC1-D2 value and 2% higher than DC1-D1 value. It also has the lower $\sigma_{aN_a(\text{avg})}$, just 7% lower than DC1-D1 value. This indicates that the draft seems to have a limited impact on the performance variables of DC1 FOHWWECS.

Since the performance variables depend on the motion spectra (see equations 82 and 100), limited changes with varying draft are then expected in those spectra. In figures 60 and 61 there are indeed limited differences between the draft levels for the WEC's relative heave motion spectrum (see zoomed-in plot) and more considerable differences in the nacelle acceleration spectrum. In both cases, the spectrum magnitudes help explaining the positions of each draft in the performance plot.

Once the relation between the motion spectra and the performance variables is demonstrated, it is necessary to analyze what is behind the variation of the spectra. This analysis is presented in the following sections.

7.2.2.1 The effect of draft and geometry

A deeper draft means a larger displacement. This produces a lower heave natural frequency since the heave restoring coefficient is constant for all drafts (see equation 21). Of course, this is a simplified logic because with multiple DOFs, the natural frequencies (eigen-frequencies) are found by solving the coupled equation 33. Despite the simplification, Table 23 indicates that certainly DC1-D3 FOHWWEC resonates at the lowest frequency, farther apart from the WEC's resonance frequency.

A deeper draft also means a larger inertia. DC1-D3 has more resistance to change its motion and this is specially noticeable in the inertia-dominated high frequency area, where DC1-D3 RAO values are the lowest (see zoomed-in plot in Figure 63).

Both effects, a lower natural frequency and larger inertia, allow the WEC to develop its motion in a more independent manner. As it can be noticed in the zoomed-in plots of figures 64 and 65, where the RAO reaches slightly greater values for DC1-D3 than for the other two draft levels. This finally leads to a slightly larger relative heave motion spectrum.

Moving on to the effect on the nacelle acceleration spectra, the first plot to be investigated is Figure 67. Here an inversion in the order of the curves is noticed; DC1-D3 values are the greatest until $\omega \approx 0.5\text{rad/s}$, after that, DC1-D1 values are the greatest. Although this inversion is not captured by the most common sea state spectrum, whose frequency range starts at $\omega \approx 0.68\text{rad/s}$, it is worth to study its causes.

Equation 98 presents the possible origins of the inversion: Surge and pitch motions, the distance from the CoG to the nacelle (h_{na}) and the frequency. The same inversion is only identified in the pitch RAO (see zoomed-in plots in Figure 66). On top of this, h_{na} multiplies only the pitch motion. In consequence, it can be considered that the nacelle acceleration RAO is mainly influenced by the pitch RAO and the h_{na} distance.

Now, why the inversion happens in the pitch RAO?. The answer relates to the pitch natural frequencies and the inertia. According to Table 23, DC1-D3 has the highest pitch natural frequency and DC1-D1 the lowest. The higher pitch resonance frequency, combined with larger moments of inertia, makes DC1-D3 pitch RAO curve to be in higher position after resonance, but to decay faster. The contrary occurs for DC1-D1 pitch RAO curve and that is why the curves cross each other.

Summarizing, for DC1-D1, a shorter h_{na} , but larger pitch RAO values in the inertia-dominated frequency area produces greater RAO_{aNa} and S_{aNa} values. For DC3-D3, a larger h_{na} , but lower pitch RAO values in the inertia-dominated frequency area produces lower RAO_{aNa} and S_{aNa} values. The root cause is the inertia combined with the majority of the wave spectra having frequency ranges starting at frequencies higher than $\omega = 0.5\text{rad/s}$ (see Figure 31).

7.2.2.2 The effect of WEC addition

Figure 72 also includes the $\sigma_{aNa(\text{avg})}$ for the FOWTs. Comparing these values with $\sigma_{aNa(\text{avg})}$ for the FOHWWECs, the latter are higher than the former ones for all draft levels.

To find the cause of this result, figures 66 and 68 are compared. Although it is difficult to directly see it, the pitch RAO values for the FOWTs are above the pitch RAO values for the FOHWWECs until $\omega \approx 0.56\text{rad/s}$. After that frequency, the FOHWWEC values are greater. The order is dictated by the pitch wave excitation forces, as it can be seen in Figure 70 for DC2-D3 FOWT and FOHWWEC substructure. Here the effect of WEC addition is palpable throughout the frequency range because the FOHWWEC and FOWT curves differ from each other. The main mechanism causing the differences is wave interaction between diffracted waves from the WT cylinder and from the WECs. This is further discussed in section 7.2.2.3.

On top of that, the WECs move together with the substructure in pitch and they add not only inertia, but also extra wave excitation forces. The force plotted in Figure 71 is added to the FOHWWEC system, while the FOWTs do not experience them.

In summary, the presence of the WECs modifies the wave excitation forces on the substructure through diffraction effects and the addition of pitch wave excitation loads. Both effects are the root cause of larger pitch RAO values, larger RAO_{aNa} values and finally greater S_{aNa} values for the FOHWWECs, in comparison with the FOWTs.

7.2.2.3 *The effect of wave diffraction*

The two WECs and the substructure diffract the incoming waves. There is then interaction between the diffracted waves, which modifies the wave excitation forces on the substructure and on the WECs. This could also affect the absorbed power and the nacelle acceleration and that is the analysis performed in this section.

Vasilikis [29] clearly identify fluctuations, due to wave diffraction, in the wave excitation forces and the RAOs of two floating vertical cylinders placed in a row. The fluctuations appear for both, 0 deg and 90 deg waves. For 0 deg waves, the fluctuations are stronger for the cylinder located in the shadow region. Considering this, it is worth to see if those fluctuations appear, specially on the wave excitation force and heave RAO of the WECs.

Starting with the heave RAO, a very small fluctuation is visible around $\omega = 1.58\text{rad/s}$ in Figure 64. Nevertheless, it is not conclusive. The pitch RAO curve (Figure 66) does not seem to have fluctuations. Looking at the pitch wave excitation force in Figure 70, again the fluctuation around $\omega = 1.58\text{rad/s}$ is visible and it is not present for the FOWT. Therefore, it is produced by wave diffraction interaction between the WECs and the substructure. Analyzing the heave wave excitation force on the WEC, depicted in Figure 111, the DC1-D3 curve presents fluctuations at $\omega \approx 1.0\text{rad/s}$ and $\omega \approx 1.58\text{rad/s}$. It is also noticeable how the DC1-D3 curve remains above the isolated WEC curve until $\omega \approx 1.70\text{rad/s}$. This is an enhancement of the heave wave excitation force on the WEC, and it is thought to be produced by positive wave interaction at the WEC's position.

This enhancement is actually what produces larger relative heave motion amplitudes for DC1's WEC, in comparison with the isolated WEC case. This is not noticeable for low frequencies (below $\omega = 0.9\text{rad/s}$) in Figure 108 due to the DC1's larger b_{PTO} value in comparison with the isolated WEC, but it is visible in high frequencies. This leads to greater spectrum values and finally to higher $\lambda_{p(\text{avg})}$ values for DC1 in comparison with the isolated WEC case, as portrayed in Figure 113.

The effect of wave diffraction on the nacelle acceleration has been identified in section 7.2.2.2. The pitch wave excitation force fluctuates for the FOHWWEC substructure because there is wave interaction between the diffracted waves (see Figure 70). This effect transfers to the σ_{aNa} values, through the pitch motion. Nevertheless, these are not large amplitude fluctuations, in comparison with the ones that will be presented for DC2 and DC3.

7.3 DC2 SIMULATION

As mentioned at the beginning of this chapter, the reader can skip the section 7.3.1, where the intermediate results are presented, and continue with the analysis in section 7.3.2. In this analysis, proper references are made to the required intermediate result.

7.3.1 Relevant intermediate results

7.3.1.1 Natural frequencies

In this section the natural frequencies values for each DOF of DC2 are presented. The values correspond to the wave frequency $\omega = 0.875\text{rad/s}$ which is the closest to the peak period $T_p = 7.1\text{s}$.

DOF/FOHWWEC	DC2-D1	DC2-D2	DC2-D3
1	0.094	0.088	0.083
3	0.421	0.388	0.362
WEC3	0.950	0.945	0.943
5	0.292	0.297	0.299

Table 36: Natural frequencies of DC2 FOHWWECs

7.3.1.2 Motion spectrum

This section includes the motion spectrum plots which are relevant for the analysis of the results of DC2. The data corresponds to the most common sea state in the operational range ($H_s = 1.5\text{m}, T_p = 7.1\text{s}$).

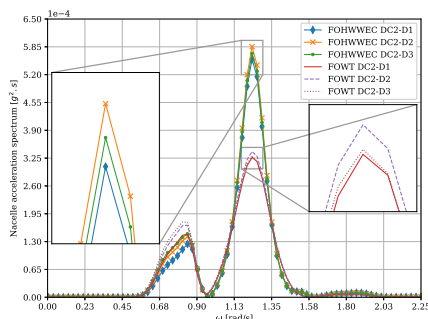


Figure 73: Nacelle acc. spectrum of DC2 FOHWWECs

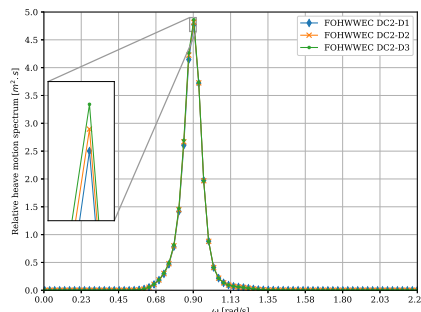


Figure 74: Rel. heave spect. of WEC on DC2 FOHWWECs

7.3.1.3 Response amplitude operators (RAOs)

This section includes the two groups of RAO plots which are relevant for the analysis of the results. The first group portrays the effect of draft variation for FOHWWECS. The second group presents the same, but for the FOWTs.

As it is done for the spectra in the previous section, the RAO data is taken as well from the most common sea state $H_s = 1.5\text{m}$, $T_p = 7.1\text{s}$ (sea state 1) and for sea state $H_s = 1.5\text{m}$, $T_p = 9.6\text{s}$ (sea state 2).

GROUP 1: FOHWWEC RAOs for each draft level

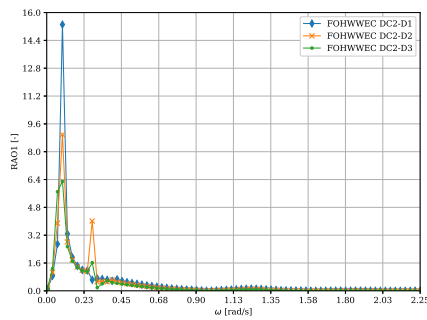


Figure 75: Surge RAO of DC2 FOHWWECS

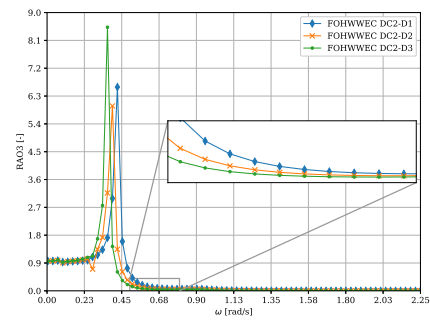


Figure 76: Heave RAO of DC2 FOHWWECS

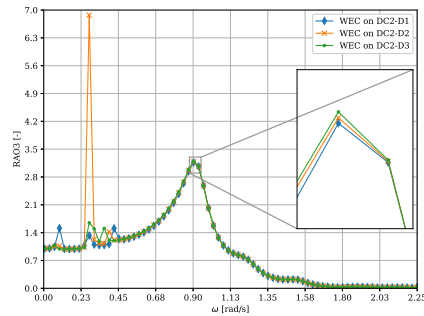


Figure 77: Heave RAO of WEC on DC2 FOHWWECS

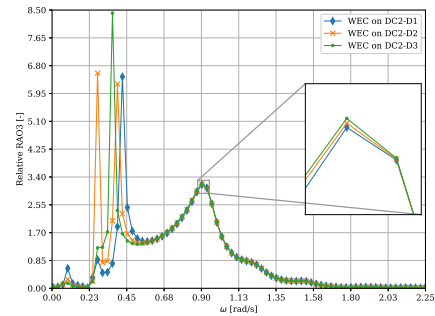


Figure 78: Rel. heave RAO of WEC on DC2 FOHWWECS

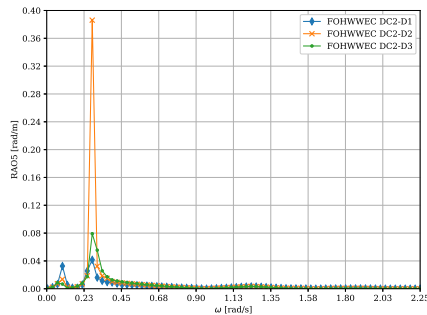


Figure 79: Pitch RAO of DC2 FOHWWECS

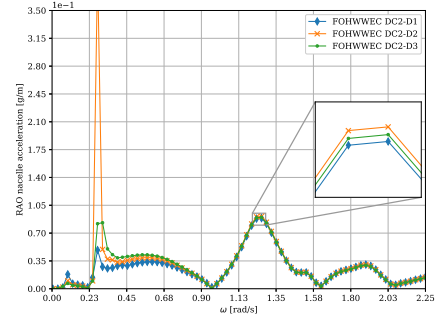


Figure 80: Nacelle acc. RAO of DC2 FOHWWECS

GROUP 2: FOWT RAOs for each draft level

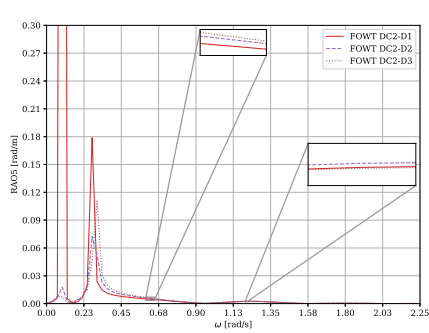


Figure 81: Pitch RAO of DC2 FOWTs

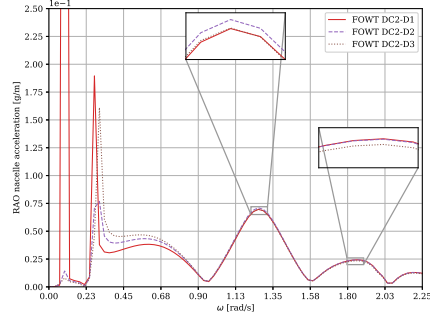


Figure 82: Nacelle acc. RAO of DC2 FOWTs

7.3.1.4 Wave excitation forces

This section includes the wave excitation force plots which are relevant for the analysis of the results of DC2.

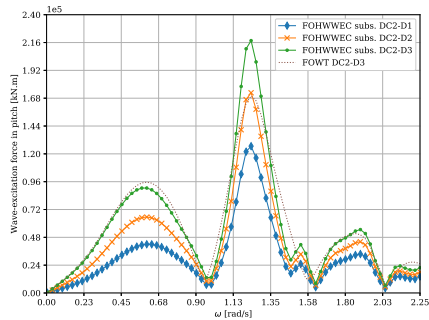


Figure 83: Pitch wave excitation force on DC2 subs. and FOWT

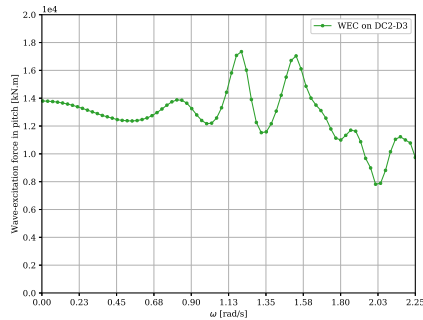


Figure 84: Pitch wave excitation force on DC2-D3 WEC

7.3.1.5 Optimized PTO damping matrix

The PTO damping coefficient (b_{PTO}) is optimized for each sea state in the operational range, following the procedure described in section 5.10.1. In the present section, the results are presented in matrix form.

H_s/T_p	4.5	5.8	7.1	8.4	9.6
0.5	363.6	90.9	90.9	393.9	545.5
1.5	363.6	90.9	90.9	393.9	545.5
2.5	363.6	90.9	90.9	393.9	545.5
3.5	363.6	90.9	90.9	393.9	545.5

Table 37: DC2-D1 and DC2-D2 optimal PTO damping coefficient [tons/s]

H_s/T_p	4.5	5.8	7.1	8.4	9.6
0.5	393.9	60.6	90.9	363.6	545.5
1.5	393.9	60.6	90.9	363.6	545.5
2.5	393.9	60.6	90.9	363.6	545.5
3.5	393.9	60.6	90.9	363.6	545.5

Table 38: DC2-D3 optimal PTO damping coefficient [tons/s]

7.3.1.6 Absorbed power and energy matrices

Once the PTO damping is established and optimized, the absorbed power can be calculated for each sea state in the operational range, using equation 82. The results are presented in matrix form in tables 39, 40 and 41.

Then, each of the values in the absorbed power matrices is multiplied by the amount of hours per year corresponding to the applicable sea state, to obtain the absorbed energy matrices. These matrices are included in Appendix A.

H_s/T_p	4.5	5.8	7.1	8.4	9.6
0.5	1.2	4.7	11.1	10.0	8.4
1.5	11.2	42.0	99.8	90.3	75.8
2.5	31.1	116.8	277.1	250.8	210.7
3.5	0.0	228.9	543.1	491.6	412.9

Table 39: DC2-D1 absorbed power per sea state [kW]

H_s/T_p	4.5	5.8	7.1	8.4	9.6
0.5	1.3	4.7	11.2	10.2	8.5
1.5	11.6	42.2	100.7	92.2	76.3
2.5	32.3	117.2	279.8	256.2	212.0
3.5	0.0	229.7	548.5	502.1	415.4

Table 40: DC2-D2 absorbed power per sea state [kW]

H_s/T_p	4.5	5.8	7.1	8.4	9.6
0.5	1.3	3.9	11.3	10.3	8.6
1.5	11.9	35.3	101.4	93.0	77.2
2.5	33.1	98.2	281.6	258.3	214.3
3.5	0.0	192.4	551.9	506.2	420.1

Table 41: DC2-D3 absorbed power per sea state [kW]

7.3.1.7 Absorption width matrix

The absorption width (λ_p) is calculated through equation 92, using the absorbed power and the available power matrices. The values for each sea state in the operational range are presented here in meters.

It is important to notice that since both WECs are considered, a 100% efficiency is equal to an absorption width of 20m (two WECs of 10m diameter each).

H_s/T_p	4.5	5.8	7.1	8.4	9.6	H_s/T_p	4.5	5.8	7.1	8.4	9.6
0.5	2.6	7.4	14.2	10.6	7.9	0.5	2.8	7.4	14.4	11.1	7.9
1.5	2.6	7.4	14.2	10.6	7.9	1.5	2.8	7.4	14.4	11.1	7.9
2.5	2.6	7.4	14.2	10.6	7.9	2.5	2.8	7.4	14.4	11.1	7.9
3.5	0.0	7.4	14.2	10.6	7.9	3.5	0.0	7.4	14.4	11.1	7.9

Table 42: DC2-D1 absorption width [m] Table 43: DC2-D2 absorption width [m]

H_s/T_p	4.5	5.8	7.1	8.4	9.6
0.5	2.8	6.2	14.4	11.2	8.0
1.5	2.8	6.2	14.4	11.2	8.0
2.5	2.8	6.2	14.4	11.2	8.0
3.5	0.0	6.2	14.4	11.2	8.0

Table 44: DC2-D3 absorption width [m]

7.3.1.8 Standard deviation of the nacelle acceleration matrix

The standard deviation of the nacelle acceleration is calculated through equation 100. The values for each sea state in the operational subset are presented here in g units. In this section only the values for the FOHWWECs are included. The matrices for the FOWTs can be found in Appendix A.

H_s/T_p	4.5	5.8	7.1	8.4	9.6
0.5	0.005	0.005	0.004	0.004	0.004
1.5	0.016	0.016	0.012	0.012	0.012
2.5	0.026	0.027	0.020	0.020	0.020
3.5	0.0	0.038	0.027	0.028	0.028

Table 45: DC2-D1 standard deviation of the nacelle acceleration [g]

H_s/T_p	4.5	5.8	7.1	8.4	9.6
0.5	0.005	0.006	0.004	0.004	0.004
1.5	0.016	0.017	0.012	0.013	0.013
2.5	0.027	0.028	0.020	0.021	0.022
3.5	0.0	0.039	0.028	0.029	0.031

Table 46: DC2-D2 standard deviation of the nacelle acceleration [g]

H_s/T_p	4.5	5.8	7.1	8.4	9.6
0.5	0.005	0.006	0.004	0.004	0.005
1.5	0.016	0.016	0.012	0.013	0.014
2.5	0.026	0.027	0.020	0.021	0.023
3.5	0.0	0.038	0.028	0.030	0.033

Table 47: DC2-D3 standard deviation of the nacelle acceleration [g]

The highlighted cells are the minimum value (blue) and maximum value (red). Both are important to define the standard deviation fluctuation.

7.3.2 Performance analysis

The performance analysis of DC2 starts with the performance plot. Nevertheless, before presenting this plot, it is necessary to explain why the $b_{PTO(opt)}$ values for $T_p = 5.8s$ sea states are equal or lower than the ones for $T_p = 7.1s$ sea states (see tables 37 and 38). As deduced from equation 87 the minimum value of b_{PTO} should be obtained for $T_p = 7.1s$, because the WEC is at resonance close to that peak frequency. Nevertheless, this is only true if the hydrodynamic coefficients are constant throughout the frequency range and this is not the case for DC2's hydrodynamic heave damping, as it can be seen in Figure 110. This is indeed what produces b_{PTO} values of 90.9tons/s and 60.6tons/s at sea states with $T_p = 5.8s$.

Figure 85 is the performance plot for DC2. The characteristics of this kind of plot have been already described in section 7.2.2.

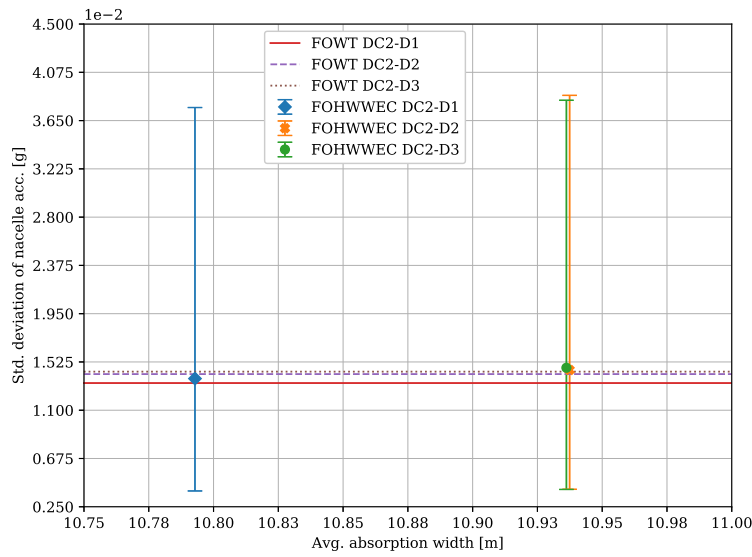


Figure 85: DC2 performance plot

These performance values are also included in Table 48.

Perf. variable	DC2-D1	DC2-D2	DC2-D3
$\lambda_{p(\text{avg})}$ [m]	10.79	10.94	10.94
$\sigma_{aN_a(\text{avg})}$ [g]	0.014	0.015	0.015

Table 48: Performance variable values of DC2 FOHWWE Cs

DC2-D2 and DC2-D3 has practically an equal $\lambda_{p(\text{avg})}$ value which is just 1% higher than DC2-D1's value. They also have the higher $\sigma_{aN_a(\text{avg})}$, 7.1% higher than DC2-D1's value. This indicates that the draft seems to have a limited impact on the performance variables.

Since the performance variables depend on the motion spectra (see equations 82 and 100), limited changes with varying draft are then expected in those spectra. In figures 73 and 74 there are indeed limited differences between the draft levels for the WEC's relative heave motion spectrum and for the nacelle acceleration spectrum (see zoomed-in plots). In both cases, the spectrum magnitudes help explaining the positions of each draft in the performance plot. Here it is important to mention that although DC2-D3 has slightly higher values of $\lambda_{p(\text{avg})}$ and $\sigma_{aN_a(\text{avg})}$, in comparison with DC2-D2, both are considered as having the same performance.

Once the relation between the motion spectra and the performance variables is demonstrated, it is necessary to analyze what is behind the variation of the spectra. This analysis is presented in the following sections.

7.3.2.1 The effect of draft and geometry

The first part of DC₁ analysis is also applicable for DC₂. That is, a lower heave resonance frequency and larger inertia for the deeper draft, allows a more independent motion of the WEC. Although, this explains why DC₂-D₂ and DC₂-D₃ absorbs more power in almost all peak periods than DC₂-D₁ (see tables 39, 40 and 41), it does not answer the following questions:

1. Why are DC₂ $\lambda_{p(\text{avg})}$ values higher than DC₁ values?
2. Why are DC₂ $\sigma_{aNa(\text{avg})}$ and $\sigma_{aNa(\text{max})}$ values lower than DC₁ values?

To answer the first question, specific aspects of DC₂ are highlighted. First, the CoG locates midway between the two cylinders. Then, when it pitches it induces the WECs to heave. Besides this, the WECs introduce the restoring coefficients C_{35} and C_{53} . All this is enhanced at pitch resonance ($\omega \approx 0.3$), explaining the peaks around the same frequency in figures 77 and 78.

Second, DC₂ FOHWWECs have higher pitch and heave natural frequencies than DC₁ FOHWWECs (see tables 23 and 36). This is due to higher hydrostatic restoring forces introduced by the addition of the B cylinder.

Third, DC₂'s WPA is expanded with the B cylinder. This is extra area over which the dynamic pressure is integrated to obtain a higher heave wave excitation load, in comparison with DC₁; at some frequencies more than five times larger, as shown in Figure 112.

All this produces an enhanced two-peaked WEC's relative heave RAO (see Figure 78). One peak is close to pitch resonance ($\omega \approx 0.3\text{rad/s}$) and the other is close to heave resonance ($\omega \approx 0.4\text{rad/s}$). The word "enhanced" means intensified by the heave wave excitation load. This produces greater WEC's relative heave RAO values than DC₁'s values, specially at the onset of WEC's heave resonance. This is clearly seen in Figure 108.

As a consequence, for sea states including frequencies at the onset of WEC's heave resonance (e.g. $T_p = 7.1\text{s}$, $T_p = 8.4\text{s}$ and $T_p = 9.6\text{s}$), and since the b_{PTO} values in those sea states are similar for DC₁ and DC₂, more power is absorbed by DC₂ FOHWWECs in comparison with DC₁ FOHWWECs.

To answer the second question, Figure 80 is the starting point. The first noticeable aspect are the fluctuations, that can be traced back to the pitch motion. Indeed, in Figure 79 the peaks at $\omega \approx 0.3\text{rad/s}$ and $\omega \approx 1.18\text{rad/s}$ are noticeable. The fluctuation at $\omega = 1.52\text{rad/s}$ is visible in Figure 77 and therefore it should be as well present in the pitch motion due to the heave-pitch coupling. All fluctuations above $\omega = 0.9\text{rad/s}$ are due to wave diffraction effects, further explained in section 7.3.2.3.

The second aspect to highlight is already detected and explained for DC1. It is the order inversion of the pitch RAO curves. In the case of DC2, only DC2-D2 and DC2-D3 participate in the inversion that occurs close to $\omega = 0.9\text{rad/s}$ (see Figure 79). DC2-D1 values remain in the lowest position, probably because the pitch wave excitation force is the lowest for DC2-D1 (see Figure 83). This order inversion reflects in figures 80 and 73 and it explains why DC2-D3 produces σ_{aN_a} values barely higher than DC2-D2 in sea states with a high T_p and DC2-D2 produces σ_{aN_a} values barely higher than DC2-D3 in sea states with low T_p (see tables 46 and 47). The net effect is that DC2-D3 produces a $\sigma_{aN_a(\text{avg})}$ value slightly higher than DC2-D2.

A third aspect in Figure 80 is that the curves descend after $\omega = 0.45\text{rad/s}$ instead of ascending as for DC1. This is due partly to the higher pitch resonance frequency of DC2. Explaining this further, the DC2 pitch RAO values between $\omega = 0.45\text{rad/s}$ and $\omega = 0.9\text{rad/s}$ decrease at a higher rate than for DC1, finally pushing the nacelle acceleration RAO values downwards. The other cause is the pitch motion being amplified by shorter h_{n_a} distances, in comparison with DC1.

These three aspects translate into a multiple-peaked nacelle acceleration spectra, but the area under those peaks is smaller than for DC1 (see Figures 73 and 60). This leads to lower values of σ_{aN_a} .

7.3.2.2 The effect of WEC addition

Figure 85 also includes the $\sigma_{aN_a(\text{avg})}$ for the FOWTs. Comparing these values with $\sigma_{aN_a(\text{avg})}$ for the FOHWWECs, the latter are slightly higher than the former ones for all draft levels.

To find the cause of this result, figures 79 and 81 are compared. Although it is difficult to directly see it, the pitch RAO values for the FOWTs are above the pitch RAO values for the FOHWWECs until $\omega \approx 1.13\text{rad/s}$. Between $\omega \approx 1.13\text{rad/s}$ and $\omega \approx 1.35\text{rad/s}$, the FOHWWEC values are greater. The order is dictated by the pitch wave excitation forces, as it can be seen in Figure 83 for DC2-D3 FOWT and FOHWWEC substructure. In this curve, the effect of WEC addition is palpable throughout the frequency range; for example at $\omega = 1.52\text{rad/s}$ there is one fluctuation that is not present in the FOWT curve. This is thought to be related to wave interactions where diffracted waves produced by the WECs are involved. This fluctuation enhances the FOHWWEC nacelle acceleration RAO (see Figure 80), the spectra and finally increase the gap between FOWT and FOHWWEC's $\sigma_{aN_a(\text{avg})}$ values.

On top of that, as explained for DC1, the WEC's pitch wave excitation forces are added to the FOHWWEC, while the FOWTs do not experience them, further enhancing the FOHWWEC's pitch motion and nacelle accel-

ation spectra. This force is plotted in Figure 84 for DC2-D3.

In summary, the presence of the WECs modifies the wave excitation forces on the substructure through diffraction effects and it adds additional pitch wave excitation loads because the substructure and WECs move together in pitch. Both effects bring the FOHWECs to higher nacelle acceleration amplitudes and $\sigma_{aN_{\alpha}(\text{avg})}$ values, in comparison with the FOWTs.

7.3.2.3 The effect of wave diffraction

The explanation of the effect of wave diffraction is very similar to the one presented for DC1. The difference this time is the additional wave interaction between the wave diffracted by the B cylinder and the one coming from the WT cylinder and WECs. According to the results obtained by Vasilikis [29], the fluctuations should be stronger for DC2, because the WECs and the WT cylinder are located on the shadow region. Indeed, looking at Figure 77 the fluctuations are more noticeable, and there are two of them, in comparison with DC1, where only one fluctuation is noticeable.

Going now to Figure 111 there are indeed more and stronger fluctuations on the DC2's wave excitation force in heave than on the DC1 curve. Their position also coincides with the fluctuations' positions on the WEC's heave RAO. There is one at $\omega \approx 1.18\text{rad/s}$ and a second one at $\omega \approx 1.52\text{rad/s}$. The one at $\omega \approx 1.85\text{rad/s}$ is almost not visible in Figure 77.

These fluctuations have an impact on the absorbed power, but since their amplitudes are larger, in comparison with DC1, the impact seems to be more localized and less uniform than the impact on DC1. The fluctuation peak "push" the RAO to higher values, as it can be seen in Figure 108. This effect translates to the relative heave spectra and finally to the λ_p values.

The fluctuations have also an important effect on the nacelle acceleration, as it has been identified in sections 7.3.2.1 and . Actually, they are the most influencing factor on the DC2's nacelle acceleration, at least for the first four peak frequencies in the operational subset. They determine the shape of the pitch wave excitation force, the pitch and nacelle acceleration RAOs and finally the nacelle acceleration spectra.

7.4 DC3 SIMULATION

As mentioned at the beginning of this chapter, the reader can skip the section 7.4.1, where the intermediate results are presented, and continue with the analysis in section 7.4.2. In this analysis, proper references are made to the required intermediate result.

7.4.1 Relevant intermediate results

7.4.1.1 Natural frequencies

In this section the natural frequencies values for each DOF of DC3 are presented. The values correspond to the wave frequency $\omega = 0.875\text{rad/s}$ which is the closest to the peak period $T_p = 7.1\text{s}$.

DOF/FOHWEC	DC3-D1	DC3-D2	DC3-D3
1	0.115	0.096	0.085
3	0.625	0.528	0.466
WEC3	0.963	0.951	0.942
5	0.337	0.323	0.318

Table 49: Natural frequencies of DC3 FOHWECs

7.4.1.2 Motion spectrum

This section includes the motion spectrum plots relevant for the analysis of the results of DC3. The data is taken from two sea states. First, the sea state $H_s = 1.5\text{m}, T_p = 7.1\text{s}$, named as *sea state 1* and used also in the previous simulations. Second, the sea state $H_s = 1.5\text{m}, T_p = 9.6\text{s}$, named as *sea state 2*. This additional sea state 2 is considered because DC3's results exhibit a particular trend for the sea states with $T_p = 9.6\text{s}$.

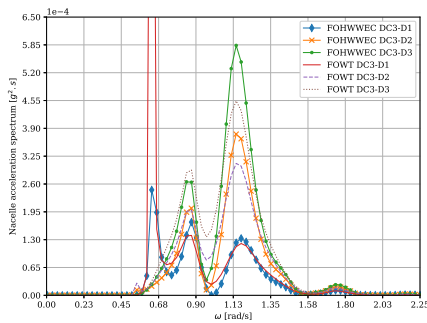


Figure 86: Nacelle acc. spectrum of DC3 FOHWECs. Sea state 1

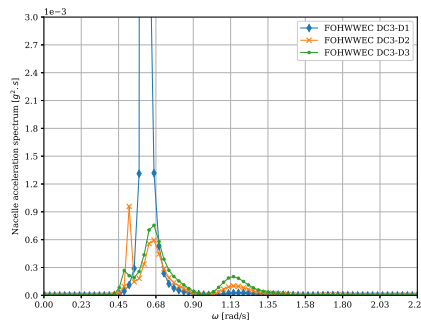


Figure 87: Nacelle acc. spectrum of DC3 FOHWECs. Sea state 1

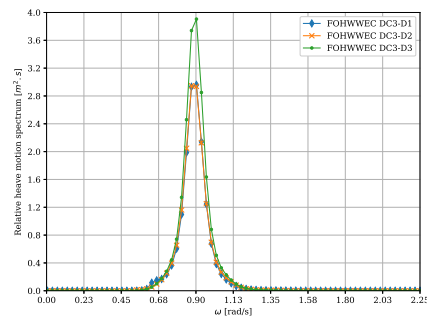


Figure 88: Rel. heave spect. of WEC on DC3. Sea state 1

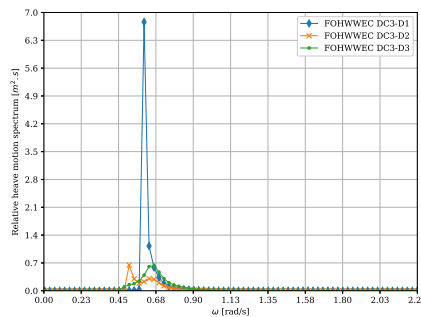


Figure 89: Rel. heave spect. of WEC on DC3. Sea state 2

7.4.1.3 Response amplitude operators (RAOs)

This section includes the RAO plots which are relevant for the analysis of the results. Two groups of plots are identified. The first group portrays the effect of draft variation for FOHWWECS. The second group presents the same, but for the FOWTs (without WECs).

As it is done for the spectra in the previous section, the RAO data is taken as well from sea state 1 and sea state 2.

GROUP 1: FOHWWEC RAOs for each draft level ($H_s = 1.5\text{m}$, $T_D = 7.1\text{s}$)

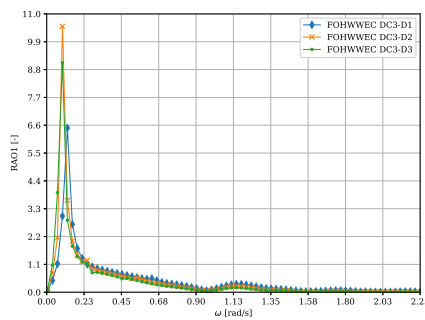


Figure 90: Surge RAO of DC3 FOHWWECS. Sea state 1

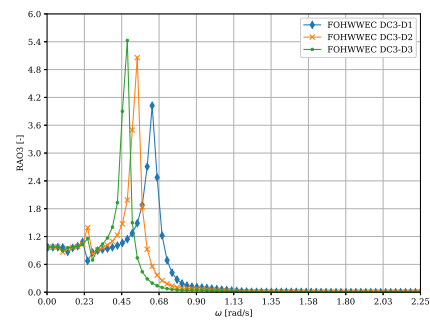


Figure 91: Heave RAO of DC3 FOHWWECS. Sea state 1

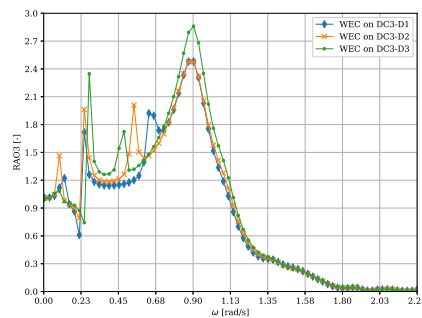


Figure 92: Heave RAO of WEC on DC3 FOHWWECS. Sea state 1

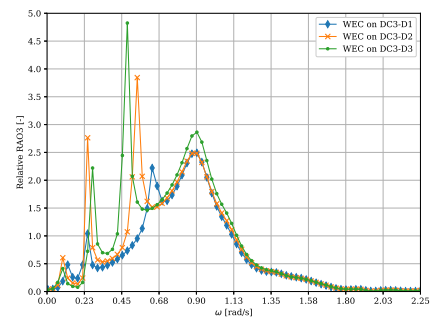


Figure 93: Rel. heave RAO of WEC on DC3 FOHWWECS. Sea state 1

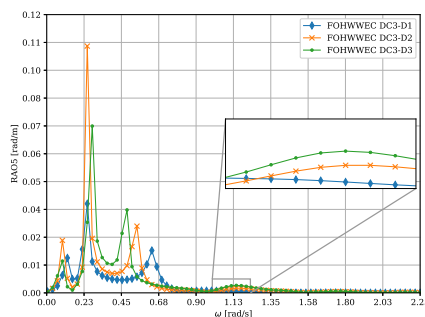


Figure 94: Pitch RAO of DC3 FOHWWECS. Sea state 1

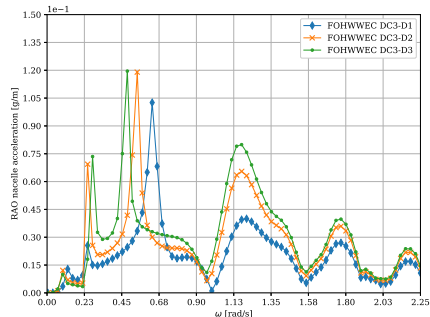


Figure 95: Nacelle acc. RAO of DC3 FOHWWECS. Sea state 1

GROUP 1: FOHWWECC RAOs for each draft level ($H_s = 1.5\text{m}, T_p = 9.6\text{s}$)

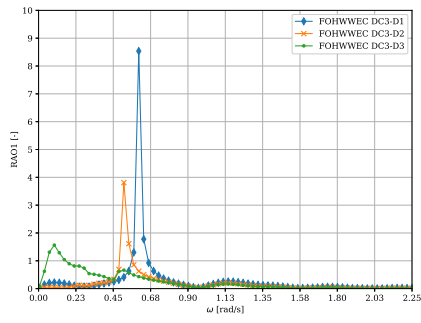


Figure 96: Surge RAO of DC3 FOHWWECCs. Sea state 2

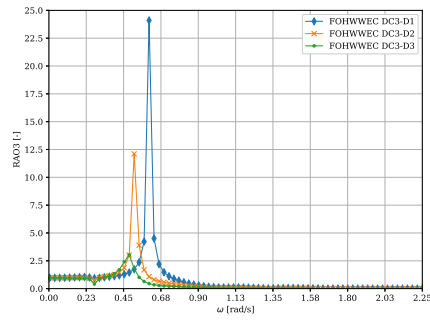


Figure 97: Heave RAO of DC3 FOHWWECCs. Sea state 2

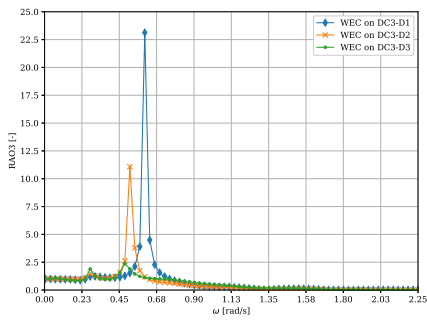


Figure 98: Heave RAO of WEC on DC3 FOHWWECCs. Sea state 2

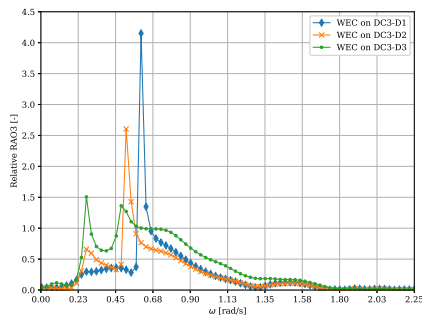


Figure 99: Rel. heave RAO of WEC on DC3 FOHWWECCs. Sea state 2

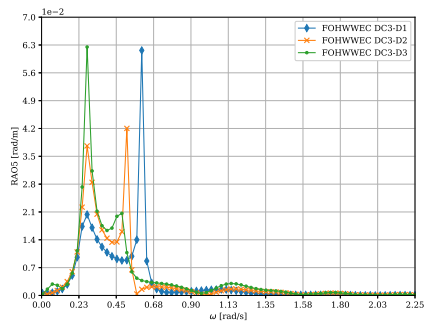


Figure 100: Pitch RAO of DC3 FOHWWECCs. Sea state 2

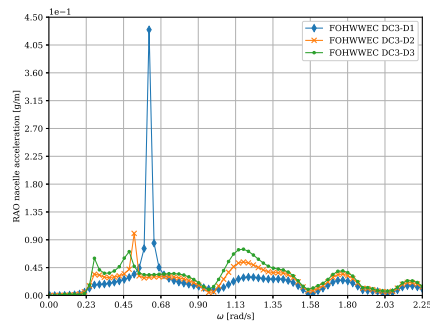


Figure 101: Nacelle acc. RAO of DC3 FOHWWECCs. Sea state 2

GROUP 1: FOWT RAOs for each draft level ($H_s = 1.5\text{m}, T_p = 7.1\text{s}$)

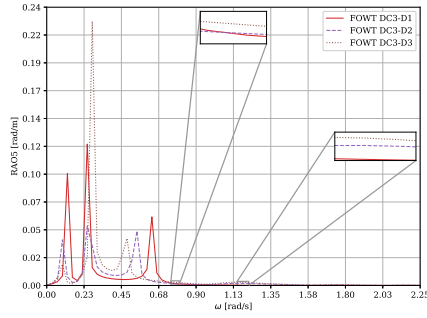


Figure 102: Pitch RAO of DC₃ FOWTs.
Sea state 1

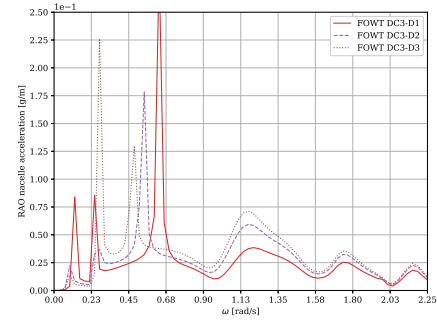


Figure 103: Nacelle acc. RAO of DC₃ FOWTs. Sea state 1

7.4.1.4 Wave excitation forces

This section includes the wave excitation force plots which are relevant for the analysis of the results of DC₃.

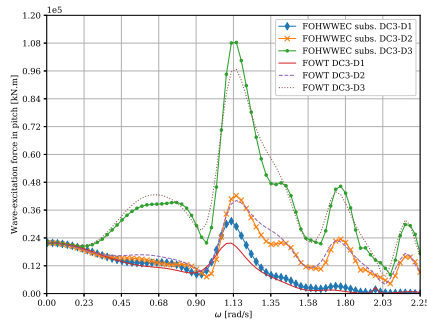


Figure 104: Pitch wave excitation force
on DC₃ subs. and FOWT

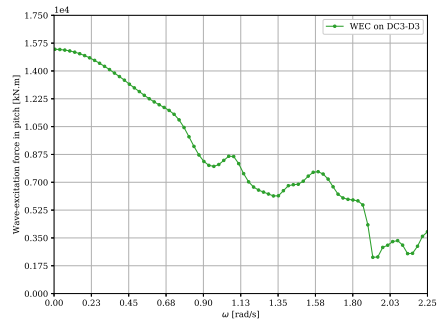


Figure 105: Pitch wave excitation force
on DC₃-D₃ WEC

7.4.1.5 Optimized PTO damping matrix

The PTO damping coefficient (b_{PTO}) is optimized for each sea state in the operational range, following the procedure described in section 5.10.1. In the present section, the results are presented in matrix form.

H_s/T_p	4.5	5.8	7.1	8.4	9.6
0.5	484.8	181.8	121.2	1333.3	1333.3
1.5	484.8	181.8	121.2	1333.3	1333.3
2.5	484.8	181.8	121.2	1333.3	1333.3
3.5	484.8	181.8	121.2	1333.3	1333.3

Table 50: DC₃-D₁ optimal PTO damping coefficient [tons/s]

H_s/T_p	4.5	5.8	7.1	8.4	9.6
0.5	454.5	212.1	121.2	575.8	1575.8
1.5	454.5	212.1	121.2	575.8	1575.8
2.5	454.5	212.1	121.2	575.8	1575.8
3.5	454.5	212.1	121.2	575.8	1575.8

Table 51: DC3-D2 optimal PTO damping coefficient [tons/s]

H_s/T_p	4.5	5.8	7.1	8.4	9.6
0.5	484.8	212.1	90.9	484.8	757.6
1.5	484.8	212.1	90.9	484.8	757.6
2.5	484.8	212.1	90.9	484.8	757.6
3.5	484.8	212.1	90.9	484.8	757.6

Table 52: DC3-D3 optimal PTO damping coefficient [tons/s]

7.4.1.6 Absorbed power and energy matrices

Once the PTO damping is established and optimized, the absorbed power can be calculated for each sea state in the operational range, using equation 82. The results are presented in matrix form in tables 53, 54 and 55.

Then, each of the values in the absorbed power matrices is multiplied by the amount of hours per year corresponding to the applicable sea state, to obtain the absorbed energy matrices. These matrices are included in Appendix A.

H_s/T_p	4.5	5.8	7.1	8.4	9.6
0.5	1.1	5.4	10.3	14.4	33.0
1.5	10.3	48.3	92.7	129.7	297.4
2.5	28.6	134.2	257.4	360.3	826.1
3.5	0.0	263.0	504.5	706.1	1619.2

Table 53: DC3-D1 absorbed power per sea state [kW]

H_s/T_p	4.5	5.8	7.1	8.4	9.6
0.5	1.3	5.8	10.5	10.5	10.6
1.5	12.0	52.6	94.5	94.7	95.3
2.5	33.3	146.1	262.6	263.0	264.7
3.5	0.0	286.3	514.7	515.4	518.9

Table 54: DC3-D2 absorbed power per year [kW]

H_s/T_p	4.5	5.8	7.1	8.4	9.6
0.5	1.4	6.1	9.9	10.3	9.2
1.5	12.9	54.8	89.4	93.0	82.7
2.5	35.9	152.2	248.2	258.3	229.8
3.5	0.0	298.4	486.6	506.3	450.3

Table 55: DC3-D3 absorbed power per year [kW]

7.4.1.7 Absorption width matrix

The absorption width (λ_p) is calculated through equation 92, using the absorbed power and the available power matrices. The values for each sea state in the operational subset are presented here in meters.

It is important to notice that since both WECs are considered, a 100% efficiency is equal to an absorption width of 20m (two WECs of 10m diameter).

H_s/T_p	4.5	5.8	7.1	8.4	9.6	H_s/T_p	4.5	5.8	7.1	8.4	9.6
0.5	2.4	8.5	13.2	15.6	30.9	0.5	2.8	9.3	13.5	11.4	9.9
1.5	2.4	8.5	13.2	15.6	30.9	1.5	2.8	9.3	13.5	11.4	9.9
2.5	2.4	8.5	13.2	15.6	30.9	2.5	2.8	9.3	13.5	11.4	9.9
3.5	0.0	8.5	13.2	15.6	30.9	3.5	0.0	9.3	13.5	11.4	9.9

Table 56: DC3-D1 absorption width [m] Table 57: DC3-D2 absorption width [m]

H_s/T_p	4.5	5.8	7.1	8.4	9.6
0.5	3.1	9.7	12.7	11.2	8.6
1.5	3.1	9.7	12.7	11.2	8.6
2.5	3.1	9.7	12.7	11.2	8.6
3.5	0.0	9.7	12.7	11.2	8.6

Table 58: DC3-D3 absorption width [m]

7.4.1.8 Standard deviation of the nacelle acceleration matrix

The standard deviation of the nacelle acceleration is calculated through equation 100. The values for each sea state in the operational subset are presented here in g units. In this section only the values for the FOHWECs are included. The matrices for the FOWTs can be found in Appendix A.

H_s/T_p	4.5	5.8	7.1	8.4	9.6
0.5	0.003	0.003	0.003	0.009	0.017
1.5	0.008	0.009	0.009	0.025	0.049
2.5	0.014	0.015	0.014	0.042	0.082
3.5	0.0	0.021	0.020	0.059	0.115

Table 59: DC3-D1 standard deviation of the nacelle acceleration [g]

H_s/T_p	4.5	5.8	7.1	8.4	9.6
0.5	0.004	0.005	0.004	0.004	0.004
1.5	0.012	0.015	0.011	0.012	0.012
2.5	0.020	0.025	0.018	0.019	0.020
3.5	0.0	0.035	0.026	0.027	0.029

Table 60: DC3-D2 standard deviation of the nacelle acceleration [g]

H_s/T_p	4.5	5.8	7.1	8.4	9.6
0.5	0.005	0.006	0.004	0.005	0.005
1.5	0.014	0.019	0.013	0.014	0.014
2.5	0.024	0.031	0.022	0.023	0.023
3.5	0.0	0.044	0.031	0.032	0.032

Table 61: DC3-D3 standard deviation of the nacelle acceleration [g]

The highlighted cells are the minimum value (blue) and maximum value (red). Both are important to define the standard deviation fluctuation.

7.4.2 Performance analysis

The performance analysis of DC3 starts with the performance plot. Nevertheless, before presenting this plot, it is necessary to highlight particular aspects in the intermediate results. First, the DC3-D1 and DC3-D2's $b_{PTO(opt)}$ matrices have particularly high values for sea states with $T_p = 8.4s$ and $T_p = 9.6s$, in comparison with the values for the other sea states and the values for the other DCs (see tables 50, 51). Second, in the DC3-D1 and DC3-D2's absorbed power matrices the maximum values are at $T_p = 8.4s$ and $T_p = 9.6s$, instead of at $T_p = 7.1s$, as it is the case for the other DCs (see tables 53 and 54). For DC3-D3, the maximum values are at $T_p = 8.4s$ (see Table 55).

Both aspects indicate that there is a different power absorption mechanism for DC3, that is not based just on the WEC's resonance. Such mechanism is taking advantage of the high peak period spectra, which have low frequency wave components. Additionally, judging by the absorption width values in

Table 56, the novel mechanism results even more efficient than the WEC's resonance mechanism for DC3-D1; higher λ_p values are obtained at $T_p = 8.4s$ and $T_p = 9.6s$, in comparison with the values at $T_p = 7.1s$. This new mechanism is further described in the present section.

Figure 106 is the performance plot for DC3. The characteristics of this kind of plot have been already described in section 7.2.2.

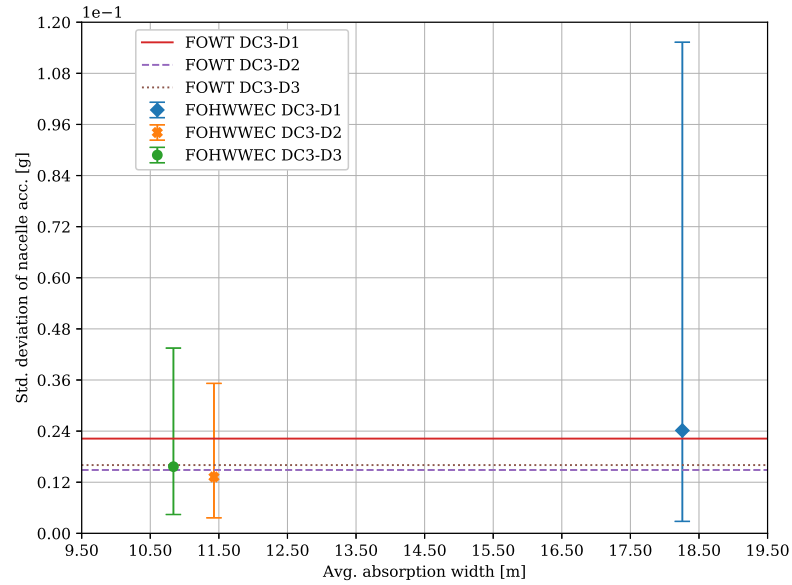


Figure 106: DC3 performance plot

These performance values are also included in Table 62.

Perf. variable	DC2-D1	DC2-D2	DC2-D3
$\lambda_{p(avg)}$ [m]	18.26	11.43	10.84
$\sigma_{aN_a(avg)}$ [g]	0.024	0.013	0.016

Table 62: Performance variable values of DC3 FOHWWEs

DC3-D1 has the higher $\lambda_{p(avg)}$, 60% higher than DC3-D2 value and 70% higher than DC3-D3 value. It also has the higher $\sigma_{aN_a(avg)}$, 50% higher than DC3-D3 and 85% higher than DC3-D2 values. This indicates that the draft seems to have a considerable impact on both, $\sigma_{aN_a(avg)}$ and $\lambda_{p(avg)}$.

Since the performance variables depend on the motion spectra (see equations 82 and 100), considerable changes with varying draft are then expected for both variables. In Figure 86 there are indeed considerable differences and based on the magnitude of the spectrum, the draft levels can be ordered as $D3 > D2 > D1$. In Figure 87 the differences are also considerable, specially

for DC3-D1 that exhibits a large peak around $\omega = 0.63\text{rad/s}$, and the order is rearranged to $D1 > D3 > D2$. The former order sequence is the same for the first three peak periods. The latter one repeats for the last two peak periods ($T_p = 8.4\text{s}$ and $T_p = 9.6\text{s}$). The combination of the two order sequences produces the arrangement of $\sigma_{aNa(\text{avg})}$ values in Figure 106.

In plot 74 the difference in the magnitude of the spectrum between DC3-D3 and the other two draft levels is considerable, but it is due to the lower b_{PTO} value of DC3-D3. The actual differences in magnitude manifest for sea state 2, in Figure 89, where DC3-D1 holds the greater values. This, coupled with a high b_{PTO} value of 1333.3tons/s, produces the highest λ_{dp} values. DC3-D2 and DC3-D3 seem to have similar spectrum magnitudes, but DC3-D2 has the greatest b_{PTO} value, leaving it in middle position regarding λ_{dp} values (see tables 56, 57 and 58). In this way, the positions of the performance points, regarding absorption width, is explained.

Once the relation between the motion spectra and the performance variables is demonstrated, it is necessary to analyze what is behind the variation of the spectra. This analysis is presented in the following sections.

7.4.2.1 The effect of draft and geometry

The analysis performed in this section should provide an answer to the following three questions:

1. Why is DC3-D1's performance point is remarkably different, in comparison with all the other performance points?
2. Why DC3-D1 and DC3-D2 are absorbing more power than DC2-D1 and DC2-D2?
3. Why DC3-D2 provides the lowest $\sigma_{aNa(\text{avg})}$ of all DCs?

In an attempt to answer the second question, the most important geometry-related differences between DC3 and DC2 are enumerated.

1. As for DC2, the WECs on DC3 introduce the coupling restoring coefficients C_{35} and C_{53} , but in DC3 these are partly counteracted by the restoring forces coming from the additional B cylinder.
2. The DC3's heave resonance frequencies are higher than for DC2. This is because, on the one hand, DC3's restoring force in heave is greater than for DC2, due to the additional cylinder. On the other hand, DC3 displacements are lower than DC2.
3. DC3 experiences larger heave wave excitation loads on the substructure, in comparison with DC2 (see Figure 112). This is due to the further expansion of the WPA with an additional B cylinder.

4. DC₃ heave resonance manifests in its pitch RAO, in contrast to DC₂, where no heave resonance peak is visible in its pitch RAO. This is due to the lower moment of inertia of DC₃ FOHWWECs, that lowers its resistance to the coupled heave-pitch motions.

Now, DC₃ FOHWWECs are absorbing more power than DC₂ FOHWWECs mainly at the sea states with high peak frequency ($T_p = 8.4s$ and $T_p = 9.6s$). The root cause are actually the DC₃'s high heave resonance frequencies mentioned above. These heave resonance peaks manifest in the WEC's relative heave RAO (see Figure 99) and all of them are above $\omega = 0.45\text{rad/s}$, in contrast to the DC₂ case, where all heave resonance peaks are below $\omega = 0.45\text{rad/s}$ (see Figure 78). In consequence, DC₃'s heave resonance peaks are captured by the high peak period wave spectra and transferred to the relative heave spectra (see Figure 89), finally enhancing the power absorption. Besides this, in Figure 99 no WEC's heave resonance around $\omega = 0.9\text{rad/s}$ is visible. This is due to the high b_{PTO} values that completely damp the WEC's resonance peak.

The previous paragraph describes the DC₃ novel power absorption mechanism. It is based on the substructure's heave resonance at low wave frequencies. Since the heave wave excitation forces involved are those applied on the substructure, they are much higher than the ones applied on the WECs (see figures 112 and 111). This allows for much greater values of b_{PTO} , in comparison with the other DCs, finally leading to greater power absorption and greater efficiency values that can not be matched by the mechanism based on the WEC's resonance.

Besides this, DC₃ substructure has a higher heave hydrodynamic damping than DC₂ substructure, due to the presence of the additional B cylinder that radiates additional waves. This is clearly shown in Figure 109 and it indicates that, compared to DC₂, DC₃ is a more stable option to absorb power with the mechanism based on the substructure's heave resonance.

Although the novel mechanism seems promising, it is important to point out that a power absorption based on the heave resonance of the substructure is probably not a convenient idea in reality. It might lead to extremely large heave and pitch motion amplitudes as. It might as well negatively impact the wind power generation and ultimately lead to damage in the equipment. It should be part then of a future investigation to figure out if this is a workable condition or not.

The answer to the first question can be deduced from the previous mechanism explanation. The DC₃-D1 substructure has the highest heave resonance frequency and therefore it is effectively captured by both high peak period spectra, at $T_p = 8.4s$ and at $T_p = 9.6s$.

To answer the third question, the analysis moves on to the effect of draft and geometry on the nacelle acceleration spectra, figures 95 and 101 are used as starting point. These curves have multiple resonance peaks and, as already learnt from DC1 and DC2 analyses, those fluctuations are to be traced back to the pitch motion. Indeed, in Figures 94 and 100 the majority of the peaks are visible.

In both plots, DC3-D3 holds the greater RAO values almost throughout the frequency range. As learnt from DC1 and DC2, this dominance is dictated by the pitch wave excitation forces, where DC3-D3 has the highest values (see Figure 104). Then this dominance is enhanced by the h_{na} distance that amplifies the pitch RAO. Nevertheless, in Figure 101 DC3-D1 curve presents a large resonance peak at $\omega = 0.63\text{rad/s}$ that transfers to the nacelle acceleration spectrum and produces largest σ_{aN_a} values than the other two drafts for $T_p = 9.6\text{s}$. The same occurs as well for DC3-D1 at sea states with $T_p = 8.4\text{s}$. The net result is DC3-D1 holding the maximum $\sigma_{aN_a(\text{avg})}$ in the performance plot, followed by DC3-D3, whose σ_{aN_a} values dominate for the first three peak periods in the operational subset.

Comparing DC3 and DC2 nacelle acceleration RAOs, some differences are found. For DC3 the curves for each draft are further separated from each other. This has two reasons; first, larger differences on the area on which pressure is integrated, due to the extra B cylinder, lead to further separated pitch wave excitation forces for each draft level, as it can be seen from comparing figures 83 and 104. Second reason is that the h_{na} distance increment from draft to draft is larger for DC3 than for DC2. This introduces more variability into the spectra and it allows the performance points to be more spread out in the performance plot.

Another difference is that DC3 nacelle acceleration RAOs include the heave resonance peaks, for both sea states in study, while those peaks do not manifest in DC2's nacelle acceleration RAO. The consequence are DC3 $\sigma_{aN_a(\text{avg})}$ values similar or higher to DC2 values. In spite of this, DC3-D2 is the top performer regarding nacelle acceleration. The reason behind this result are the lower pitch wave excitation forces and lower h_{na} , in comparison with DC2 values.

7.4.2.2 The effect of WEC addition

Figure 106 also includes the $\sigma_{aN_a(\text{avg})}$ for the FOWTs. Comparing these values with $\sigma_{aN_a(\text{avg})}$ for the FOHWWECs leads to an interesting finding. The DC3-D2 and DC3-D3 $\sigma_{aN_a(\text{avg})}$ value are actually below their corresponding FOWT values by about 12% for DC3-D2 and 2.5% for DC3-D3. These are the first FOHWWECs in study that generates a lower $\sigma_{aN_a(\text{avg})}$ than its FOWTs counterpart.

In consequence, it is not necessary to find out why FOWT's $\sigma_{aNa(avg)}$ values are lower than FOHWWECS' values. This is already discussed for DC1 and DC2. The question is why the FOHWWECS' value is lower than the FOWT's value. To answer this, figures 103 and 95 are compared. It can be noticed that all heave resonance peaks for the FOWTs have a larger amplitude than the same peaks for the FOHWWECS. Then, it is deduced that the WEC and its PTO should be supplying additional heave damping into the system. To verify this, the plot in Figure 107 is prepared. It portrays the heave RAO for FOHWWECS and FOWTs. Indeed, the amplitudes are shorter for the FOHWWECS, specially for DC3-D2.

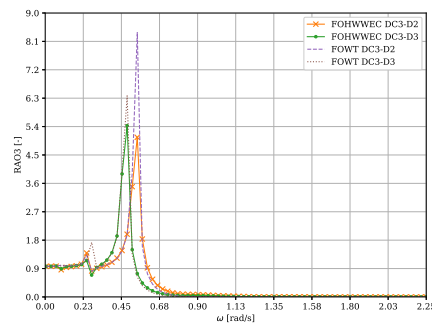


Figure 107: Heave RAO of DC3-D2 and DC3-D3 FOHWWECS and FOWTs

Besides this, and contributing to the result, the pitch wave excitation forces on DC3-D3 and DC3-D2 FOHWWECS are similar to the ones on their FOWTs counterparts as it can be seen in Figure 104. That means the wave diffraction effects are similar for both, FOHWWECS and FOWTs.

The shorter heave resonance amplitudes are making the difference with respect to the FOWTs specially at high peak periods, where the wave spectra captures them. This difference is appearing only for DC3 FOHWWECS because the heave-pitch coupled motion is more apparent than for DC2.

7.4.2.3 The effect of wave diffraction

The explanation of the effect of wave diffraction is very similar to the one given in section 7.3.2.3 for DC2. The difference this time is that there are additional wave interaction effects due to the presence of an extra B cylinder. Indeed, looking at the wave excitation force in heave in Figure 111 there are more fluctuations for DC3 curve than for DC2 and for certain frequencies they are stronger, for example for frequencies between $\omega = 1.35\text{rad/s}$ and $\omega = 1.90\text{rad/s}$. The position of the fluctuations also coincides with the fluctuations obtained from $\omega = 0.9\text{rad/s}$ onwards in Figure 95.

These fluctuations have a small impact on the power absorbed because as it can be seen in Figure 108 the RAO values are pushed to lower or higher values at the fluctuation's frequencies, getting farther or closer and even surpassing the WEC relative heave RAO values of DC1. These effects translate

to the relative heave spectra and finally to the absorption widths.

The fluctuations also have an important effect on the nacelle acceleration. They are one of the most important contributing factors in the construction of the DC₃ nacelle acceleration spectra, but their relative importance is less than for DC₂. In other words, the DC₃ nacelle acceleration is a product of the combination of heave resonance peaks that are actually reflected in the pitch RAO and wave diffraction effects. In contrast, the DC₂ nacelle acceleration is a product of pure pitch motion amplitudes and wave diffraction effects.

7.5 COMBINED RESULTS

As mentioned at the beginning of this chapter, the reader can skip the section 7.5.1, where the intermediate results are presented, and continue with the analysis in section 7.5.2. In this analysis, proper references are made to the required intermediate result.

7.5.1 Relevant intermediate results

7.5.1.1 Response amplitude operators (RAOs)

The present section includes plots with RAO curves of different design configurations. These plots support a combined analysis of the results, but also the analysis of each design configuration.

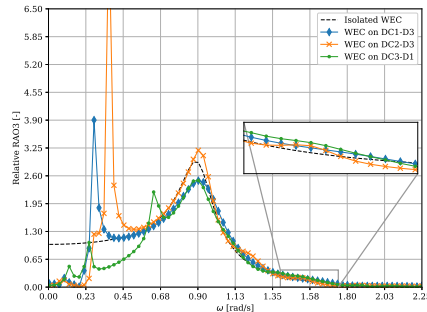


Figure 108: WEC wave-excitation force in heave. All DCs

7.5.1.2 Hydrodynamic coefficients and wave excitation forces

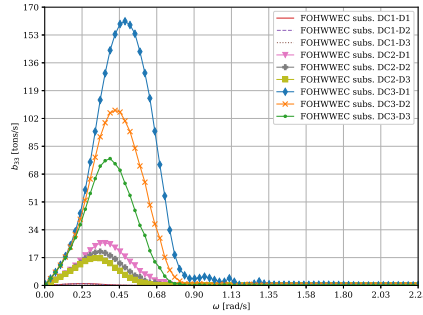


Figure 109: Damping coeff. b_{33}^{CC} .
Combined plot

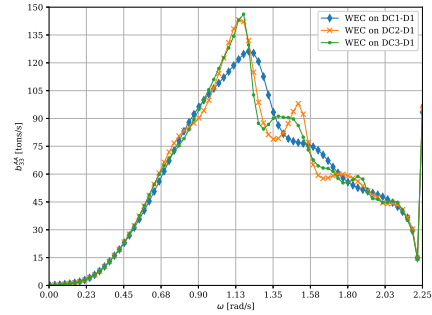


Figure 110: Damping coeff. b_{33}^{AA} .
Combined plot

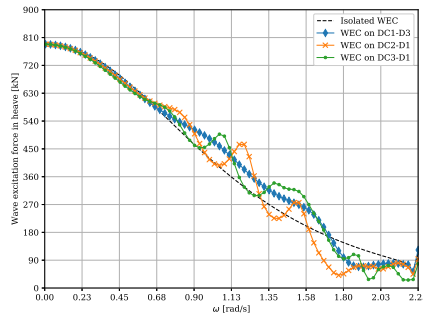


Figure 111: Heave wave excitation force on WEC. Combined plot

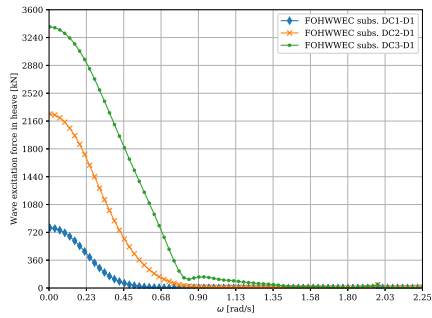


Figure 112: Heave wave excitation force on substructure. Combined plot

Notice that in hydrodynamic coefficient plots the superscript “AA” corresponds to the WEC on the positive y axis and “CC” corresponds to the substructure. The meaning of these superscripts can be found in the symbols list.

7.5.2 Performance analysis

The analysis in the previous sections allows to understand in detail the physics behind the results. Based on that understanding, a broader perspective is assumed in this section to assess the position of each DC in the design space and with respect to the other DCs. To complete this assessment means to accomplish the main objective of the present work.

Figure 113 is the combined performance plot. As in the other performance plots, the $\lambda_{p(avg)}$ values are in the x axis, but in this case the $\sigma_{aN\alpha(max)}$ values are in the y axis. The maximum standard deviations of the nacelle acceleration are more relevant than the averages when comparing the DCs.

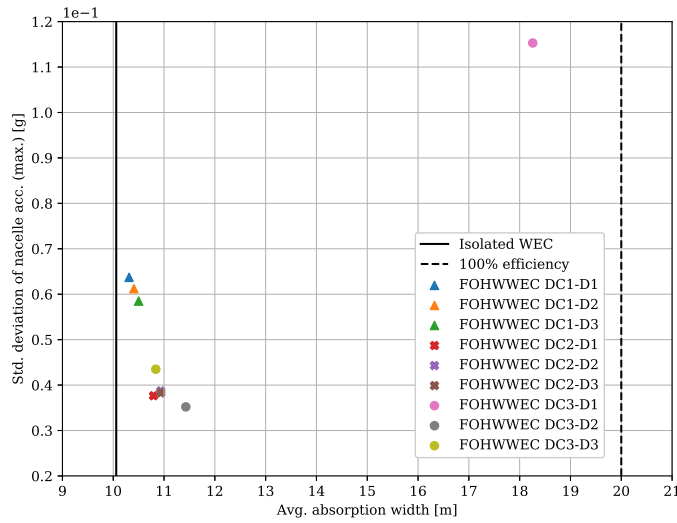


Figure 113: Combined performance plot

From this plot it is clear that DC3 is the design configuration offering maximum $\lambda_{p(\text{avg})}$ values and minimum $\sigma_{aN_{a(\text{max})}}$ values. The second place in performance is for DC2 FOHWWECs, the third place is for DC1 FOHWWECs and in the last place, from the power absorption perspective, appears the isolated WEC. This is a qualitative assessment. In order to have a quantitative assessment and to weigh the effect of the draft, all performance points are compared to the lowest $\lambda_{p(\text{avg})}$ (DC1-D1) and to the greater $\sigma_{aN_{a(\text{max})}}$ (DC3-D1), to obtain a percentage of improvement for each of the performance variables. The results of this action, including the root causes of the phenomenon, are included in tables 63 and 64. The arrows indicate the direction of the improvement and the encircled numbers refer to either the root causes per column or per row.

	Root cause			Root cause
	①	①	②	
D level/DC	DC1	DC2	DC3	
D1	0.0 ↓ →	4.7 ↓ →	77.1 ↑	③ and ④
D2	1.0 ↓ →	6.0 →	10.8 ↑	③ and ④
D3	1.8 →	6.0 ←	5.0	③ and ⑤

Table 63: Draft effect on $\lambda_{p(\text{avg})}$, as % of increase

The root causes related to $\lambda_{p(\text{avg})}$ are described as follows:

- ① = The increasing displacement produces a lower substructure's heave resonance frequency and a higher inertia. This allows the WEC to move more independently, maximizing the WEC's relative heave RAO. This is called the WEC's heave resonance mechanism.
- ② = The decreasing displacement produces a higher substructure's heave resonance frequency. This sets the substructure's heave resonance peak closer to the wave spectrum peak of the sea states with $T_p = 8.4s$ and $T_p = 9.6s$, enhancing the WEC's relative heave motion spectrum. This is called the substructure's heave resonance mechanism.
- ③ = This explains the performance improvement from DC1 to DC2: First, the CoG position enhances the heave-pitch coupled motion. Second, the increment of the WPA produces higher heave wave excitation loads. Third, the WPA expansion leads to higher restoring forces that produce higher substructure's pitch and heave resonance frequencies. All three aspects leads to an enhanced WEC's relative heave RAO, specially at the onset of WEC's resonance, that is captured by the high peak period sea states ($T_p = 7.1s$, $T_p = 8.4s$ and $T_p = 9.6s$).
- ④ = This explains the performance improvement from DC2 to DC3, for draft levels D1 and D2: The increment of the WPA produces higher heave restoring forces, leading to a higher substructure's heave resonance frequency. This sets the substructure's heave resonance peak closer to the wave spectrum peak of the sea states with $T_p = 8.4s$ and $T_p = 9.6s$, enhancing the WEC's relative heave motion spectrum. Additionally, the higher heave wave excitation load on the substructure, in comparison with the load on the WEC, allow for higher b_{PTO} values. This further enhances power absorption.
- ⑤ = This explains the performance decline from DC2-D3 to DC3-D3: In comparison with the other two drafts, DC3-D3 has the worst performance based on the substructure's heave resonance mechanism (②) due to its lower substructure's heave resonance frequency. It neither takes advantage of the WEC's heave resonance mechanism (①), due to its higher substructure's heave resonance frequency and lower inertia, in comparison with DC2.

D level/DC	Root cause			Root cause
	①	②	③ and ④	
D1	44.3 ↓ →	67.8 ↑ ←	0.0 ↓	⑤ and ⑥
D2	47.0 ↓ →	67.0 →	69.6 ↑	⑤ and ⑥
D3	49.6 →	67.0 ←	61.7	⑤ and ⑥

Table 64: Draft effect on $\sigma_{aN_{a(max)}}$, as % of decrease

The root causes related to $\sigma_{aN_{a(max)}}$ are described as follows:

- ① = On the one hand, the increasing draft and displacement produces a higher moment of inertia. On the other hand, the same increasing draft and displacement does not produce a major difference in the pitch wave excitation loads. Both effects produce an inversion of the order (from higher amplitudes to lower) of the pitch RAO curves from $D3 > D2 > D1$ to $D1 > D2 > D3$ at a low wave frequency ($\omega \approx 0.45\text{rad/s}$). The wave spectra captures only the latter order, transferring it to the nacelle acceleration spectrum.
- ② = On the one hand, the increasing draft and displacement produces a higher moment of inertia. On the other hand, the same increasing draft and displacement does produce major differences in the pitch wave excitation loads, because the area on which the pressure is integrated considerably increases due to the presence of the additional B cylinder. Both effects produce a partial inversion of the order (from higher amplitudes to lower) of the pitch RAO curves from $D3 > D2 > D1$ to $D2 > D3 > D1$ at a higher frequency ($\omega \approx 0.90\text{rad/s}$), in comparison with DC1. In consequence, the wave spectra captures both orders, but the order $D3 > D2 > D1$ prevails in the sea states with high peak period, leading to slightly lower $\sigma_{aNa(\max)}$ for D1 level.
- ③ = This explains the performance improvement from DC3-D3 to DC3-D2: The same root cause ② is enhanced because the surface area on which the pressure is integrated have a stronger increment, in comparison with DC2, due to the presence of the additional B cylinder.
- ④ = This explains the performance decline from DC3-D2 to DC3-D1: The DC3 with the lowest draft and displacement has the highest substructure's heave resonance frequency. This is positive for power absorption, but negative for the nacelle acceleration because the substructure's heave resonance peak manifests in the pitch RAO and in the nacelle acceleration RAO at a frequency that is closer to the spectrum peak frequency of the sea states with high peak period ($T_p = 8.4\text{s}$ and $T_p = 9.6\text{s}$). This maximizes the σ_{aNa} values for those sea states.
- ⑤ = This explains the performance improvement from DC1 to DC2: First, DC2 shorter drafts leads to lower pitch wave excitation loads and therefore lower pitch RAO values. Second, DC2 shorter drafts translates into lower h_{na} values that produce a less stronger amplification of the nacelle acceleration RAOs. Third, DC2 higher pitch natural frequencies "push" the nacelle acceleration RAO downwards, instead of upwards as for DC1. Fourth, stronger wave diffraction effects on DC2 leads to a fluctuating pitch wave excitation force nacelle acceleration RAO. All this aspects contribute to produce an overall lower nacelle acceleration spectra for DC2 and therefore lower σ_{aNa} values.
- ⑥ = This explains the performance improvement and decline from DC2 to DC3: The root cause ③ makes the order $D3 > D2 > D1$ to prevail regarding nacelle acceleration RAO values. The root cause ④ makes the order $D1 > D2 > D3$ to prevail regarding the impact of the substructure's heave resonance peak on the nacelle acceleration spectrum. This combines with the root cause ⑤, but applied to DC2 and DC3, to produce performance improvement from DC2-D2 to DC3-D2, but performance decline for the other two draft levels.

CONCLUSIONS AND RECOMMENDATIONS

In the previous chapter, the performance results of the four simulations have been analyzed. The isolated WEC simulation has been performed for two spherical point absorber type WECs, allowed only to heave without hydrodynamic interaction between them or with a substructure. The other three design configuration simulations have been performed for three FOHWWECs, differing on their floating stability principle (ballast-stabilized, ballast-buoyancy-stabilized and buoyancy-stabilized). Each FOHWWEC consists of a floating substructure supporting a WT with two spherical PA type WECs attached to it through a PTO system. The isolated WECs and the FOHWWECs has been subjected to 0 deg waves, no aerodynamic loads have been considered and only passive loading control of the PTO is used. The coupled motion equations have been solved in the frequency domain and the hydrodynamic coefficients have been obtained from the BEM solver NEMOH.

Regarding the wave data, a scatter diagram of the North Sea region has been employed and an operational subset encompassing the 80% of the sea state occurrences has been defined. A JONSWAP spectrum definition has been used for each sea state.

The previous paragraphs serve as a brief statement of the most important conditions considered in the study. They represent the framework within which the conclusions are built.

Two kind of conclusions are included in this chapter. The first kind results from the direct evaluation of the objectives of the present research. They are called *Objective related conclusions*. The second kind results from focusing on the physics explaining the performance results, that have been analyzed in the previous chapter. From the physical phenomena, wide-ranging conclusions are obtained, which have a more tangible impact on the FOHWWEC design space and industry. They are called *Wide-ranging conclusions*.

8.1 OBJECTIVE RELATED CONCLUSIONS

1. It is advantageous to select the design configuration 3 (DC₃) over the other two configurations to maximize the annual average absorption width. In particular, the DC₃ FOHWWEC with the shallower draft produces the maximum value. This value is about 74% higher than the maximum value produced by DC₁ FOHWWECs and 67% higher than the maximum value produced by DC₂ FOHWWECs.

2. It is advantageous to select the design configuration 3 (DC₃) over the other two configurations to minimize the standard deviation of the nacelle acceleration. In particular, the DC₃ FOHWWECS with the middle-level draft produces the minimum value. This value is about 40% lower than the minimum value produced by DC₁ FOHWWECS and 8% lower than the minimum value produced by DC₂ FOHWWECS.
3. Deepening the draft leads to different effects on the annual average absorption width, depending on the DC. This is because the mechanisms enhancing power absorption varies from one DC to the other. For DC₁ the mechanism is to allow the WEC to develop its motion in a more independent manner, and the larger draft of DC₁-D₃ enhances that mechanism. For DC₃ the important is to have the substructure's heave resonance close to the WEC's resonance onset, and the shorter draft of DC₃-D₁ enhances it. DC₂ is a hybrid between DC₁ and DC₃; the substructure's heave resonance frequency is not high enough to make the substructure resonance mechanism to manifest. Therefore, it favors the WEC's resonance mechanism through DC₂-D₂ and DC₂-D₃. More detailed explanations are given in section 7.5.2.
4. Deepening the draft leads to different effects on the maximum values of the standard deviation of the nacelle acceleration, depending on the DC. This is due to a combination of different pitch natural frequencies, different characteristics of the pitch wave excitation forces and the influence of the substructure's heave resonance on the pitch RAO. For DC₁ deepening the draft means to reduce $\sigma_{aN_{a(max)}}$. For DC₃ the lowest $\sigma_{aN_{a(max)}}$ values are for the middle-level draft and the highest for the shallower draft. For DC₂, the three draft levels produce almost the same $\sigma_{aN_{a(max)}}$ values, but DC₂-D₁ has a slightly lower value than the other two drafts. More detailed explanations are given in section 7.5.2.
5. The operational subset of sea states has a very marked influence on the results. The peak periods $T_p = 7.1s$, $T_p = 8.4s$ and $T_p = 9.7s$ have the strongest impact. The first one because the most common sea state has that period and the WEC's heave resonance is tune to it. The second and third because they capture the low frequency substructure's heave resonance that enhances power absorption in DC₃ FOHWWECS.

8.2 WIDE-RANGING CONCLUSIONS

In the majority of the investigated studies related to FOHWWECS, it is considered that the substructure main objective is to support the WT and guarantee a stable wind power production and protection of the WT equipment. It also supports the WECs, but it is considered that it does not actively participate in the wave power absorption mechanism, specially because it normally has low natural frequencies that are away from the prevailing sea states in-

volved in the power absorption.

The present research has been developed without such a premise or consideration. For that reason, it has been found that a FOHWWEC with a substructure actively participating on the wave power absorption mechanism is able to maximize power absorption and the efficiency of that absorption. It has also been found that in order to reach those maximum values of absorbed power, the FOHWWEC substructure should function based on a buoyancy-stabilization principle.

Considering this, the following wide-ranging conclusions are established.

1. A FOHWWEC whose wave power absorption mechanism is based, at the same time, on the WEC's heave resonance and on the substructure's heave resonance is able to absorb more power and to do it more efficiently than a FOHWWEC whose wave power absorption mechanism is based only on WEC's resonance. This, of course, under the premise that proper tuning to the operational sea region has been performed.

By taking advantage of both resonances the FOHWWEC is capable of the following:

- It maintains similar or slightly lower absorption width values in sea states with low peak periods, in comparison with the values obtain through WEC's resonance only mechanism.
 - It obtains higher absorption width values in sea states with high peak periods, in comparison with the values obtain through WEC's resonance only mechanism.
2. In order to obtain a FOHWWEC whose wave power absorption mechanism is based on both resonances, the substructure floating stability principle must be buoyancy-stabilization. This is because through the WPA expansion, the heave restoring force is increased, producing an increment of the heave resonance frequency that sets the substructure's heave resonance peak in the prevailing wave period range of ocean waves (6-10s) [32].
 3. In the present research, the two resonances (WEC and substructure) has been combined in such a way that the substructure's heave resonance is close to the onset of the WEC's heave resonance. Nevertheless, It might be equally efficient or even more efficient to separate them, encompassing a larger range of the operational subset in study.
 4. Bouyancy-stabilization also has the following advantages, contributing to the performance of the FOHWWEC:
 - The separation between the heave and pitch resonance frequencies is enlarged, in comparison with FOHWWECs employing the

other two stabilization principles. This allows to set the heave resonance in range of the wave frequencies involved in power absorption and to keep the pitch resonance peaks away from them.

- The magnitude of the heave resonance peak, that has an impact on the horizontal nacelle accelerations (see $\sigma_{aN\alpha(\max)}$ value for DC3-D1) is partially damped by the hydrodynamic and mechanical damping added by the WECs, as it has been demonstrated by analyzing Figure 107. This is more relevant when the absorption mechanism based on both resonances (WEC and substructure) is employed, because in this case the substructure's heave resonance manifest on the nacelle acceleration RAO in frequencies that are captured by the wave spectra involved in power absorption.
5. Although the wave power absorption mechanism based on the WEC and the substructure resonances is capable of producing higher absorption width values, further research is required to determine if a FOHWWEC operating under such conditions is convenient, feasible and safe.
 6. As it has been seen, different wave power absorption mechanisms are available in the FOHWWEC's design space and for one of them it is required that the substructure actively participates. This demonstrates that considering both, wind and wave power generation from the beginning in the design of a new FOHWWEC is the most convenient and reasonable approach. By limiting to an existing substructure, some opportunities to maximize the wave absorbed power are lost. In a similar line of thought, it is reasonable to start the design of a new FOHWWEC concept with a buoyancy-stabilized substructure and not with a ballast-stabilized or ballast-buoyancy-stabilized substructure. This is because buoyancy-stabilization provides the required flexibility to thoroughly explore and find the balance between design variables such as WPA, displacement, draft, size and position of the WECs, mooring, among others, in order to optimize both, wind and wave power.

8.3 RECOMMENDATIONS

Future investigation should enhance the present work in three ways. First, by modeling additional physical phenomena in order to get closer to the real phenomena. Second, by analyzing new substructure geometries, WEC's configurations and several sea regions, widening the exploration of the design space. Third, by performing model tests with the purpose of validating the obtained numerical results.

Here the most relevant suggestions for each way of enhancement.

1. The wind loads should be included in the dynamic model. There are two possibilities to do this. First option is a linearization in the fre-

quency domain, probably using additional software, in a similar way as it is done in references [7] and [8]. Second option is to develop the analysis in the time domain.

2. It is strongly recommended as well to perform the study in 45 degree waves, in order to consider all DOFs and the complete coupled motion of the FOHWEC.
3. It is also strongly recommended to perform the simulations in other sea regions to compare the results with the results of this thesis, and derive conclusions from it.
4. This study has determined that DC₃ configuration is more convenient to be implemented. Then, it is recommended to optimize DC₃ in a future study. For example, the number of WECs and their position on the substructure, and the number of cylinders might be interesting parameters to be used in the optimization process.
5. By setting up model tests for each DC the results of the present thesis could be validated. This would also help quantifying the influence of physical phenomena currently not included (viscous damping, non-linear mooring effects, wind loads, among others).
6. It is recommended to study the effect that end stops or a method to suppress WEC's motion for the system's safety would have on the performance variables. In the present study it has been established that the system can accommodate any relative heave displacement of the WEC. Nevertheless, this is not practical in reality.
7. It is recommended to perform a future investigation to determine if the power absorption mechanism based on the substructure's heave resonance can be actually implemented in reality, or if it has not acceptable consequences on the WT performance or its equipment.
8. It is important to study whether linearizing the mooring loads around the initial position rather than the equilibrium position is accurate enough. In other words, to study the effect of the non-linear mooring forces on the FOHWEC dynamics.
9. It is also recommended to study the effects of the hydrodynamic viscous damping on the substructure and on the WECs.
10. It is recommended to include the vertical nacelle accelerations as a performance variable in a future investigation. This acceleration also have an impact on the wind power production.
11. It would be interesting to perform analyses for WECs with different working principles. For example, pitching or surging WECs. Additional substructure's geometries should be studied as well. As an example, barge and semi-submersible type of substructures.

12. It is recommended, in general, to further analyze the effect of wave diffraction on the performance and if those effects can be tuned with the FOHWEC geometry to obtain a better performance.

APPENDIX A

A.1 STABILITY CALCULATION RESULTS FOR DC2 AND DC3

In this section the following data, related to the stability calculation of DC2 and DC3, is included:

1. The input/output (I/O) data of the stability calculation, from Table 65 until Table 72.
2. The righting moment curves, from Figure 114 until Figure 119.

Property	Value	I/O
f [m]	15	I
D _{max} [m]	80	I
l _{cyl-cyl} [m]	35	I
WT prop. [-]	In Appendix B	I
$\rho_{s(eq)}$ [Kg/m ³]	8500	I
d _{rat} [-]	1.33	I
r _{cyl} ^{max} [m]	6	I
φ_{max} [°]	10	I
θ_{max} [°]	10	I

Table 65: DC2 common stability input

Property	Value	I/O
D [m]	53	O
r _{cyl} [m]	6	O
∇_{wb} [tons]	12288.03	O
m _{b_{WT}} [tons]	3518.06	O
m _{b_B} [tons]	4215.52	O
CoB _z [m]	-26.5	O
CoG _z [m]	-32.42	O
GM _t [m]	6.09	O
GM _l [m]	11.87	O
I _{yy} [Kg.m ²]	1.94894e+10	O

Table 66: FOWT DC2-D1 stability I/O

Property	Value	I/O
D [m]	63	O
r _{cyl} [m]	6	O
∇_b [tons]	14606.52	O
m _{b_{WT}} [tons]	4422.66	O
m _{b_B} [tons]	5120.12	O
CoB _z [m]	-31.5	O
CoG _z [m]	-41.55	O
GM _t [m]	10.20	O
GM _l [m]	15.06	O
I _{yy} [Kg.m ²]	2.37999e+10	O

Table 67: FOWT DC2-D2 stability I/O

Property	Value	I/O
D [m]	73	O
r_{cyl} [m]	6	O
∇_b [tons]	16925.02	O
$m_{b_{WT}}$ [tons]	5327.27	O
m_{b_B} [tons]	6024.73	O
CoB _z [m]	-36.5	O
CoG _z [m]	-50.45	O
GM _t [m]	14.08	O
GM _l [m]	18.27	O
I _{yy} [Kg.m ²]	2.87699e+10	O

Table 68: FOWT DC2-D3 stability I/O

Property	Value	I/O
f [m]	15	I
α_{subs} [°]	60	I
$l_{cyl-cyl}$ [m]	45	I
WT prop. [-]	In Appendix B	I
$\rho_{s(eq)}$ [Kg/m ³]	8500	I
d_{rat} [-]	1.33	I
r_{cyl}^{max} [m]	6	I
φ_{max} [°]	10	I
θ_{max} [°]	10	I

Table 69: DC3 common stability input

Property	Value	I/O
D [m]	22	O
r_{cyl} [m]	6	O
∇_{wb} [tons]	7651.03	O
$m_{b_{WT}}$ [tons]	1287.14	O
m_{b_B} [tons]	1984.60	O
CoB _z [m]	-11.0	O
CoG _z [m]	-2.54	O
GM _t [m]	7.29	O
GM _l [m]	9.21	O
I _{yy} [Kg.m ²]	1.16711e+10	O

Table 70: FOWT DC3-D1 stability I/O

Property	Value	I/O
D [m]	32	O
r_{cyl} [m]	6	O
∇_b [tons]	11128.77	O
$m_{b_{WT}}$ [tons]	2644.04	O
m_{b_B} [tons]	3341.5	O
CoB _z [m]	-16.0	O
CoG _z [m]	-13.84	O
GM _t [m]	8.67	O
GM _l [m]	9.98	O
I _{yy} [Kg.m ²]	1.60401e+10	O

Table 71: FOWT DC3-D2 stability I/O

Property	Value	I/O
D [m]	42	O
$r_{c_{yl}}$ [m]	6	O
∇_b [tons]	14606.52	O
$m_{b_{WT}}$ [tons]	4000.95	O
m_{b_B} [tons]	4698.41	O
CoB_z [m]	-36.5	O
CoG_z [m]	-23.66	O
GM_t [m]	10.91	O
GM_l [m]	11.91	O
I_{yy} [Kg.m ²]	2.10803e+10	O

Table 72: FOWT DC3-D3 stability I/O

The meaning of each property included in these tables can be found in the symbols list.

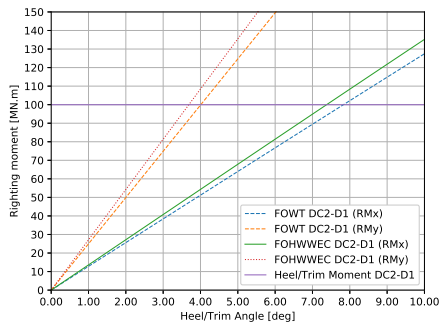


Figure 114: Righting moment curve for DC2-D1

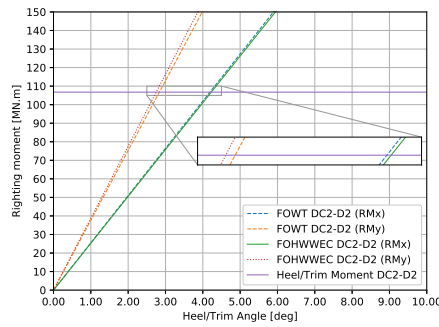


Figure 115: Righting moment curve for DC2-D2

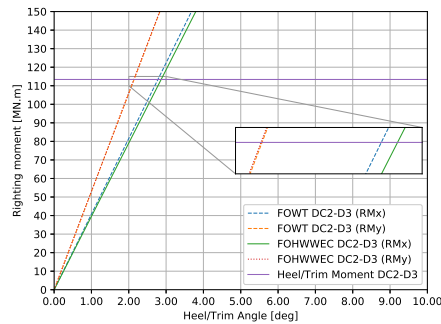


Figure 116: Righting moment curve for DC2-D3

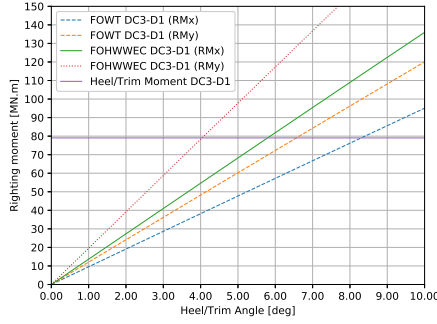


Figure 117: Righting moment curve for DC3-D1

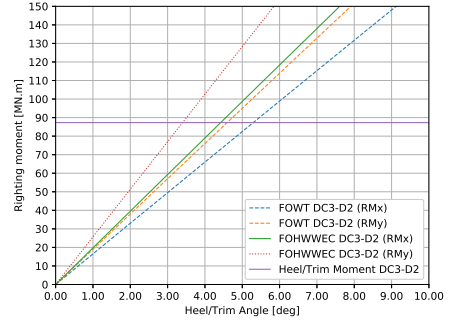


Figure 118: Righting moment curve for DC3-D2

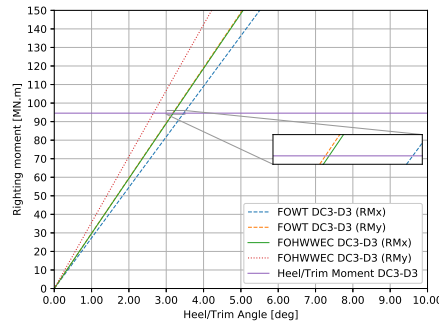


Figure 119: Righting moment curve for DC3-D3

As it can be seen in these plots, all the studied cases for DC2 and DC3 are stable since all intercept angles are below 10°.

A.2 STANDARD DEVIATION OF THE NACELLE ACCELERATION MATRICES OF DC FOWTS

In this section the standard deviation of the nacelle acceleration matrices for all DC FOWTs are presented, from Table 73 until 81. This data is relevant because is employed in the calculation of $\sigma_{aNa(avg)}$, that is included in the performance plot of each DC.

- DC1 FOWTs:

H_s/T_p	4.5	5.8	7.1	8.4	9.6
0.5	0.006	0.008	0.008	0.008	0.008
1.5	0.018	0.023	0.025	0.024	0.023
2.5	0.030	0.039	0.041	0.041	0.039
3.5	0.0	0.054	0.058	0.057	0.054

Table 73: DC1-D1 FOWT standard deviation of the nacelle acceleration [g]

H_s/T_p	4.5	5.8	7.1	8.4	9.6
0.5	0.006	0.007	0.008	0.008	0.008
1.5	0.017	0.022	0.024	0.023	0.023
2.5	0.028	0.037	0.039	0.039	0.038
3.5	0.0	0.052	0.055	0.055	0.053

Table 74: DC₁-D₂ FOWT standard deviation of the nacelle acceleration [g]

H_s/T_p	4.5	5.8	7.1	8.4	9.6
0.5	0.005	0.007	0.008	0.008	0.007
1.5	0.016	0.021	0.022	0.022	0.022
2.5	0.027	0.035	0.037	0.037	0.036
3.5	0.0	0.049	0.052	0.052	0.050

Table 75: DC₁-D₃ FOWT standard deviation of the nacelle acceleration [g]

- DC₂ FOWTs:

H_s/T_p	4.5	5.8	7.1	8.4	9.6
0.5	0.005	0.005	0.004	0.004	0.004
1.5	0.015	0.014	0.010	0.012	0.013
2.5	0.024	0.024	0.018	0.020	0.022
3.5	0.0	0.033	0.025	0.028	0.030

Table 76: DC₂-D₁ FOWT standard deviation of the nacelle acceleration [g]

H_s/T_p	4.5	5.8	7.1	8.4	9.6
0.5	0.005	0.005	0.004	0.004	0.005
1.5	0.015	0.015	0.011	0.013	0.014
2.5	0.025	0.024	0.019	0.021	0.024
3.5	0.0	0.034	0.026	0.030	0.033

Table 77: DC₂-D₂ FOWT standard deviation of the nacelle acceleration [g]

H_s/T_p	4.5	5.8	7.1	8.4	9.6
0.5	0.005	0.005	0.004	0.004	0.005
1.5	0.015	0.014	0.011	0.013	0.015
2.5	0.024	0.024	0.019	0.022	0.025
3.5	0.0	0.034	0.026	0.031	0.035

Table 78: DC₂-D₃ FOWT standard deviation of the nacelle acceleration [g]

- DC₃ FOWTs:

H_s/T_p	4.5	5.8	7.1	8.4	9.6
0.5	0.003	0.003	0.004	0.007	0.014
1.5	0.009	0.010	0.011	0.021	0.042
2.5	0.015	0.016	0.019	0.036	0.070
3.5	0.0	0.022	0.026	0.050	0.098

Table 79: DC₃-D1 FOWT standard deviation of the nacelle acceleration [g]

H_s/T_p	4.5	5.8	7.1	8.4	9.6
0.5	0.004	0.005	0.004	0.004	0.006
1.5	0.013	0.015	0.011	0.013	0.017
2.5	0.021	0.025	0.019	0.022	0.029
3.5	0.0	0.035	0.026	0.030	0.041

Table 80: DC₃-D2 FOWT standard deviation of the nacelle acceleration [g]

H_s/T_p	4.5	5.8	7.1	8.4	9.6
0.5	0.005	0.006	0.005	0.005	0.005
1.5	0.014	0.018	0.013	0.014	0.015
2.5	0.024	0.030	0.022	0.023	0.025
3.5	0.0	0.042	0.031	0.032	0.035

Table 81: DC₃-D3 FOWT standard deviation of the nacelle acceleration [g]

A.3 ABSORBED ENERGY MATRICES OF DC FOHWWECS

The absorbed energy for each DC FOHWWEC is presented in this section, from table 82 until table 90. The total sum, in the lower right corner of each table, corresponds to the annual energy absorption.

- DC₁ FOHWWECS:

H_s/T_p	4.5	5.8	7.1	8.4	9.6	Sum
0.5	0.3	5.5	10.6	3.8	0.8	20.9
1.5	0.4	28.2	122.3	83.1	27.8	261.8
2.5	0.4	27.2	176.8	170.2	77.3	451.8
3.5	0.0	18.8	148.5	178.3	98.4	444.0
Sum	1.0	79.7	458.2	435.4	204.3	1178.5

Table 82: DC₁-D1 absorbed energy per year [MWh/y]

H_s/T_p	4.5	5.8	7.1	8.4	9.6	Sum
0.5	0.3	5.5	10.6	3.9	0.8	21.1
1.5	0.4	28.4	122.9	84.2	28.1	264.0
2.5	0.4	27.4	177.7	172.5	78.1	456.0
3.5	0.0	19.0	149.3	180.6	99.5	448.3
Sum	1.0	80.3	460.5	441.1	206.4	1189.3

Table 83: DC1-D2 absorbed energy per year [MWh/y]

H_s/T_p	4.5	5.8	7.1	8.4	9.6	Sum
0.5	0.3	5.6	10.7	3.9	0.8	21.2
1.5	0.4	28.6	123.4	85.1	28.6	266.1
2.5	0.4	27.6	178.5	174.3	79.4	460.1
3.5	0.0	19.1	149.9	182.5	101.2	452.7
Sum	1.0	80.8	462.4	445.8	210.0	1200.1

Table 84: DC1-D3 absorbed energy per year [MWh/y]

- DC2 FOHWWECS:

H_s/T_p	4.5	5.8	7.1	8.4	9.6	Sum
0.5	0.2	4.1	10.7	4.2	0.9	20.1
1.5	0.3	21.1	123.8	91.7	31.1	268.1
2.5	0.3	20.4	179.1	187.8	86.4	474.0
3.5	0.0	14.1	150.4	196.7	110.1	471.3
Sum	1.0	79.7	458.2	435.4	204.3	1233.5

Table 85: DC2-D1 absorbed energy per year [MWh/y]

H_s/T_p	4.5	5.8	7.1	8.4	9.6	Sum
0.5	0.3	4.1	10.8	4.3	0.9	20.4
1.5	0.4	21.2	125.0	93.7	31.3	271.6
2.5	0.3	20.4	180.8	191.8	86.8	480.4
3.5	0.0	14.1	151.9	200.9	110.8	477.7
Sum	0.9	59.9	468.6	490.7	229.9	1250.0

Table 86: DC2-D2 absorbed energy per year [MWh/y]

H_s/T_p	4.5	5.8	7.1	8.4	9.6	Sum
0.5	0.3	3.5	10.9	4.3	0.9	19.8
1.5	0.4	17.8	125.8	94.4	31.7	270.0
2.5	0.3	17.1	182.0	193.4	88.0	480.8
3.5	0.0	11.8	152.9	202.5	112.0	479.3
Sum	1.0	50.2	471.5	494.7	232.5	1249.9

Table 87: DC2-D3 absorbed energy per year [MWh/y]

- DC₃ FOHWECs:

H_s/T_p	4.5	5.8	7.1	8.4	9.6	Sum
0.5	0.2	4.7	9.9	6.1	3.4	24.3
1.5	0.3	24.3	115.0	131.7	122.0	393.3
2.5	0.3	23.4	166.3	269.8.4	339.0	798.7
3.5	0.0	16.2	139.7	282.5	431.8	870.2
Sum	0.8	68.6.2	431.0	690.0	896.2	2086.6

Table 88: DC₃-D1 absorbed energy per year [MWh/y]

H_s/T_p	4.5	5.8	7.1	8.4	9.6	Sum
0.5	0.3	5.1	10.1	4.4	1.1	21.1
1.5	0.4	26.4	117.3	96.1	39.1	279.4
2.5	0.3	25.5	169.7	196.9	108.6	501.0
3.5	0.0	17.6	142.5	206.2	138.4	504.7
Sum	1.0	74.7	439.7	503.6	287.2	1306.2

Table 89: DC₃-D2 absorbed energy per year [MWh/y]

H_s/T_p	4.5	5.8	7.1	8.4	9.6	Sum
0.5	0.3	5.4	9.6	4.3	0.9	20.5
1.5	0.4	27.6	110.9	94.4	33.9	267.2
2.5	0.4	26.6	160.4	193.4	94.3	475.1
3.5	0.0	18.4	134.8	202.6	120.1	475.8
Sum	1.0	77.8	415.7	494.8	249.3	1238.6

Table 90: DC₃-D3 absorbed energy per year [MWh/y]

APPENDIX B

B.1 WIND TURBINE PROPERTIES

In this appendix the properties of the NREL 5MW wind turbine are presented in Table 91. All these properties have been used in the calculations. The majority of them have been obtained from reference [35] and when the source of information differs, it is indicated in the remarks column. The orientation of the axes is given by the coordinate system $G(x_b, y_b, z_b)$ in Figure 14, with x_b pointing downwind. The properties are ordered as in the WT input interface of the *FOHWWEC Analysis Program*.

Property	Value	Remark
Hub height [m]	90.0	From WT tower base
WT CoG z coordinate [m]	64.0	From WT tower base
WT CoG y coordinate [m]	0.0	
WT CoG x coordinate [m]	0.0	Assumed. In reality is -0.2m
Tower CoG z coordinate [m]	38.2	From WT tower base
RNA CoG z coordinate [m]	89.6	From WT tower base [45]
Rotor diameter [m]	126	
On the base (OTB) tower diam. [m]	6	
On the top (OTT) tower diam. [m]	3.87	
Tower height [m]	87.6	From WT tower base
Tower plate thick. [m]	0.027	
Rotor mass [tons]	110.0	
Nacelle mass [tons]	240.0	
Tower mass [tons]	347.5	
Total mass [tons]	697.5	
RNA I_{xx} [Kg.m ²]	4.5050444×10^7	From tower top [45]
RNA I_{yy} [Kg.m ²]	2.4940618×10^7	From tower top [45]
RNA I_{zz} [Kg.m ²]	2.5477668×10^7	From tower top [45]
RNA I_{zx} [Kg.m ²]	1.454038×10^6	From tower top [45]
Peak rotor thrust force [kN]	750	

Table 91: NREL 5 MW wind turbine properties [35]

APPENDIX C

C.1 FOHWWEC ANALYSIS PROGRAM - USER GUIDE

In this section a short user guide of the program developed by the author is included. The objective is to provide the user with a document to understand the setup of the program and provide instructions on how it should be used. The guide has been developed to be used as a standalone document, independent from the present research.

FOHWWEC ANALYSIS PROGRAM - USER GUIDE

MARTIN A. GONZALEZ JIMENEZ

Version 0.1 - March 2020

1. PURPOSE

The purpose of this guide is to provide the user of the *FOHWWEC Analysis Program* with instructions on how to setup and use the program. The structure of the program is also described.

2. GENERAL DESCRIPTION OF THE PROGRAM

FOHWWEC stands for Floating Offshore Hybrid Wind-Wave Energy Converter.

The FOHWWEC Analysis Program is a software developed in the programming language Python (v3.7.3). Its current main objectives are:

- a) To provide a platform to develop a semi-automated evaluation of the performance of three different FOHWWEC design configurations (DCs).
- b) To provide a platform to evaluate the influence of selected geometrical parameters in the performance of each DC.

The criteria to define the three DCs and the geometrical parameters can vary. In its current version, the program has been configured to perform the evaluation described in the author's MSc. thesis. Nevertheless, the program's code and structure facilitates the configuration of other types of evaluation. How to perform that configuration is not described in the present guide.

The FOHWWEC Analysis Program interacts with other two programs: SALOME and NEMOH. SALOME is an open source program, used to model the underwater surfaces and to mesh them. NEMOH is an open source Boundary Element Method (BEM) solver. It provides the hydrodynamic coefficients and wave excitation forces needed to solve the FOHWWEC's motion equation.

Both, SALOME and NEMOH, are used in their Windows versions. SALOME version 9.2.2 and NEMOH version 2.03.

3. STRUCTURE OF THE PROGRAM

The FOHWWEC Analysis Program consist of several python files that interact with each other. These files can be grouped in the following manner:

- *Group 1 - Administration:* This group includes the files controlling user interfaces, file paths, input reading and plotting of results. The python files in this group are shown in Figure C.1.1.

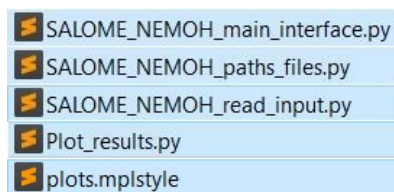


Figure C.1.1: Group 1 python files

- *Group 2 - Hydrostatic stability calculation:* This group of files is constructed to perform the stability calculations of the isolated WEC and each DC. The python files are portrayed in Figure C.1.2.

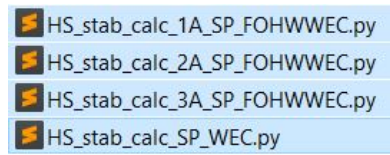


Figure C.1.2: Group 2 python files

- *Group 3 - Hydrostatic restoring force calculation:* The files in this group perform the calculation of the hydrostatic restoring coefficients for each floating body. They are depicted in Figure C.1.3.

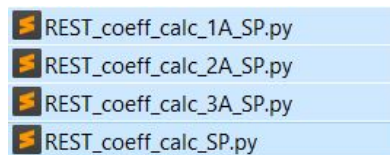


Figure C.1.3: Group 3 python files

- *Group 4 - Wave spectrum:* This group performs the calculations related to the wave spectrum. The python file is listed in Figure C.1.4.

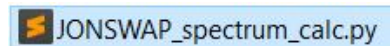


Figure C.1.4: Group 4 python files

- *Group 5 - Mooring system calculation:* The calculations related to the mooring system are performed by this group. Python files are shown in Figure C.1.5.

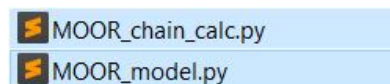


Figure C.1.5: Group 5 python files

- *Group 6 - Available power calculation:* This group addresses the calculation of the available power in the given operational region. The python file performing this action is shown in Figure C.1.6.



Figure C.1.6: Group 6 python files

- *Group 7 - Motion and performance calculation:* This is the main group. It performs the calculation of the motion and performance variables for the isolated WEC, DC FOWTs and DC FOHWWECs. Several python files are part of this group, as it can be seen in Figure C.1.7.

DYN_1A_SP_FOHWWEC_D1.py	POWER_calc_1A_SP_FOHWWEC_D1.py
DYN_1A_SP_FOHWWEC_D2.py	POWER_calc_1A_SP_FOHWWEC_D2.py
DYN_1A_SP_FOHWWEC_D3.py	POWER_calc_1A_SP_FOHWWEC_D3.py
DYN_2A_SP_FOHWWEC_D1.py	POWER_calc_2A_SP_FOHWWEC_D1.py
DYN_2A_SP_FOHWWEC_D2.py	POWER_calc_2A_SP_FOHWWEC_D2.py
DYN_2A_SP_FOHWWEC_D3.py	POWER_calc_2A_SP_FOHWWEC_D3.py
DYN_3A_SP_FOHWWEC_D1.py	POWER_calc_3A_SP_FOHWWEC_D1.py
DYN_3A_SP_FOHWWEC_D2.py	POWER_calc_3A_SP_FOHWWEC_D2.py
DYN_3A_SP_FOHWWEC_D3.py	POWER_calc_3A_SP_FOHWWEC_D3.py
DYN_SP_WEC.py	POWER_calc_SP.py
	PTO_calc.py
NACA_calc_1A_SP_FOHWWEC_D1.py	RAO_calc_1A_SP_FOHWWEC_D1.py
NACA_calc_1A_SP_FOHWWEC_D2.py	RAO_calc_1A_SP_FOHWWEC_D2.py
NACA_calc_1A_SP_FOHWWEC_D3.py	RAO_calc_1A_SP_FOHWWEC_D3.py
NACA_calc_1A_SP_FOWT_D1.py	RAO_calc_1A_SP_FOWT_D1.py
NACA_calc_1A_SP_FOWT_D2.py	RAO_calc_1A_SP_FOWT_D2.py
NACA_calc_1A_SP_FOWT_D3.py	RAO_calc_1A_SP_FOWT_D3.py
NACA_calc_2A_SP_FOHWWEC_D1.py	RAO_calc_2A_SP_FOHWWEC_D1.py
NACA_calc_2A_SP_FOHWWEC_D2.py	RAO_calc_2A_SP_FOHWWEC_D2.py
NACA_calc_2A_SP_FOHWWEC_D3.py	RAO_calc_2A_SP_FOHWWEC_D3.py
NACA_calc_2A_SP_FOWT_D1.py	RAO_calc_2A_SP_FOWT_D1.py
NACA_calc_2A_SP_FOWT_D2.py	RAO_calc_2A_SP_FOWT_D2.py
NACA_calc_2A_SP_FOWT_D3.py	RAO_calc_2A_SP_FOWT_D3.py
NACA_calc_3A_SP_FOHWWEC_D1.py	RAO_calc_3A_SP_FOHWWEC_D1.py
NACA_calc_3A_SP_FOHWWEC_D2.py	RAO_calc_3A_SP_FOHWWEC_D2.py
NACA_calc_3A_SP_FOHWWEC_D3.py	RAO_calc_3A_SP_FOHWWEC_D3.py
NACA_calc_3A_SP_FOWT_D1.py	RAO_calc_3A_SP_FOWT_D1.py
NACA_calc_3A_SP_FOWT_D2.py	RAO_calc_3A_SP_FOWT_D2.py
NACA_calc_3A_SP_FOWT_D3.py	RAO_calc_3A_SP_FOWT_D3.py
	RAO_calc_SP.py

Figure C.1.7: Group 7 python files

- *Group 8 - SALOME related:* This group addresses all processing and post-processing activities related to SALOME. The processing activities are performed by python files that are located directly in the SALOME directory (see Figure C.1.8). The post-processing python files (Figure C.1.9) are located in the program's main directory.

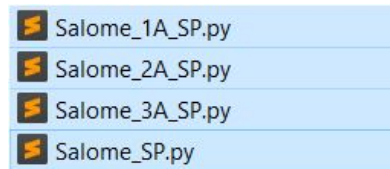


Figure C.1.8: Group 8 processing python files

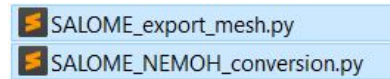


Figure C.1.9: Group 8 post-processing python files

- *Group 9 - NEMOH related:* This group basically automates the creation of the NEMOH *.cal files. The python files are depicted in Figure C.1.10.

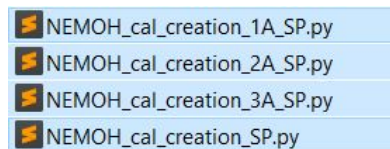


Figure C.1.10: Group 9 python files

- *Group 10 - Verification:* This group perform the verification of the selected panel's length. It is an action taken in the author's MSc thesis, but it might be adapted for other studies. The python files are shown in Figure C.1.11.

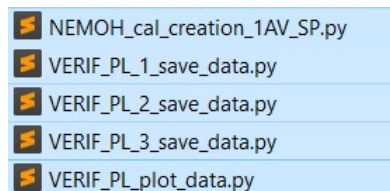


Figure C.1.11: Group 10 python files

4. INSTALLATION AND INITIALIZATION

The installation requirements are the following:

- SALOME software version 9.2.2 or higher for Windows. SALOME is normally installed in the directory shown in Figure C.1.12.



Figure C.1.12: SALOME installation directory

- NEMOH software version 2.03 or higher for Windows. The NEMOH working folder is selected by the user.
- Since the program is open source and it is in Beta version, no *.exe file has been created. Therefore, it is necessary that the user installs Python version 3.7.3 or higher for Windows.

The installation procedure is as follows:

- Select a main directory and copy the python files included in groups 1 until 10, with the exception of the SALOME processing python files (see Figure C.1.8). All these files are accessed by the program during initialization, running and termination. Make sure you are copying as well the *run.bat* file.
- Create the folder *Python_scripts* in the SALOME directory and copy the SALOME processing files (see Figure C.1.8) to it. The result is shown in Figure C.1.13.

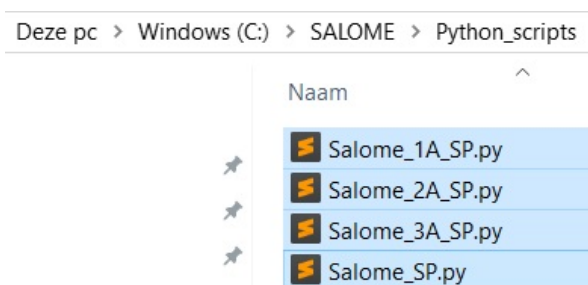


Figure C.1.13: SALOME folder for python scripts

- Create a shared folder under *Windows\Users\<user name>* folder with the name *SALOME_NEMOH_shared*. This folder is used as repository for input and output data. The python files communicate with each other through the files stored in this folder. Figure C.1.14 depicts an example share folder path.



Figure C.1.14: Shared folder example

- Double click the *run.bat* file. The program should start, presenting the main user interface window shown in Figure C.1.15.



Figure C.1.15: Main user interface

The initial configuration is as follows:

- Specify the required paths in the main user interface window. Verify that the indicated paths actually exist and save the applicable wave scatter data as a *.txt file, in the shared folder, with name *Wave_scatter_diagram*. Save the data by clicking on the *Save* button. In Figure C.1.16 example paths are shown. In Figure C.1.17 an example of the wave data file is presented.

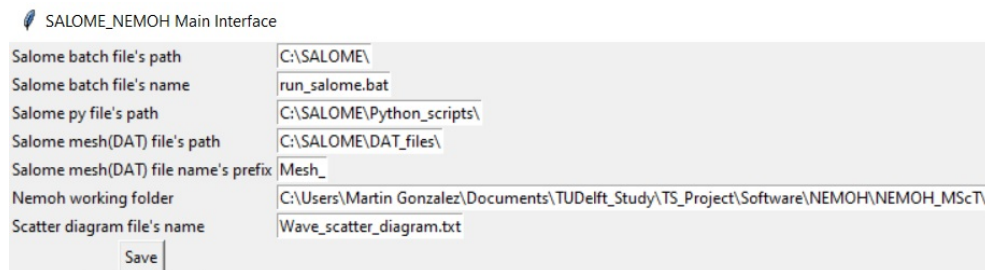


Figure C.1.16: Initial configuration paths

Wave_scatter_diagram.txt - Kladblok

Bestand	Bewerken	Opmaak	Beeld	Help									
1	3.5	4.5	5.5	6.5	7.5	8.5	9.5	10.5	11.5	12.5	13.5		
0.5	19	86	94	41	10	2	0	0	0	0	0		
1.5	3	49	121	99	40	10	2	0	0	0	0		
2.5	1	17	63	73	40	13	3	1	0	0	0		
3.5	0	6	27	39	26	10	3	1	0	0	0		
4.5	0	2	11	19	14	6	2	1	0	0	0		
5.5	0	1	4	9	7	4	1	0	0	0	0		
6.5	0	0	2	4	4	2	1	0	0	0	0		
7.5	0	0	1	2	2	1	1	0	0	0	0		
8.5	0	0	0	1	1	1	0	0	0	0	0		
9.5	0	0	0	1	1	0	0	0	0	0	0		
10.5	0	0	0	0	0	0	0	0	0	0	0		
11.5	0	0	0	0	0	0	0	0	0	0	0		
12.5	0	0	0	0	0	0	0	0	0	0	0		
13.5	0	0	0	0	0	0	0	0	0	0	0		
14.5	0	0	0	0	0	0	0	0	0	0	0		

Figure C.1.17: Wave scatter diagram *.txt file example

- b) Create the *results* folder under the SALOME directory (see Figure C.1.18). The converted mesh files are saved in this folder.

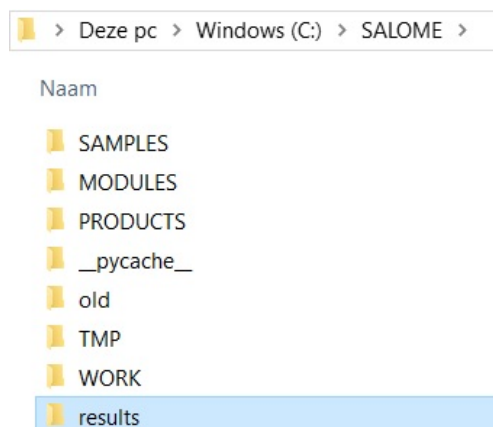


Figure C.1.18: SALOME results folder

- c) Create the *Nemoh_initial_data* folder under the NEMOH working directory. Copy the NEMOH files required to start a run into the newly created folder. Figure C.1.19 depicts the required files.

Deze pc > Documenten > TUDelft_Study > TS_Project > Software > NEMOH > NEMOH_MScT > Nemoh_initial_data				
Naam		Gewijzigd op	Type	Grootte
ID.dat		18-12-2013 16:42	DAT-bestand	1 kB
input.txt		18-12-2013 15:44	Tekstdocument	1 kB
LICENSE.txt		13-1-2014 14:56	Tekstdocument	11 kB
Mesh.exe		16-4-2015 21:06	Toepassing	1.120 kB
Nemoh.cal		17-7-2019 13:33	CAL-bestand	2 kB
Normalvelocities.dat		17-7-2019 13:34	DAT-bestand	948 kB
NOTICE.txt		13-1-2014 15:03	Tekstdocument	1 kB
postProcessor.exe		5-12-2014 11:43	Toepassing	1.145 kB
preProcessor.exe		11-7-2014 17:16	Toepassing	1.170 kB
run.bat		19-2-2018 23:02	Windows-batchbe...	1 kB
Solver.exe		10-3-2015 15:41	Toepassing	832 kB

Figure C.1.19: NEMOH data

5. WORKING WITH THE PROGRAM

Here it is explained how the user should work with the program.

- a) The *FOHWVEC Analysis Program* is built to perform four simulations: isolated WECs, DC₁, DC₂ and DC₃. To perform each simulation the user should follow the steps from 1 until 13, tagged in Figure C.1.21 and described in the following paragraphs.

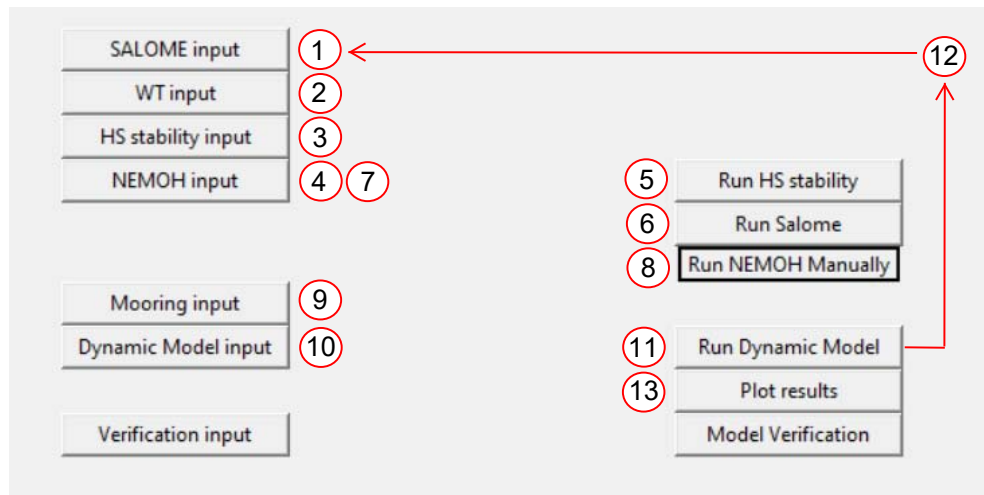


Figure C.1.20: Step-by-step of working with the program

- i. Step 1: Click on the *SALOME input* button. Select the type of run → *WEC only* for the isolated WEC simulation or *FO-HWWEC* for DC₁, DC₂ and DC₃ simulations. Select the WEC → *Sphere* is the currently available option. Select the FOHWWEC DC → *1A* for DC₁, *2A* for DC₂ and *3A* for DC₃. Select the WEC position → *CC* is the currently available option. Specify the required parameters. Click the *Save* button and then the *Back to initial input* button. Figure C.1.21 shows the DC₁'s required parameters as an example.

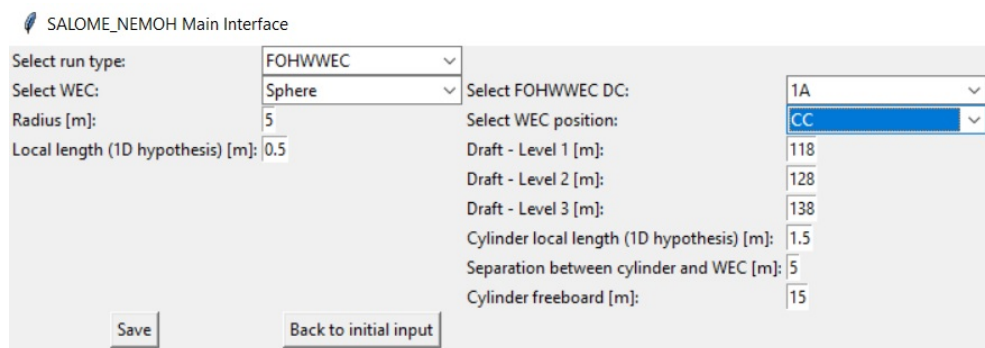


Figure C.1.21: SALOME input example for DC₁

- ii. Step 2: Click on the *WT input* button. Select the WT → *NREL-5MW* is the currently available option. Specify the required parameters. Click the *Save* button and then the *Back to initial input* button. Figure C.1.22 portrays the parameters corresponding to the NREL-5MW WT.

SALOME_NEMOH Main Interface

Select WT: NREL-5MW

Hub height [m]:	90	tower plate thickness [m]:	0.027	RNA lzx about tower top [Kg.m2]:	1454037.637
WT CG z coordinate [m]:	64	Rotor mass [Kg]:	110000	Cut-In wind speed [m/s]:	3
tower CG z coordinate [m]:	38.234	Nacelle mass [Kg]:	240000	Rated wind speed [m/s]:	11.4
RNA CG z coordinate [m]:	89.567	Tower mass [Kg]:	347460	Cut-Out wind speed [m/s]:	25
Rotor diameter [m]:	126	Total mass [Kg]:	697460	Cut-In rotor speed [rpm]:	6.9
On the base tower diameter [m]:	6	RNA lxx about tower top [Kg.m2]:	45050443.961	Rated rotor speed [rpm]:	12.1
On the top tower diameter [m]:	3.87	RNA lyy about tower top [Kg.m2]:	24940615.741	Peak rotor thrust [N]:	750000
tower height [m]:	87.6	RNA lzz about tower top [Kg.m2]:	25477667.652		

Buttons: Save, Back to initial input

Figure C.1.22: WT input

- iii. Step 3: Click on the *HS stability input* button. Specify the required parameters. Click the *Save* button and then the *Back to initial input* button. Figure C.1.23 presents the required input for the stability calculation.

SALOME_NEMOH Main Interface

Steel density [Kg/m3]:	7850.0
Equivalent steel density [Kg/m3]:	8500
OTB tower diam./Subs diam. initial ratio [-]:	1.333
Maximum cylinder radius [m]:	6
Max. heeling angle [deg]:	10
Max. trimming angle [deg]:	10
Maximum draft for DC2 [deg]:	80

Buttons: Save, Back to initial input

Figure C.1.23: Hydrostatic stability input

- iv. Step 4: Click on the *NEMOH input* button. Specify the required parameters. Click the *Save* button and then the *Back to initial input* button. Figure C.1.24 shows the required input for NEMOH.

SALOME_NEMOH Main Interface

Water density [Kg/m3]:	1025.0
Gravity [m/s2]:	9.81
Water depth [m]:	250.0
Number of wave frequencies [rads/s]:	76
First wave frequency [rads/s]:	0.005
Last wave frequency [rads/s]:	2.255

Buttons: Save, Create NEMOH.cal, Back to initial input

Figure C.1.24: NEMOH input

- v. Step 5: Click on the *Run HS stability* button → The stability of the WEC or FOHWWEC selected in step 1 is evaluated. Once stability is proven the righting moment curves are plotted and

the mass matrix is calculated. The most relevant stability output data is saved to the shared folder, specifically in one of the folders shown in Figure C.1.25.

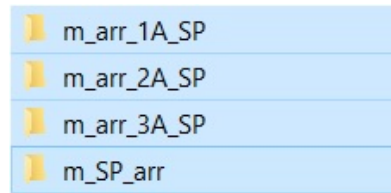


Figure C.1.25: HS Stability output folders

- vi. Step 6: Click on the *Run Salome* button → The SALOME program is started and the applicable python script is run. The submerged surfaces are automatically modeled and meshed. The mesh data is exported to the SALOME *DAT_files* folder and converted to comply with NEMOH requirements. Converted mesh data is saved in the SALOME *results* folder. In the case of the FOHWECs, the program automatically processes all three draft levels. As an example, Figure C.1.26 present the converted mesh files for DC1

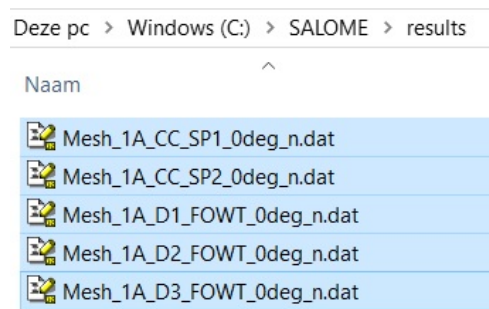


Figure C.1.26: Converted mesh files for DC1

- vii. Step 7: Click again on the *NEMOH input* button. Then, click on the *Create NEMOH.cal* button → all the files required to run NEMOH are copied from the *Nemoh_initial_data* folder to the NEMOH initialization folder (see an example initialization folder path in Figure C.1.28) → the message shown in Figure C.1.27 is shown and the user should type the letter *c* + Enter to continue. The NEMOH *.cal file(s) are generated.

```

C:\> Odrachtprompt - py Test16.py
NEMOH folders and initial data are created. Enter "c" to continue:
  
```

Figure C.1.27: Message requesting input from user

Deze pc > Documenten > TUDelft_Study > TS_Project > Software > NEMOH > NEMOH_MSct > 1A-CC_Sphere > 0deg > D1_FOHWVEC >

Figure C.1.28: Example NEMOH initialization folder

- viii. Step 8: Browse to the applicable NEMOH initialization folder and run NEMOH by clicking on the *run.bat* file. In the case of a FOHWVEC, six runs should be done, three for FOHWVECs and three for FOWTs. It is decided that NEMOH should be run manually because each run can take several hours. The output files are saved in the *Results* folder, located in the initialization folder (see Figure C.1.29). From these output files, two are relevant for the calculations performed by the program: the *ExcitationForce.tec* file and the *RadiationCoefficients.tec* file. Figures C.1.30 and C.1.31 present an extract from these files.

Deze pc > Documenten > TUDelft_Study > TS_Project > Software > NEMOH > NEMOH_MSct > 1A-CC_Sphere > 0deg > D1_FOHWVEC >

Naam	Gewijzigd op	Type	Grootte
Mesh	25-11-2019 10:47	Bestandsmap	
Results	25-11-2019 15:58	Bestandsmap	

Figure C.1.29: Example of NEMOH results folder

```
VARIABLES="w (rad/s)"
"A 1 1" "B 1 1"
"A 1 2" "B 1 2"
"A 1 3" "B 1 3"
"A 1 4" "B 1 4"
"A 1 5" "B 1 5"
"A 1 6" "B 1 6"
"A 2 1" "B 2 1"
"A 2 2" "B 2 2"
"A 2 3" "B 2 3"
"A 2 4" "B 2 4"
"A 2 5" "B 2 5"
"A 2 6" "B 2 6"
"A 3 1" "B 3 1"
"A 3 2" "B 3 2"
"A 3 3" "B 3 3"
"A 3 4" "B 3 4"
"A 3 5" "B 3 5"
"A 3 6" "B 3 6"
Zone t="Motion of body 1 in DoF 1", I= 76, F=POINT
0.5000000E-02 0.1408039E+06 0.4435728E-05 0.1364927E+00 0.3604131E-07
0.3500000E-01 0.1376180E+06 0.1921693E-02 -0.2145001E-01 -0.2092831E-07
0.6500000E-01 0.1383000E+06 0.1278593E-01 -0.3256791E-01 -0.5103220E-06
0.9500001E-01 0.1384963E+06 0.4500461E-01 -0.3093982E-01 0.4243795E-06
0.1250000E+00 0.1386966E+06 0.1222040E+00 -0.1348223E-01 -0.1730038E-05
0.1550000E+00 0.1392252E+06 0.2918972E+00 -0.2209802E-01 -0.1094868E-05
0.1850000E+00 0.1392707E+06 0.6544601E+00 -0.1972423E-01 -0.3538152E-05
```

Figure C.1.30: Example of *RadiationCoefficients.tec* file for DC1-D1

```

VARIABLES="w (rad/s) "
"abs (F 1 1) " "angle (F 1 1) "
"abs (F 1 2) " "angle (F 1 2) "
"abs (F 1 3) " "angle (F 1 3) "
"abs (F 1 4) " "angle (F 1 4) "
"abs (F 1 5) " "angle (F 1 5) "
"abs (F 1 6) " "angle (F 1 6) "
"abs (F 2 1) " "angle (F 2 1) "
"abs (F 2 2) " "angle (F 2 2) "
"abs (F 2 3) " "angle (F 2 3) "
"abs (F 2 4) " "angle (F 2 4) "
"abs (F 2 5) " "angle (F 2 5) "
"abs (F 2 6) " "angle (F 2 6) "
"abs (F 3 1) " "angle (F 3 1) "
"abs (F 3 2) " "angle (F 3 2) "
"abs (F 3 3) " "angle (F 3 3) "
"abs (F 3 4) " "angle (F 3 4) "
"abs (F 3 5) " "angle (F 3 5) "
"abs (F 3 6) " "angle (F 3 6) "
Zone t="Diffraction force - beta = 0.000 deg",I= 76,F=POINT
0.5000000E-02 0.4524037E+03 -0.1570840E+01 0.2228925E+00 -0.3131654E+01
0.3500000E-01 0.3157540E+04 -0.1570793E+01 0.1023894E+02 -0.3141563E+01
0.6500000E-01 0.5945510E+04 -0.1570779E+01 0.3586887E+02 0.3141540E+01
0.9500001E-01 0.8869141E+04 -0.1570754E+01 0.7682127E+02 -0.3141391E+01
0.1250000E+00 0.1201363E+05 -0.1570713E+01 0.1389286E+03 -0.3141322E+01
0.1550000E+00 0.1547976E+05 -0.1570647E+01 0.2188723E+03 -0.3141113E+01
0.1850000E+00 0.1936992E+05 -0.1570543E+01 0.3206231E+03 -0.3140562E+01

```

Figure C.1.31: Example of *ExcitationForce.tec* file for DC₁-D₁

- ix. Step 9: Click on the *Mooring input* button. Specify the required parameters (see Figure C.1.32). Click the *Save* button. Click on the *Calculate rest. forces* button to calculate the mooring restoring coefficient matrix. The most relevant mooring data is saved to the shared folder, specifically in the *mooring_data* folder (see Figure C.1.33). Finally, click on the *Back to initial input* button.

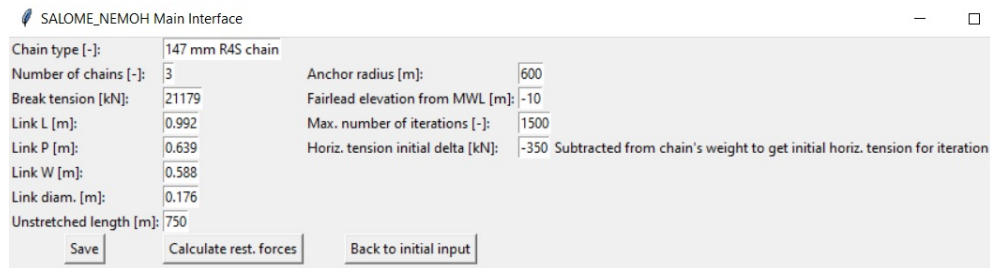


Figure C.1.32: Mooring input example

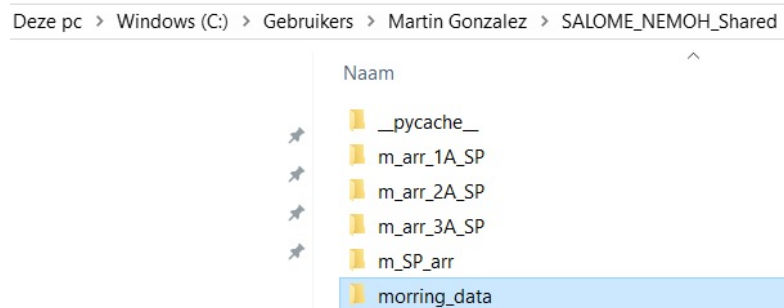


Figure C.1.33: Mooring data folder

- x. Step 10: Click on the *Dynamic Model input* button. Indicate whether the hydrodynamic coefficient interaction matrices should

be included or not in the calculation → *Y* for Yes and *N* for No. Select the PTO damping coefficient type → options are *No PTO*, *Constant* and *Optimum*. The latter option is the one employed in the author's MSc thesis and it is shown in Figure C.1.34. Notice that there are three groups of parameters. Each group corresponds to a draft level. For the isolated WEC case, only the data assigned to the first group is used.

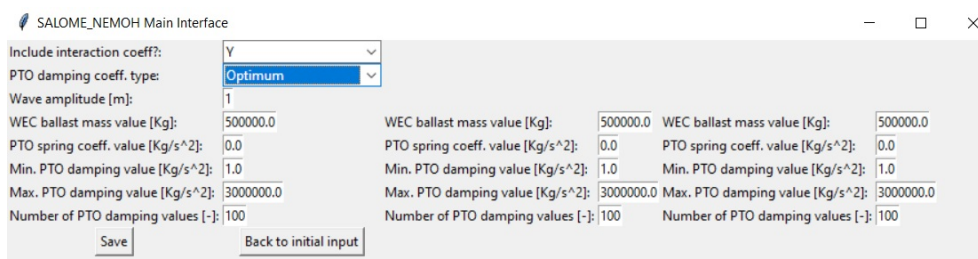


Figure C.1.34: Dynamic model input example

- xi. Step 11: Click on the *Run Dynamic Model input* button → the calculation of motions and performance for the selection made in step 1 is triggered. In the case of FOHWWECs, the three draft levels are automatically included in the calculations. The most relevant results are saved to the shared folder, specifically in the three folders highlighted in Figure C.1.35.

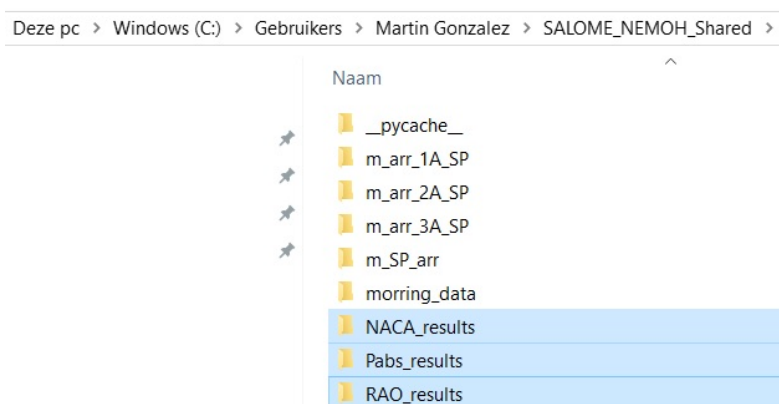


Figure C.1.35: Program's result folders

- xii. Step 12: Repeat steps 1 until 11 for the following simulation. All four simulations must be completed in order to plot the results.
- xiii. Step 13: Once all simulations are completed, click on the *Plot_results* button. This triggers the generation of all relevant plots to be used in the analysis of the results. The plot configuration inside the python file *Plot_results.py* can be edited by the user as required by the specific study performed. Figure C.1.36 is an

example. It shows that several plot windows can be generated at once.

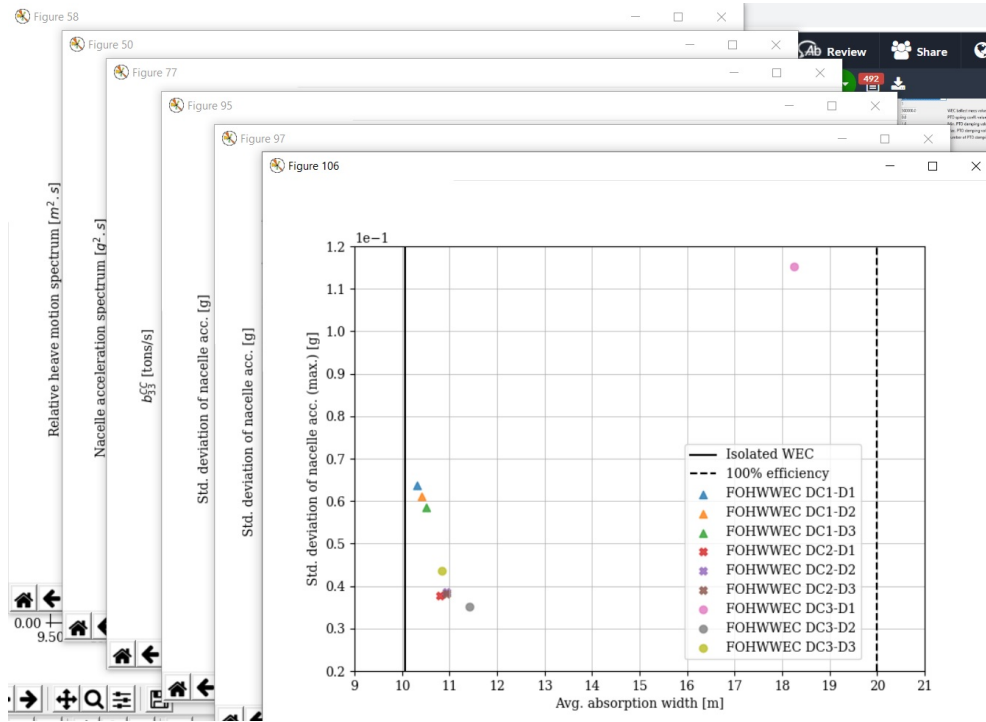


Figure C.1.36: Example result plots

BIBLIOGRAPHY

- [1] UNFCCC. *Nationally Determined Contributions (NDCs)* | UNFCCC. URL: <https://unfccc.int/process-and-meetings/the-paris-agreement/nationally-determined-contributions-ndcs> (visited on 10/22/2019).
- [2] International Renewable Energy Agency (IRENA). *Global Energy Transformation: A Roadmap to 2050*. 2018, p. 76. ISBN: 1059-910X. DOI: [Doi10.1002/\(Sici\)1097-0029\(19990915\)46:6<398::Aid-Jemt8>3.0.Co;2-H](https://doi.org/10.1002/(Sici)1097-0029(19990915)46:6<398::Aid-Jemt8>3.0.Co;2-H). URL: <http://irena.org/publications/2018/Apr/Global-Energy-Transition-A-Roadmap-to-2050>{\%}0Awww.irena.org.
- [3] Wind Europe. "Floating Offshore Wind Vision Statement." In: June (2017), p. 16. URL: <https://windeurope.org/about-wind/reports/floating-vision-statement/>.
- [4] D. Magagna, R. Monfardini, and A. Uihlein. "JRC Ocean Energy Status Report 2016 Edition." In: April 2017 (2016). ISSN: 1831-9424. DOI: [10.2760/509876](https://doi.org/10.2760/509876). URL: <https://ec.europa.eu/jrc/en/publication/euro-scientific-and-technical-research-reports/jrc-ocean-energy-status-report-2016-edition>.
- [5] M. Scheu, D. Matha, M. A. Schwarzkopf, and A. Kolios. "Human exposure to motion during maintenance on floating offshore wind turbines." In: *Ocean Engineering* 165. February (2018), pp. 293–306. ISSN: 00298018. DOI: [10.1016/j.oceaneng.2018.07.016](https://doi.org/10.1016/j.oceaneng.2018.07.016). URL: <https://doi.org/10.1016/j.oceaneng.2018.07.016>.
- [6] J. Beerens. "Offshore Hybrid Wind-Wave Energy Converter System." In: (2010).
- [7] M. Hall, B. Buckham, and C. Crawford. "Hydrodynamics-based floating wind turbine support platform optimization: A basis function approach." In: *Renewable Energy* 66 (2014), pp. 559–569. ISSN: 09601481. DOI: [10.1016/j.renene.2013.12.035](https://doi.org/10.1016/j.renene.2013.12.035). URL: <http://dx.doi.org/10.1016/j.renene.2013.12.035>.
- [8] C. Tracy. "Parametric Design of Floating Wind Turbines." In: (2007), pp. 1–93. URL: <http://hdl.handle.net/1721.1/40877>.
- [9] A. Mérigaud and J. V. Ringwood. "A nonlinear frequency-domain approach for numerical simulation of wave energy converters." In: *IEEE Transactions on Sustainable Energy* 9.1 (2018), pp. 86–94. ISSN: 19493029. DOI: [10.1109/TSTE.2017.2716826](https://doi.org/10.1109/TSTE.2017.2716826).
- [10] A. Peiffer. "DESIGN OF A POINT ABSORBER INSIDE THE WIND-FLOAT STRUCTURE." In: (2017), pp. 1–9.

- [11] A. Aubault, M. Alves, A. Sarmiento, D. Roddier, and A. Peiffer. "Modeling of an oscillating water column on the floating foundation Wind-Float." In: *Proceedings of the International Conference on Offshore Mechanics and Arctic Engineering - OMAE* 5. January (2011), pp. 235–246. DOI: [10.1115/OMAE2011-49014](https://doi.org/10.1115/OMAE2011-49014).
- [12] M. Sojo and G. Auer. "Marine Renewable Integrated Application Platform - Final Summary Report." In: (2013), pp. 1–119.
- [13] Z. Gao, T. Moan, L. Wan, and C. Michailides. "Comparative numerical and experimental study of two combined wind and wave energy concepts." In: *Journal of Ocean Engineering and Science* 1.1 (2016), pp. 36–51. ISSN: 24680133. DOI: [10.1016/j.joes.2015.12.006](https://doi.org/10.1016/j.joes.2015.12.006). URL: <http://dx.doi.org/10.1016/j.joes.2015.12.006>.
- [14] M. J. Muliawan, M. Karimirad, and T. Moan. "Dynamic response and power performance of a combined Spar-type floating wind turbine and coaxial floating wave energy converter." In: *Renewable Energy* 50 (2013), pp. 47–57. ISSN: 09601481. DOI: [10.1016/j.renene.2012.05.025](https://doi.org/10.1016/j.renene.2012.05.025). URL: <http://dx.doi.org/10.1016/j.renene.2012.05.025>.
- [15] L. Wan, M. Greco, C. Lugni, Z. Gao, and T. Moan. "A combined wind and wave energy-converter concept in survival mode: Numerical and experimental study in regular waves with a focus on water entry and exit." In: *Applied Ocean Research* 63 (2017), pp. 200–216. ISSN: 01411187. DOI: [10.1016/j.apor.2017.01.013](https://doi.org/10.1016/j.apor.2017.01.013). URL: <http://dx.doi.org/10.1016/j.apor.2017.01.013>.
- [16] C. Michailides, C. Luan, Z. Gao, and T. Moan. "Effect of Flap type Wave Energy Converters on the Response of a Semi-Submersible Wind Turbine in Operational Conditions." In: *Proceedings of the ASME 2014 33rd International Conference on Ocean, Offshore and Arctic Engineering* (2014), pp. 1–10.
- [17] C. Michailides, Z. Gao, and T. Moan. "Experimental study of the functionality of a semisubmersible wind turbine combined with flap-type Wave Energy Converters." In: *Renewable Energy* 93 (2016), pp. 675–690. ISSN: 18790682. DOI: [10.1016/j.renene.2016.03.024](https://doi.org/10.1016/j.renene.2016.03.024). URL: <http://dx.doi.org/10.1016/j.renene.2016.03.024>.
- [18] J. E. Hanssen et al. "Design and performance validation of a hybrid offshore renewable energy platform: A path to cost-efficient development of deepwater marine energy resources." In: *2015 10th International Conference on Ecological Vehicles and Renewable Energies, EVER 2015* (2015). DOI: [10.1109/EVER.2015.7113017](https://doi.org/10.1109/EVER.2015.7113017).
- [19] T. Soulard, A. Babarit, and B. Borgarino. "Preliminary Assessment of a Semi-Submersible Floating Wind Turbine Combined with Pitching Wave Energy Converters." In: *EWTEC 2013 Proceedings* May 2016 (2013).

- [20] J. Sarmiento, A. Iturrioz, V. Ayllón, R. Guanche, and I. J. Losada. “Experimental modelling of a multi-use floating platform for wave and wind energy harvesting.” In: *Ocean Engineering* 173. November 2018 (2019), pp. 761–773. ISSN: 00298018. DOI: [10.1016/j.oceaneng.2018.12.046](https://doi.org/10.1016/j.oceaneng.2018.12.046).
- [21] A. Yde, T. Larsen, A. Hansen, M. Fernandez, and S. Bellew. “Comparison of Simulations and Offshore Measurement Data of a Combined Floating Wind and Wave Energy Demonstration Platform.” In: *Journal of Ocean and Wind Energy* 2.3 (2015), pp. 129–137. ISSN: 23103604. DOI: [10.17736/jowe.2015.jcr34](https://doi.org/10.17736/jowe.2015.jcr34).
- [22] M. Karimirad. “WindWEC: Combining Wind and Wave Energy Inspired by Hywind and Wavestar.” In: December (2016).
- [23] W. Star, P. All, and D. Tel. “Wavestar prototype at Roshage.” In: (2012).
- [24] E. E. Bachynski and T. Moan. “Point Absorber Design for a Combined Wind and Wave Energy.” In: *32nd International Conference on Ocean, Offshore and Arctic Engineering* (2013), pp. 1–10.
- [25] M. Borg, M. Collu, and F. P. Brennan. “Use of a wave energy converter as a motion suppression device for floating wind turbines.” In: *Energy Procedia* 35.0 (2013), pp. 223–233. ISSN: 18766102. DOI: [10.1016/j.egypro.2013.07.175](https://doi.org/10.1016/j.egypro.2013.07.175). URL: <http://dx.doi.org/10.1016/j.egypro.2013.07.175>.
- [26] F. Fàbregas Flavià, A. Babarit, and A. H. Clément. “On the numerical modeling and optimization of a bottom-referenced heave-buoy array of wave energy converters.” In: *International Journal of Marine Energy* 19 (2017), pp. 1–15. ISSN: 22141669. DOI: [10.1016/j.ijome.2017.05.004](https://doi.org/10.1016/j.ijome.2017.05.004).
- [27] J. M. J. Journée, W. W. Massie, and R. H. M. Huijsmans. “OFFSHORE HYDROMECHANICS Third Edition (2015) Based on Original Lecture Notes (2000).” In: (2015).
- [28] O. Faltisen. *Sea Loads on Ships and Offshore Structures*. Cambridge University Press, 1993.
- [29] N. Vasilikis. “Hydrodynamic interaction and power absorption efficiency of wave energy converters in the frequency domain, using the boundary element method.” In: December (2016).
- [30] L. H. Holthuijsen. *Waves in Oceanic and Coastal Waters*. Cambridge University Press, 2009, p. 379.
- [31] A. Pecher, J. P. Kofoed, M. Folley, R. Costello, J. H. Todalshaug, L. Bergdahl, A. Têtu, and M. Alves. *Handbook of Ocean Wave Energy*. Vol. 7. 2017, p. 287. ISBN: 978-3-319-39888-4. DOI: [10.1007/978-3-319-39889-1](https://doi.org/10.1007/978-3-319-39889-1). URL: <http://link.springer.com/10.1007/978-3-319-39889-1>.
- [32] J. Falnes and J. Hals. “Heaving buoys, point absorbers and arrays.” In: *Philosophical Transactions of the Royal Society A: Mathematical, Physical and Engineering Sciences* 370.1959 (2012), pp. 246–277. ISSN: 1364503X. DOI: [10.1098/rsta.2011.0249](https://doi.org/10.1098/rsta.2011.0249).

- [33] G. Backer. "Hydrodynamic design optimization of wave energy converters consisting of heaving point absorbers." In: *Ghent University, Belgium* (2009), pp. 1–3. ISSN: 1098-6596. DOI: [10.1017/CB09781107415324.004](https://doi.org/10.1017/CB09781107415324.004). arXiv: [arXiv:1011.1669v3](https://arxiv.org/abs/1011.1669v3). URL: <http://www.vliz.be/imisdocs/publications/220173.pdf>.
- [34] D. Evans. "A theory for wave-power absorption by oscillating bodies." In: *Journal of Fluid Mechanics* 77.1 (1976).
- [35] J. Jonkman, S Butterfield, W Musial, and G Scott. "Definition of a 5-MW reference wind turbine for offshore system development." In: *Contract* February (2009), pp. 1–75. ISSN: 01487299. DOI: [10.1002/ajmg.10175](https://doi.org/10.1002/ajmg.10175). URL: http://tethys-development.pnnl.gov/sites/default/files/publications/Jonkman{_}et{_}al{_}2009.pdf.
- [36] Open Cascade. *SALOME Platform*. URL: <https://www.salome-platform.org/> (visited on 10/03/2019).
- [37] H. J. D. K. Gans. "Manual for experiments of Numerical Methods in Ship Hydromechanics." In: (2014).
- [38] M. Penalba, T. Kelly, and J. V. Ringwood. "Using NEMOH for Modelling Wave Energy Converters : A Comparative Study with WAMIT." In: *12th European Wave and Tidal Energy Conference* August (2017), p. 10.
- [39] LHEEA Centrale Nantes. *NEMOH-Presentation*. URL: <https://lheea.ec-nantes.fr/logiciels-et-brevets/nemoh-presentation-192863.kjsp> (visited on 10/03/2019).
- [40] DAMEN. "STUDLESS CHAIN OFFSHORE." In: 31.0 ().
- [41] M. K. Al-Solihat and M. Nahon. "Stiffness of slack and taut moorings." In: *Ships and Offshore Structures* 11.8 (2016), pp. 890–904. ISSN: 17445302. DOI: [10.1080/17445302.2015.1089052](https://doi.org/10.1080/17445302.2015.1089052).
- [42] BMT. *Global Wave Statistics Online*. URL: <http://www.globalwavestatisticsonline.com/> (visited on 01/28/2020).
- [43] A. Hulme. "The wave forces acting on a floating hemisphere undergoing forced periodic oscillations." In: *Journal of Fluid Mechanics* 121.57 (1982), pp. 443–463. ISSN: 14697645. DOI: [10.1017/S0022112082001980](https://doi.org/10.1017/S0022112082001980).
- [44] G. K. Ramachandran, A. Robertson, J. M. Jonkman, and M. D. Masciola. "Investigation of response amplitude operators for floating offshore wind turbines." In: *Proceedings of the International Offshore and Polar Engineering Conference* July (2013), pp. 369–376. ISSN: 10986189.
- [45] J. Jonkman. *Using Aggregate Mass in ADAMS to Check NREL CS_Monopile.bmi - NWTC*. URL: <https://wind.nrel.gov/forum/wind/viewtopic.php?f=3{\&t=842> (visited on 03/05/2020).